

Scanning Tunnelling Spectroscopy of
Subsurface Magnetic Atoms in Copper
Electron Focusing and Kondo Effect

Dissertation
zur Erlangung des Doktorgrades
der Mathematisch-Naturwissenschaftlichen Fakultäten
der Georg-August-Universität zu Göttingen

vorgelegt von
Alexander Weismann
aus Gräfelfing

Göttingen, 2008

II

D7

Referent: Prof. Dr. R. G. Ulbrich

Korreferent: Prof. Dr. K. Schönhammer

Tag der mündlichen Prüfung: 9. 7. 2008

Contents

1	Introduction	1
2	Experimental setup	7
2.1	Sample preparation	7
2.1.1	UHV metal epitaxy chamber	8
2.1.2	Single crystal preparation	8
2.1.3	Epitaxy	11
2.1.4	Deposition of dilute magnetic films	13
2.2	Scanning tunnelling microscopy	14
2.2.1	Basic principles of STM	15
2.2.2	STM-Theory of Tersoff and Harmann	15
2.2.3	Low temperature STM	17
3	Electron propagation in real space	19
3.1	STM topographies of buried impurities	20
3.2	Electron propagation in the crystal lattice	22
3.2.1	The single electron propagator	22
3.2.2	G of anisotropic media, electron focusing	25

3.2.3	Calculating G of the Host	29
3.3	Interaction: single impurity scattering	34
3.3.1	The t-matrix	34
3.3.2	LDOS in the vicinity of a single impurity	35
3.4	Detection	37
3.4.1	Vacuum LDOS at different distances - a first approach	38
3.4.2	Implementing a semi-infinite crystal geometry	41
3.4.3	Impact of the tip quality	45
3.4.4	Impact of the tunnelling resistance	48
3.5	Comparison between experiments and calculation	50
3.5.1	Data processing and fitting	51
3.5.2	Defects below the Cu(100)-surface	53
3.5.3	Defects below the Cu(111)-surface	54
3.5.4	Reconstruction of the propagator from STM-data	58
3.5.5	Comparison with <i>ab-initio</i> calculations	59
4	Kondo Effect of subsurface magnetic atoms	61
4.1	Phenomenology	62
4.2	Energy dependence of $\rho(\mathbf{x}, \varepsilon)$ near an impurity	63
4.2.1	Resonant impurity scattering and Fano line shapes	63
4.2.2	$\rho(\mathbf{x}, \varepsilon)$ in Copper	73
4.3	Scanning Tunnelling Spectroscopy	78
4.3.1	Multi bias spectroscopy	80
4.3.2	$I(V)$ - spectroscopy	80

<i>CONTENTS</i>	V
4.3.3 STS normalization	84
4.4 Topographies at different bias voltages	86
4.5 STS of subsurface impurities	94
4.5.1 Fe impurities	95
4.5.2 Co impurities	98
4.5.3 Comparison of the fitting results	98
4.5.4 Discussion of the experimental findings	103
4.5.5 Background scattering	105
4.5.6 Experimental determination of $t_{imp}(\varepsilon)$	108
5 Outlook	113
6 Summary	119
A Computational details: LCAO	121
B The real part of G_0	131
C List of Abbreviations	137
Literature	146
Danksagung	147
Lebenslauf	149

Chapter 1

Introduction

The coherent propagation of electrons in a given crystal potential is the underlying principle for a variety of effects in condensed matter physics. These include electron focusing, Friedel oscillations, Fermi-surface nesting, charge-/spin density oscillations, Ruderman-Kittel-Kasuya-Yosida interactions and the interlayer-exchange coupling among others. Historical developments and the wish to focus on that description which is most appropriate for the particular experiment are the main reasons for this Babel of nomenclature.

Apart from a different terminology the mentioned effects are usually described using different physical key-quantities. When investigating macroscopic electron transport through single crystals, explanations use the *group-velocities* $\mathbf{v}_{Gr} = \nabla_{\mathbf{k}}E(\mathbf{k})$ of the electrons. They are normal to the Fermi surface of the particular system. An accumulation of these vectors in a certain direction results in an enhanced electron flux. This is the so-called *electron focusing* [1]. Fermi-surface nesting is the prevalent mechanism explaining charge- and spin-density oscillations [2] like those that occur in interlayer exchange coupling structures. Such experiments are mainly interpreted by estimating extremal *callipering vectors* of a given system [3]. Single defects in solids lead to a disturbance that is minimized in energy by a rearrangement of the electron sea. This is the generic screening which Friedel [4] showed to be an oscillatory variation of the charge density $\langle n(\mathbf{x}) \rangle$ around the defect [5]. Within the free-electron model, the asymptotic oscillations depend only on the absolute value of the *Fermi wavevector* k_F . If a magnetic impurity scatters spin-up and spin-down electrons differently, the resulting spatial oscillatory behavior of spin-polarization is termed RKKY-oscillation [6, 7]. The underlying physics may be reduced to the difference $\langle \sigma_z(\mathbf{x}) \rangle = \langle n_{\uparrow}(\mathbf{x}) \rangle - \langle n_{\downarrow}(\mathbf{x}) \rangle$ of Friedel oscillations for each spin species.

Since all mentioned effects are related to the propagation of conduction band electrons they can be described using one unifying physical quantity: the quantum-mechanical Propagator [8] of the given system.

The work described in this thesis was initiated by an unexpected experimental observation. It was found by low temperature *Scanning Tunnelling Microscopy* (STM) that buried impurities produce highly anisotropic oscillations of the electron density at the surface. These oscillations appeared to be of long range and allowed an identification of single impurities placed more than 15 atomic layers below the surface. We will show that the characteristic signatures are related to the shape of the conduction-electron Propagator which is directly associated with the geometry of the Fermi surface of bulk electrons.

In the first part of this thesis we will analyze how the Fermi surface is linked to the interference patterns of the subsurface defects. An impurity which is incorporated in a metal leads to a rearrangement of the surrounding electrons. This results in an oscillatory behavior of electron density versus distance. This concept of Friedel oscillations can be commonly found in standard textbooks but the description is exclusively performed on isotropic systems using the dispersion of a free electron. It is well known that the band-structure of *every* material deviate from a free-electron dispersion. There are only a few examples in nature, where a nearly isotropic, free-electron-like dispersion is found. Examples are the 2D surface states on (111) surfaces of noble metals [9]. These simple cases attract particular attention in the scientific community, because they can be understood using basic textbook knowledge only.

Since the vast majority of elements has an anisotropic electronic structure, *anisotropic Friedel oscillations* are expected in every material. This generalization to realistic systems has been developed decades ago [10, 11]. However the physical understanding of anisotropic Friedel oscillations has not become a matter of common knowledge yet. Although the oscillations of charge density near an impurity are ground-states properties of the perturbed system (ideal host + impurity), they may be viewed as a scattering experiment of the unperturbed eigenstates at the impurity. The necessary physical concepts for a proper description can be found in scattering theory [12]. The wave function of an incoming electron interferes with the scattered (outgoing) wave and produces a standing wave pattern, i.e. a stationary modulation of the probability density. Thus the physics can be described by two sub processes: i) the *propagation* of the electrons before and after the collision and ii) the *interaction* of the electrons with the impurity potential.

The first process changes dramatically if an electron propagates within different crystal potentials. This will be discussed in detail later but we will already give

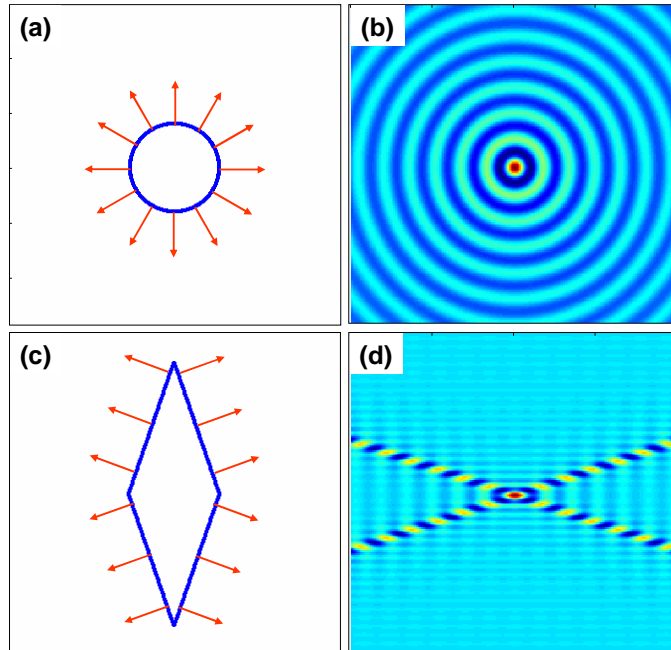


Figure 1.1: *Different k -space geometries of the Fermi surface (a,c) cause different shapes of the "Huygens"-wave (b,d) in real space. A spherically symmetric Fermi surface (a) leads to isotropic propagation (b) and hence to isotropic Friedel oscillations. If the FS is non-spherical (c), a standing wave pattern may be present only in certain directions (d) from the impurity (electron focusing).*

some illustrative examples here. The "Huygens" wave¹ is a well-known physical concept that describes the retarded propagation of probability amplitude from a point-like source. This propagation has been plotted in Figure 1.1 for two different model band structures: the isotropic system that is characterized by a spherical Fermi surface (blue contour, Fig. 1.1a) shows a spherically symmetric Huygens wave (Fig. 1.1b). In the second case (Fig. 1.1c), where the Fermi surface is anisotropic, the "Huygens"-wave of the electrons looks completely different and shows a preferred propagation in certain directions. The connection between these directions and the distribution of Fermi velocities (red arrows in Fig.1.1a,c) is obvious. This relates the Friedel oscillations to the *electron focusing* effect mentioned earlier.

The strongly directional propagation of electrons causes the anisotropy of the Friedel oscillations. Thus the first part of this thesis is to analyze the shape of the oscillations and to provide understanding of their connection to the band-structure of the host

¹we will use the term *single-particle Green function* or *Propagator* for this concept in the following

material.

In the second part of this thesis a new approach to the physics of Kondo-systems will be described. Systems of magnetic impurities in non-magnetic metals are known to show a variety of low-temperature anomalies, which are summarized by the term Kondo effect [13]. The most prominent experimental observation is an increase of resistivity when the temperature is decreased [14]. In a more microscopic picture it was shown [15] that a narrow many-body resonance (the Abrikosov-Suhl resonance [16]) builds up in the one-particle spectrum of the impurity at the chemical potential if the temperature is decreased below a specific temperature T_K , the Kondo-temperature. Since the charge transport is dominated by quasi-particles near the Fermi energy [17] and this resonance implies a strong scattering at the chemical potential, the behavior of the electrical resistance can be understood.

A strong scattering of conduction band electrons in turn results in large amplitudes of the standing wave pattern around the impurity. Furthermore it is well known from elementary quantum-mechanics that a scattering resonance produces an energy dependent phase-shift of the wave functions. The enhanced scattering amplitude and the phase-shift both impress the local density of states $\varrho(\mathbf{x}, \varepsilon)$, a quantity that can be measured by STM. Most of the experimental work concerning the Kondo Effect was performed on macroscopic systems and large ensembles of magnetic impurities. The development of the *Scanning Tunnelling Microscope* (STM) by Binnig and Rohrer [18] provided a new approach to the Kondo effect - the local spectroscopy of individual impurity atoms [19, 20]. This has been performed on magnetic atoms that have been *adsorbed* on a noble metal surface. A tunnelling spectrum taken directly above a Cerium atom showed a sharp anti-resonance at zero bias which was interpreted as the spectral signature of the Kondo Effect. Many other groups followed these pioneering experiments using different magnetic ad-atoms on several surfaces [21, 22, 23, 24]. All previous STM experiments showed that the spectroscopic signatures rapidly vanished if the tip is moved away from the impurity atom [25]. In contrast to this, theoretical work [26, 27] predicted a long range influence on the conduction electrons.

In this thesis we approach the Kondo Effect from a conduction-band electron's "point of view" as the magnetic impurities were buried below the surface. Different depths of the impurities below the surface correspond to different distances between the impurities and the STM tip. Our analysis combines two physical concepts that are normally treated separately. One of them is usually discussed in real-space. It is the oscillatory behavior of charge density ("Friedel oscillations") [4] in the vicinity of an impurity. The second concept is spectroscopy which in general measures physical quantities only versus energy. These experiments either average over large length scales or are only sensitive to specific aspects of the experimental system

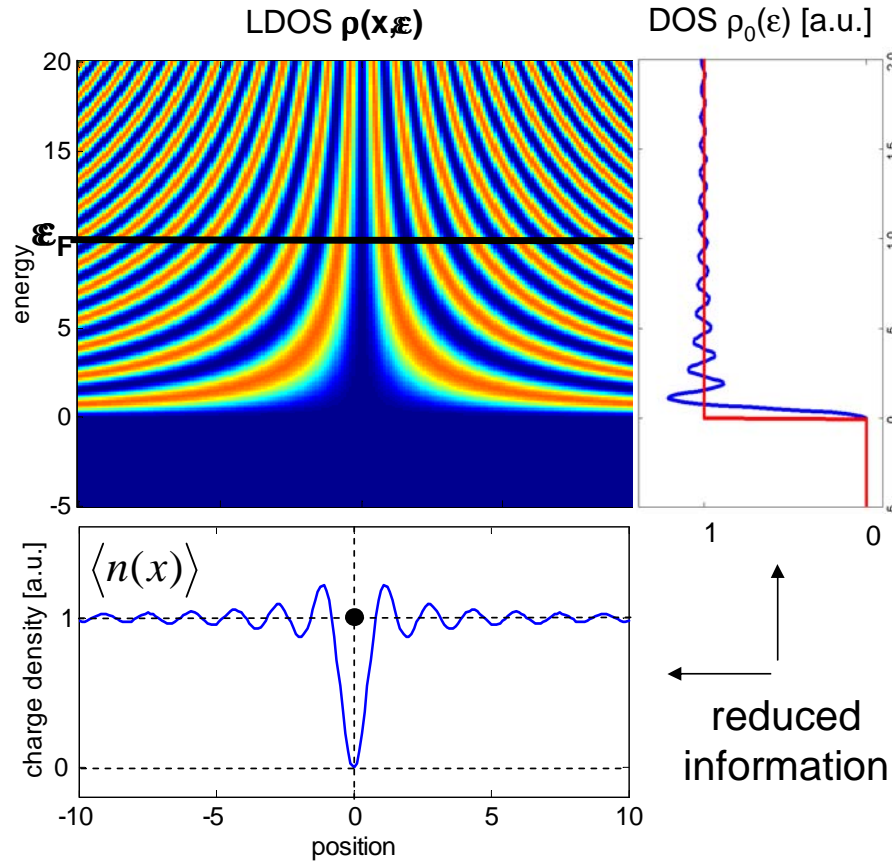


Figure 1.2: *Local density of states in the vicinity of an infinitely strong point scatterer at $x = 0$ within a one-dimensional electron gas having linear dispersion. The charge-density $n(x)$ shows Friedel oscillations. The oscillations in the DOS (blue curve) will converge towards the red curve for large systems.*

(e.g. core levels). If a tunnelling spectrum is recorded with the STM-tip placed at specific position only (e.g. direct above a magnetic adsorbate), information about the spatial distribution of spectral density is not obtained.

This is demonstrated in Figure 1.2. It shows the example of an infinitely strong repulsive point scatterer that is placed in a one-dimensional electron gas.² The local density of states $\rho(x, \varepsilon)$ describes the sum of probability densities $|\Psi_\nu(x)|^2$ of all states at a certain energy ε . It shows oscillations, whose spatial periodicity depend on the energy (as expected from the chosen dispersion relation). The charge density $\langle n(x) \rangle$ is the integral of this quantity including all energies up to the Fermi energy

²for simplicity we assumed a linear dispersion in order to avoid divergencies in the density of states.

ϵ_F . If integration is performed over the spatial dimension, this yields the density of states $\varrho_0(\epsilon)$. It is obvious that both quantities $\langle n(x) \rangle$ and $\varrho_0(\epsilon)$ contain less information than $\rho(x, \epsilon)$.

We noted earlier that the Kondo Effect is characterized by a strong scattering of quasi-particles near the Fermi energy. A strong scattering will result in an enhanced amplitude of the LDOS-oscillations in this energy range. Since the STM has access to the spatial and the energetic dimension of $\varrho(x, \epsilon)$, it should be observable. Thus we will use the STM to study the behavior of subsurface impurities versus energy and analyze whether a scattering resonance can be observed. This will be done in Chapter 4. Using a theory that will be developed in Chapter 3 we will extract the energy dependence of scattering amplitudes and phase-shifts from the STM-data. We will show that both show indeed strong Kondo signatures.

In Chapter 2 the sample preparation and the low-temperature STM will be shortly described. Chapter 3 will concentrate on the spatial dimension of the LDOS, while the regarded energy is fixed to the chemical potential. We will focus on the oscillations in the spectral density of the conduction band electrons and combine experimental and theoretical methods to demonstrate that these oscillations are strongly anisotropic if the Fermi surface of the host material is not spherical. We show that the electron density around the impurity is modulated only in very narrow directions linked with regions of small curvature on the Fermi surface. In Chapter 4 the Kondo Effect will be accessed. For this we have to analyze the energy-dependent behavior of the system. Since the Kondo resonance of Fe impurities in copper is extremely narrow, a strong change of the STM patterns can be observed very close to zero-bias. We will perform scanning tunnelling spectroscopy versus position and energy. In Chapter 5 some possible applications and the connection to other physical effects will be discussed. In particular, we will show that the strong directional propagation of electrons can be used to study buried interfaces. Chapter 6 will give a short summary of this thesis.

Chapter 2

Experimental setup

The task of this work is to prepare isolated magnetic atoms beneath a noble metal surface and to investigate their influence on the surrounding electronic structure by Scanning Tunnelling Spectroscopy at low temperatures. This chapter will give a brief description of the experimental setup and provide specific information about the preparation procedures.

2.1 Sample preparation

Both components, the host metal and the impurity material were deposited on a clean single crystal substrate using two electron beam evaporators. One of them, operating at moderate fluencies (≈ 1 layer/min), performs a homo-epitactical growth of the matrix material. The second one, kept at much lower deposition rates, carries out an admixture of the impurity atoms at specific times during the growth process by *pulsed* shutter operation.

The preparation has to meet several requirements. In order to avoid a coupling between the individual impurities and to keep their STM-signatures discriminable, low dopant concentrations are needed. Furthermore the number of residual (unwanted) impurities has to be kept far below these concentrations so that a clear attribution of the observed signatures to the added chemical element is possible. Finally the surface has to contain large, atomically flat terraces in order to obtain well-defined tunnelling geometries. Therefore the preparation has to be performed under *ultra high vacuum* (UHV) conditions using high purity evaporants and a carefully cleaned substrate.

2.1.1 UHV metal epitaxy chamber

The sample preparation was carried out in a mobile UHV chamber that is attachable to various scanning tunnelling microscopes as well as to a stand-alone LEED/AES (*low energy electron diffraction/Auger electron spectroscopy*) characterization unit. It allows an immediate transfer of the prepared samples to the subsequent experiments without breaking the vacuum. UHV is achieved using a 530 l/s turbo-molecular pump and a LN_2 cooled titanium-sublimation pump. 24 hours after bake-out a base pressure of $p < 5 \cdot 10^{-11}$ mbar is achieved that can be temporarily lowered to $p \approx 2 \cdot 10^{-11}$ mbar by sublimation of titanium.

The chamber is equipped with multiple facilities for UHV sample preparation allowing ion bombardment and the deposition of up to three materials at variable substrate temperatures. A CF250 cluster flange at the bottom of the chamber carries a Ar^+ -ion sputter source (IQE11/35 by SPECS, Berlin), three electron-beam evaporators (e-beam by TECTRA, Frankfurt), and a pyrometer (IM120 by IMPAC, Frankfurt) for non-contact temperature monitoring during the preparation. The sample is placed centrally in the chamber and can be positioned using xyz-micrometer drives. It is attached to a device allowing LN_2 -cooling and sample heating by electron bombardment or resistive heating. Additionally it provides six electrical contacts to the multi-segment sample holder. In our case one of these contacts was used to apply a high voltage to the sample in order to perform electron-beam heating. Detailed information about the sample preparation chamber can be found in [28, 29].

2.1.2 Single crystal preparation

One of the most important prerequisites for a well defined epitaxial film growth is a clean and atomically flat substrate surface. Additionally it is desired to reduce the number of residual impurities close to the surface. A comprehensive review of different preparation procedures to obtain such conditions for a variety of materials can be found in [30]. Concerning the cleaning process of the single crystal we conformed to the described procedures.

Substrate material

For the experiments we used single crystals of copper that were commercially acquired from MATECK, Jülich. They were 1 mm in thickness and fabricated in a hat-like shape with diameters of 8.5 mm and 6 mm respectively. The surfaces were

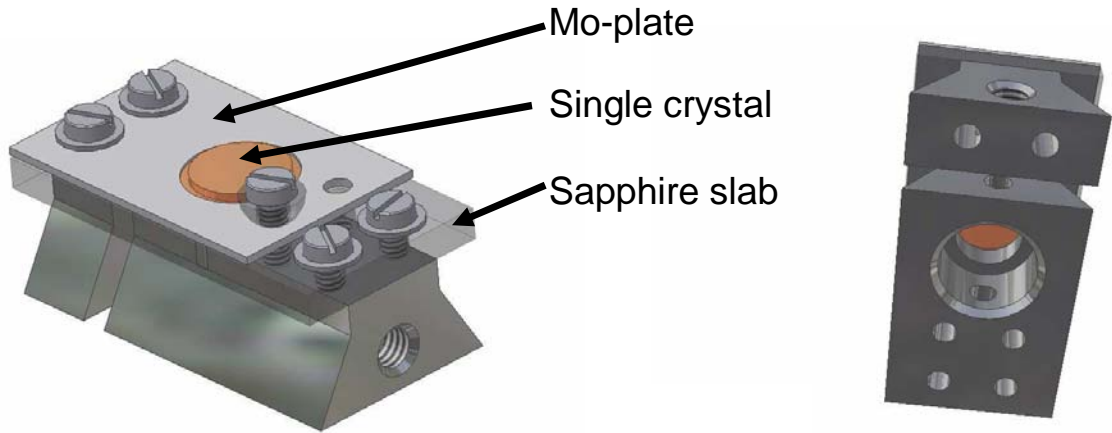


Figure 2.1: *Constructional sketch of sample holder*

oriented normal to the $[100]$ and $[111]$ directions with a accuracy $< 0.1^\circ$ and polished to a roughness $< 30nm$. An annealing procedure in a hydrogen/argon atmosphere was performed by the manufacturer to reduce the number of residual impurities (mostly sulfur and carbon).

Sample holder

The crystal was placed in a sample holder combining a good thermal contact to the cryostat with the electrical insulation necessary for electron beam heating. A molybdenum top plate gently presses the crystal onto a sapphire slab that is fixed on a multi-segmented, dovetail-shaped bar made of stainless steel. A picture of the sample holder can be seen in Figure 2.1. A hole in the bar and sapphire plate allows access to the reverse side of the crystal for electron bombardment.

To avoid contamination of the crystal surface by the sample-holder material (stainless steel, molybdenum) due to secondary sputtering effects during the cleaning procedure, the topmost parts of the sample holder were covered by multiple μm of copper. Additionally, due to the crystal's hat-shaped geometry, the crystal surface is placed above the Mo-plate avoiding direct particle trajectories between the sample holder and the crystal surface.

Ar⁺-ion bombardment

The single crystals were prepared by repeated cycles of Ar⁺-ion sputtering and subsequent annealing by electron-beam heating. The sputtering procedure was performed with 700eV ion-beam energy at a fluency of $2\mu A$ ion current hitting the sample holder. During the sputtering process the chamber pressure raised to $2 \cdot 10^{-6} mbar$ due to the inlet of argon gas. The initial ion bombardment was performed for two hours to remove the oxide film as well as residua of previous thin film depositions. The following repetitive sputtering periods were of 20 minutes duration.

Annealing

The annealing causes both a smoothing of the surface morphology producing large, atomically flat terraces and a segregation of bulk point-defects towards the surface. These can be removed during the subsequent sputtering process. Sample heating was performed by electron bombardment. A thoriated tungsten cathode was brought close to the back of the crystal. Filament currents I_{Fil} up to 6A led to thermionic emission of electrons that were accelerated onto the sample by an electrical field of 800 V. The filament current I_{Fil} was adjusted while monitoring both the emission current I_{em} and the substrate temperature. The crystal was heated to a temperature of 720 K for 10 minutes. For this purpose emission currents of $I_{em} \approx 15mA$ were sufficient according to a power of 12W applied to the crystal. A computer controlled closed loop feedback system provided constant sample temperature or constant e-beam power by adjusting I_{Fil} . The sample temperature was measured using a pyrometer with a selected emissivity of 11% that has previously been shown to be adequate [28]. In cases where substrate temperatures were below the detection limit ($160^{\circ}C$) of the pyrometer or if interfering IR-sources (operating evaporators, ...) were present, the primary control parameter was the e-beam power.

Substrate characterization

After 15 sputtering/annealing cycles the prepared surfaces were characterized by STM and LEED. An STM constant current topography of a freshly prepared Cu(100) surface can be seen in Figure 2.2a). It shows large, atomically flat terraces. This is confirmed by the LEED pattern showing very sharp diffraction peaks.

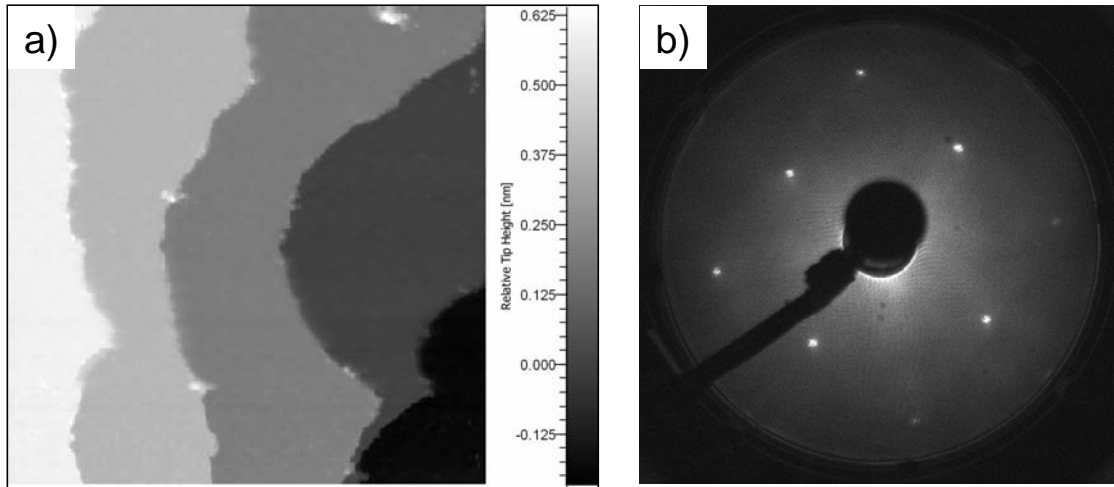


Figure 2.2: *Characterization of the prepared Cu(100) single crystal: a) STM image ($165\text{nm} \times 165\text{nm}$, 0.5 nA , 100 mV) of a freshly prepared substrate surface showing large, atomically flat terraces, b) a LEED pattern taken at 100 eV electron energy revealing sharp diffraction peaks.*

2.1.3 Epitaxy

After having achieved a clean and atomically flat substrate, thin films of dilute magnetic alloys were prepared using computer-controlled evaporator and shutter equipment.

Electron beam evaporators

The electron beam evaporators used here apply a high positive voltage V_{Ev} to the evaporant, which is either placed in a tungsten crucible (Cu) or directly evaporated from a rod (Co, Fe). Electrons, emitted from a surrounding thoriated tungsten filament are accelerated onto the crucible/rod and heat the evaporant. A fraction of the vapor-phase atoms is positively ionized by the electron beam. These are used for flux monitoring and detected by an electrode placed outside the evaporator (see Figure 2.3). In order to prevent ubiquitous electrons from compensating the positive charge of the ions, a negative voltage ($\approx -20\text{V}$) was applied to the flux electrode. Obtainable ion currents I_{Flux} are in the order of $1\text{nA} \dots 10\mu\text{A}$ and monitored by the computer. A feedback loop provided flux control by adjusting the filament current I_{Fil} .

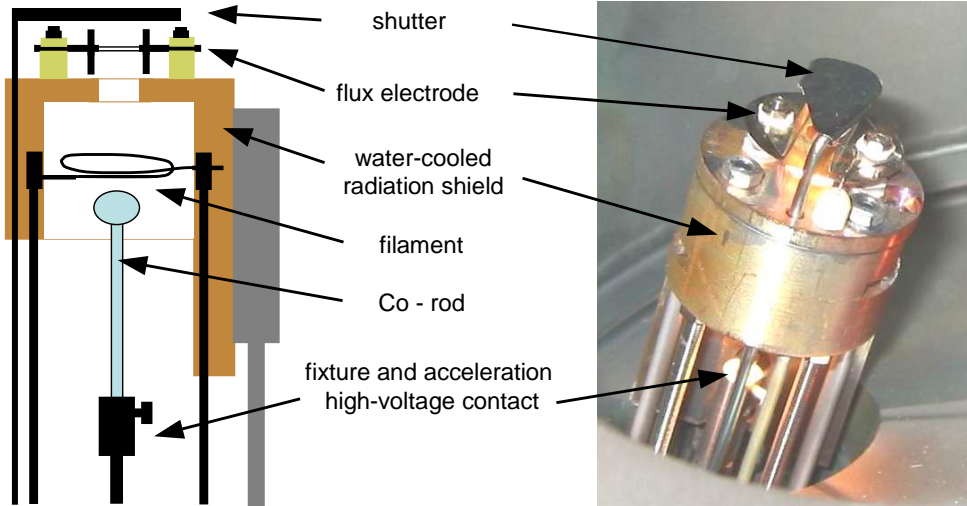


Figure 2.3: *Constructional sketch and image of the electron-beam evaporators used for the thin-film deposition*

As the ionization probability and therefore the fraction of ionized atoms is proportional to the thermionic emission current I_{em} , this parameter needs also to be considered. I_{em} was monitored by the computer and used as the primary control variable during heat-up, until a sufficient I_{Flux} was detected. It was taken care that calibration and deposition were performed at identical emission currents. The high voltage U_{Ev} was manually adjusted until the desired deposition flux was obtained at predetermined emission currents (20mA crucible, 12mA rod).

In previous experiments it turned out that the positively charged atoms, albeit helpful in controlling the deposition rate, have a negative impact on the morphology of the achieved films. They are repelled by the crucible and accelerated onto the sample causing ion currents at the sample holder of $\approx 1\mu A$ (in the case of Cu at 1ML/min). This is comparable to the currents obtained during the Ar^+ -bombardment and causes a significant sputtering damage resulting in a strongly enhanced surface roughness. These observations are described in detail in [31].

In the current experiments we avoided this ion bombardment by applying a high positive voltage to the crystal during the evaporation. The chosen voltage was higher than the voltage applied to the evaporants. In some sample preparations this high

voltage was also used for sample heating during deposition.

The evaporant materials have been purchased from ALFA AESAR and had specified purities of 99.995%(Co,Fe) and 99.9999%(Cu). Before the deposition, an out-gasing procedure was performed for several hours by slowly increasing I_{Flux} slightly above the targeted deposition flux. For the thin film deposition, the Cu evaporator was operated at $I_{Flux} = 1.3\mu A$, $I_{Em} = 20mA$, $U_{Ev} = 800V$ corresponding to 1ML/min. The impurity evaporators (Fe,Co) were kept at the lowest possible fluencies compatible with a stable flux control. We used ($I_{Flux} = 5nA$, $I_{Em} = 12mA$, $U_{Ev} = 800V$) corresponding to deposition rates of 0.05ML/min (Co) and 0.35ML/min (Fe), respectively.

For a further reduction of the impurity concentration, stepper motors were attached to the shutters allowing deposition times down to 50ms. These actuators were computer controlled assuring well-defined and reproducible deposition sequences.

2.1.4 Deposition of dilute magnetic films

A final sputtering/annealing cycle was performed after the out-gasing procedure with both evaporators on temperature. The annealing step was shortened to 5 minutes and was lower in temperature (670K) to avoid surface contamination due to a segregation of bulk defects. The film preparation started with a deposition of 10ML of pure copper. Thereafter the impurity metal was added in the topmost 10-15 ML. Within 30 minutes after film deposition the samples were transferred into the LN_2 pre-cooled STM-cryostat. The final cool down to 5K was performed after un-docking the mobile metal epitaxy chamber within 90 minutes after preparation.

The applied deposition sequences and substrate temperatures varied for the different prepared systems:

Co in Cu(100)

The best results were obtained by heating the crystal with an e-beam power of 3W during deposition. As the temperature was below the detection threshold of the pyrometer (160°C) a constant-power feedback was required for sample heating and the prevailing sample temperature is unknown.

Fe in Cu(100)

Preparing isolated subsurface iron atoms turned out to be a much more challenging task because iron atoms have a much higher diffusibility in copper than cobalt atoms. First preparation attempts resulted in a high number of Fe clusters in the surface layer similar to those reported by [32].

Therefore the crystal was cooled down to 80K prior to deposition. The film was grown onto the cold substrate with additional 5ML of pure copper on top. In order to achieve a flat surface, the film was shortly annealed by heating up the sample using an e-beam power of 30W until the pyrometer indicated a temperature $T > 160^{\circ}\text{C}$. Then the power was reduced to 6W for 30 seconds and the sample was immediately cooled down to 80K afterwards. Although a significant number of Fe impurities stayed isolated below the surface and could be successfully analyzed, several Fe-clusters were still observed in the surface layer. Thus, the procedure still has room for improvement.

Co in Cu(111)

The experimental data of Co in Cu(111) presented in this thesis were prepared using higher Cu-fluencies ($3\mu\text{A}$) and without simultaneous sample heating. Details on the preparation can be found in the Ph.D thesis of *Quaas* [28, 29].

2.2 Scanning tunnelling microscopy

The Scanning Tunnelling Microscope is the most powerful tool to investigate the morphology and the electronic structure of conductive solid surfaces in real space with atomic resolution. It was developed in 1981 by Binnig and Rohrer [18] who received the Nobel-prize in physics five years later. A comprehensive introduction in scanning tunnelling microscopy can be found in [33] [34]. Here we will give a brief description of the basic principles, the specific setup and the STM-Theory of *Tersoff* and *Harmann*. An introduction in *Scanning Tunnelling Spectroscopy* (STS) as well as the description of the different graphical STS-representations used in this thesis can be found in Chapter 4.3.

2.2.1 Basic principles of STM

In an STM, a sharp metal tip is brought in close proximity to the sample surface resulting in an overlap of tip and sample wave functions. This causes nonzero transmission probabilities of electrons so that an applied bias voltage V_T results in a net current I_T (usually nA). This tunnelling current is very sensitive to the tip-sample distance h and is stabilized using piezo-ceramic actuators and a closed-loop control.

The acquisition of two-dimensional images is performed by scanning the tip laterally. In this work we exclusively used *constant current mode* where the tip-sample distance h is continuously adjusted in order to keep I_T constant. This mode provides contours $h(\mathbf{x}_{\parallel})$ of constant I_T at every scan-point $\mathbf{x}_{\parallel} = (x, y)$. $h(\mathbf{x}_{\parallel})$ contains *structural information* about surface e.g. mono-atomic steps, dislocations as well as the atomic lattice. An example can be seen in Figure 2.2a), where information about the size of mono-atomic terraces was extracted from constant current topographies. For this thesis the morphology of the surface was of secondary importance while the STM-signatures originating from the *electronic structure* of the sample were of primary interest. Above areas of reduced electron density the tip has to be moved closer to the surface to obtain the set tunnelling current. In contrast the tip will be retracted above regions of increased electron density. More precisely it is only a small spectral fraction of the charge density that contributes to the tunnelling current and thus influences $h(\mathbf{x}_{\parallel})$. This fraction is sensitive to the chosen bias voltage V_T which allows the extraction of *spectroscopic information*.

2.2.2 STM-Theory of Tersoff and Hamann

Shortly after the development of the Scanning Tunnelling Microscope by *Binnig* and *Rohrer* in 1981, *Tersoff* and *Harmann* presented a theory to explain the physical information contained in STM-topographies. They based their theory on the work of *Bardeen*, presented in 1961 who had described planar tunnelling devices using first order perturbation theory. The transitions of electrons across the tunnelling junction take place from filled tip-states Ψ_{μ} into empty sample states Ψ_{ν} and from filled sample states into empty tip states. Using the Fermi distributions $f(\varepsilon) = (1 + \exp(\varepsilon/k_B T))^{-1}$ for tip and sample the tunnelling current I can be derived using Fermi's golden rule:

$$I = \frac{2\pi}{\hbar} e^2 V \sum_{\mu, \nu} |M_{\mu\nu}|^2 (f(E_{\mu} - \epsilon_F^{(T)}) - f(E_{\nu} - \epsilon_F^{(S)})) \delta(E_{\nu} - E_{\mu} - eV) \quad (2.1)$$

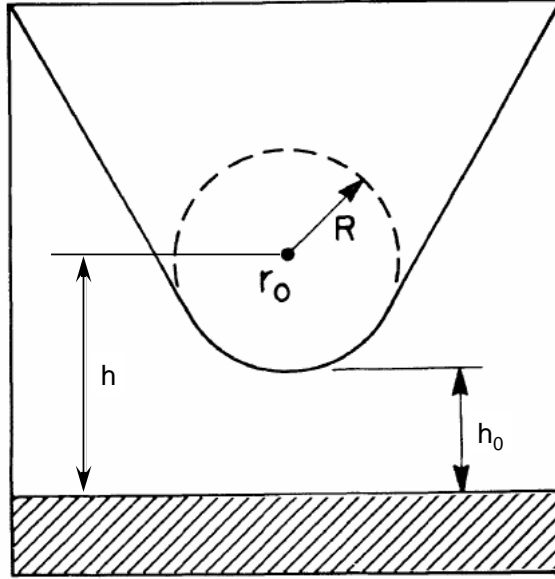


Figure 2.4: Schematic picture of the tunnelling geometry taken from [35]. Of importance for the interpretation of STM-images is the surface LDOS at position r_0 - well within the STM-tip

For low temperatures and low bias voltages only states at the Fermi energy contribute to the tunnelling current. An expression for the tunnelling matrix element $M_{\mu\nu}$ was derived by Bardeen [36]:

$$M_{\mu\nu} = \int_{\Omega} d\vec{S} \Psi_{\mu} \nabla \Psi_{\nu} - \Psi_{\nu} \nabla \Psi_{\mu} \quad (2.2)$$

where the integral is performed over any surface Ω lying entirely within the gap region between tip and surface.

Tersoff and Hamann [35, 37] approximated the tip as an s-like wave function and calculated the matrix element for a tip-sample geometry shown in Fig. 2.4. They related the tunnelling current to the *local density of states* (LDOS) of the sample

$$\rho(\mathbf{x}, \varepsilon) = \sum_{\alpha} |\Psi_{\alpha}(\mathbf{x})|^2 \delta(\varepsilon - E_{\alpha}) \quad (2.3)$$

Although the integration contour Ω is located anywhere *between* tip and sample, the final expression contains only the *sample LDOS* at position r_0 , i.e. in the middle of the STM-tip:

$$I \propto V \phi_{\rho_t}(\epsilon_F) R^2 \kappa^{-4} e^{2\kappa R} \rho(r_0, \epsilon_F) \quad (2.4)$$

With $\varrho(h) \propto e^{-2\kappa h} = e^{-2\kappa(h_0+R)}$ this gives a current $I \propto R^2 e^{-2\kappa h_0}$. This current is proportional to the surface area of the tip ($\propto R^2$) and decays exponentially with increasing distance h_0 between tip and sample. Thus if the LDOS at the position of the tip changes from $\varrho_0(\mathbf{x}, \varepsilon_F)$ to $\varrho_0(\mathbf{x}, \varepsilon_F) + \Delta\varrho(\mathbf{x}, \varepsilon_F)$ this is compensated by a change of the tip-sample distance:

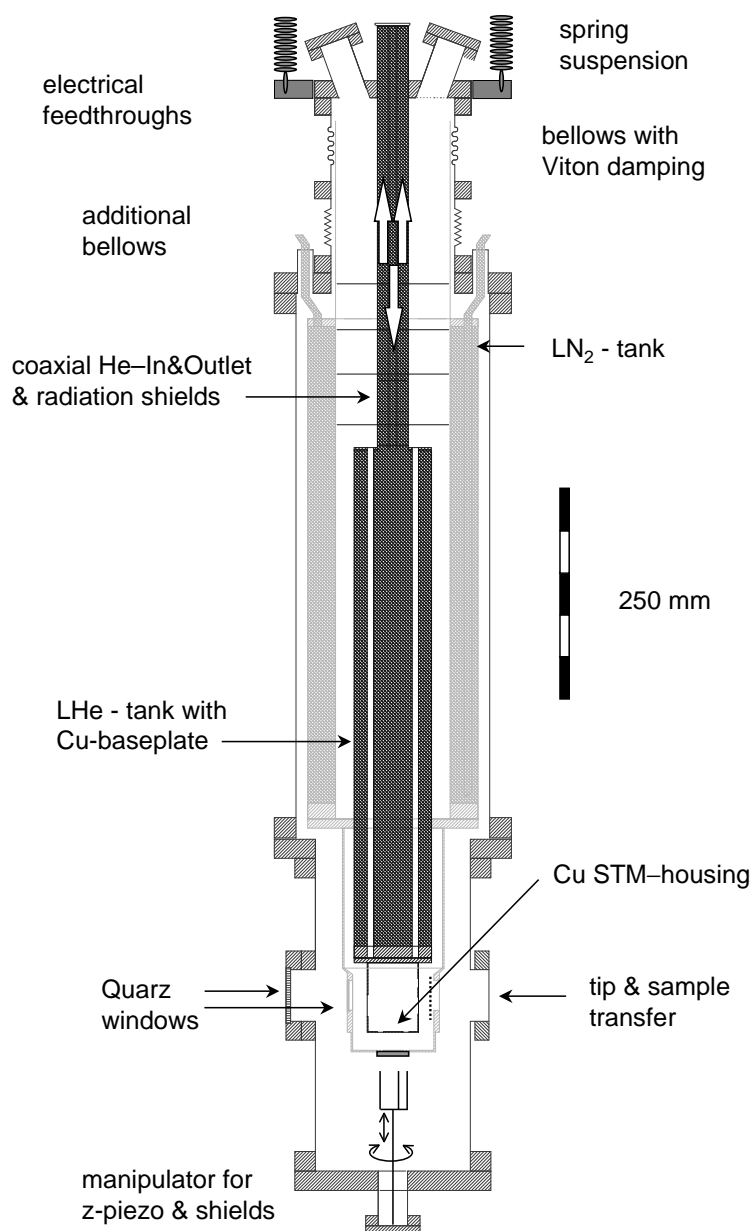
$$\Delta h(\mathbf{x}_{\parallel}) = \frac{1}{2\kappa} \ln \left(1 + \frac{\Delta\varrho(\mathbf{x}_{\parallel}, \varepsilon_F)}{\varrho_0(\varepsilon_F)} \right) \approx \frac{\Delta\varrho(\mathbf{x}_{\parallel}, \varepsilon_F)}{2\kappa\varrho_0(\varepsilon_F)} \quad (2.5)$$

The last approximation holds only for $|\Delta\varrho| \ll \varrho_0$. Using a work function of 4eV a variation of LDOS by one decade results in a 1Å change of the tip-sample distance. The normalization $\Delta\varrho/\varrho_0$ will be commonly used in the next chapters.

2.2.3 Low temperature STM

The experiments presented in this thesis were performed using a custom-built low temperature STM working at 5K. The construction of the STM-cryostat is depicted in Figure 2.5. The core is a Besocke-type [38] piezo-unit, attached to a liquid helium (LHe) bath cryostat. The LHe-tank is a spring-suspended, Viton damped pendulum surrounded by a liquid-nitrogen cooled vessel, shielding the heat radiation. The setup allows optical access and *in-situ* tip and sample exchange[39, 40]. STM-scanner and sample support are thermally coupled to the LHe-tank using sapphire plates and Indium foil. The tip is coupled to the cryostat using several thin silver wires. Temperature at the sample support can be monitored using a CernoxTM-sensor. Temperatures of 5.4K are commonly achieved with one LHe filling lasting for a time period of 20 hours.

The STM-tips were electro-chemically etched from a 250 μm tungsten wire in a KOH solution. Inside the UHV they were electrically heated to $\approx 1000\text{K}$, sputtered with 4keV Ar^+ ions and characterized by field-emission. A detailed description of the tip preparation including a SEM (*Scanning Electron Microscopy*)-study of the achieved apex-radii can be found in [41].

Figure 2.5: *low temperature STM*

Chapter 3

Electron propagation in real space

In this chapter, the influence of isolated subsurface impurities on the *Local Density of States* at the surface is discussed. For convenience, we will start with the description of *experimental facts* (3.1). For this we will have a look at a few STM measurements of single subsurface cobalt and iron atoms in copper, which will later be analyzed in detail. The subsequent task is to theoretically understand the observed signatures and to develop a model that reproduces the STM-measurements. This process will be conceptually divided into three underlying processes. First of all we will regard the *propagation* (3.2) of conduction band electrons within the unperturbed crystal potential of the host metal. In particular we will discuss the influence of anisotropies within the host metal's band structure on the propagation. While the band structure is a property of the bare host metal the insertion of an impurity atom causes perturbations within the host, which will be treated as an *interaction* (3.3) of the otherwise unperturbed conduction band electrons with the impurity potential. The third process is the *detection* (3.4) of the LDOS modulations with the STM. Since the tip is positioned a few Ångströms above the surface and is of finite width, the results of the STM measurements are affected by the properties of the tip and the tunnelling junction. After having discussed these three processes a *comparison* (3.5) between experiments and calculations will be performed allowing a depth classification of the experimentally observed defect patterns. The influence of the spectral properties of the impurity on the LDOS at the surface will be discussed in the next chapter.

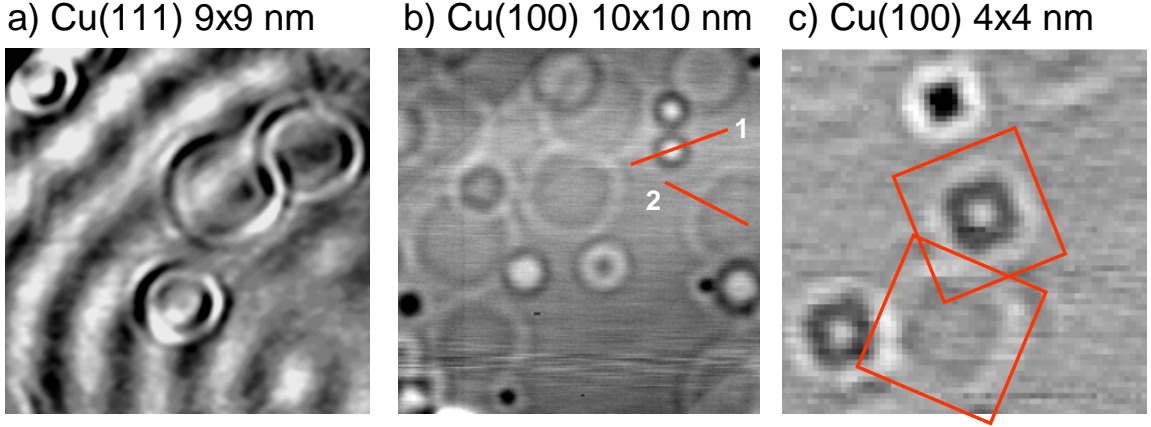


Figure 3.1: *STM Topographies of subsurface Co-impurities buried in different depths below the (111)(a) and (100)(b,c) surfaces of copper. The used tunnelling parameters were a) $V_T = -80\text{mV}, I_T = 1\text{nA}$, b) $V_T = 10\text{mV}, I_T = 0.8\text{nA}$, c) $V_T = -50\text{mV}, I_T = 1\text{nA}$. Red lines in b) indicate the positions of the cross-sections analyzed in Fig. 3.2. The orientation of the patterns arising from deeply buried defects is rotated by 45° compared with those of surface-near impurities (red squares in c).*

3.1 STM topographies of buried impurities

It is known from the Thomas-Fermi theory of screening [42] that defects incorporated in metals are screened within distances of a few \AA . Applied to copper, the host metal of the systems prepared in this work, a screening length of $r_{TF} = 0.55\text{\AA}$ is obtained. This is much shorter than the inter-atomic distance (2.55\AA). From this, it appears quite questionable whether impurities buried up to 15 layers ($\approx 30\text{\AA}$) below the surface are causing any perturbations that can be detected with the STM.

In strong contrast to this expectation the experimental findings reveal that the impurities can be clearly identified in the STM-measurements. Fig. 3.1a) shows a $9\text{nm} \times 9\text{nm}$ image that illustrates the influence of different Co atom depths (6,7,9 and 10ML) below the Cu(111)-surface on a constant current topography. Two major observations can be made here: i) a long-wavelength standing wave pattern caused by surface state electrons that are scattered at a mono-atomic step-edge in the upper left corner and ii) four ring-like structures, corresponding to short-wavelength oscillations with an amplitude of about 2pm . They vary in diameter but are constant in their radial envelope width (≈ 1.5 oscillations). The long-wave modulations of the surface-state electrons are unperturbed by the impurities. Since the LDOS of the surface state electrons decays into the crystal within the first five atomic layers [43], it can be concluded that the impurities must be positioned below the 5th

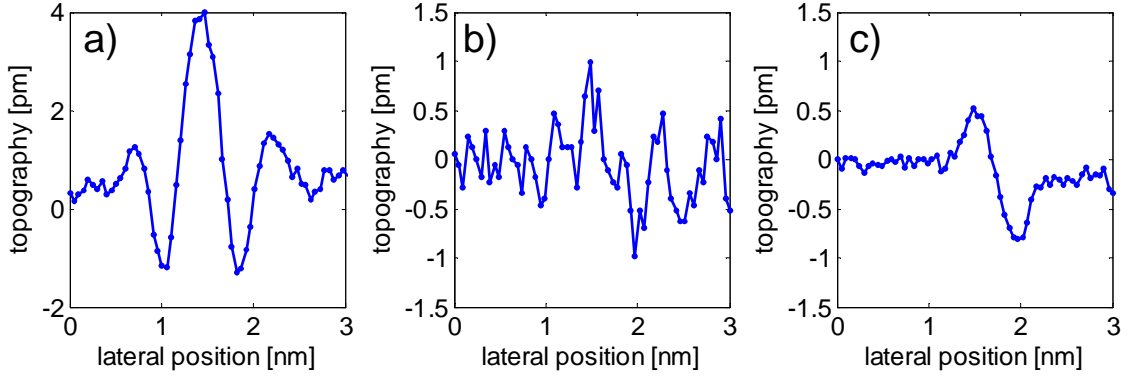


Figure 3.2: *Cross-sections of the defect patterns depicted in figure 3.1b : a) defect close to the surface (section 1) b): raw data of a deeply buried impurity (section 2) - defect signature below the noise level c): same defect but after averaging 20 parallel scan lines shows 500fm modulations of the tip-sample distance.*

layer. It will be proven later that the features having a larger diameter correspond to impurities buried deeper below the surface. Therefore the LDOS seems to be unmodified within a certain angle above the impurity.

Fig 3.1 b) and c) show the patterns induced by subsurface Co atoms that are buried below the Cu(100) surface. Here fourfold symmetric patterns are observed. For the deeply buried defects (large patterns in Fig. 3.1 b)) the electron density seems to be little influenced directly above the defect. The orientation of the features arising from deep defects seems to be rotated by 45° compared with the pattern arising from the impurities being closer to the surface (Fig. 3.1 c)).

Although clear signatures of the impurity atoms can be identified, the measured STM-signals are very weak. This can be seen in figure 3.2. The variations of tip-sample distance arising from the deepest defects (section 2 in Fig. 3.1b) are about 500fm and therefore 400 times smaller than the height of a mono atomic step. It is a good rule of thumb for the interpretation of STM-data that (assuming a work function of 4eV) a change of the tip-sample distance of 1\AA results in a variation of tunnelling current by one decade. Consequently, the LDOS modulations that cause a 500fm change of tip-sample distance are in the order of 0.6%.

We can summarize that subsurface impurities in copper produce short wavelength LDOS oscillations with a significant anisotropy in the STM-topographies. Especially at larger distances from the impurity atoms, the LDOS is influenced only in narrowly confined directions from the impurity atom. From the short wavelength and the characteristic symmetry of the observed patterns we conclude that the os-

cillations are due to scattering of bulk electrons at the subsurface defects, which produce a standing wave pattern in their vicinity. Therefore the physics behind these observations should be found in the band structure of the host metal. This connection between the band structure and the characteristic shapes of the observed LDOS-patterns will be elucidated in the following.

3.2 Electron propagation in the crystal lattice

”If you want to learn about nature, to appreciate nature, it is necessary to understand the language that she speaks in.”

Richard P. Feynman

From the symmetry and the short wavelength of the described impurity signatures it is evident that the band structure of the host metals has a major impact on the observed patterns. We will now show that the shape of the observed patterns is directly connected to a fundamental property of electronic structure, the quantum-mechanical propagator or single-particle Green function G . After a short introduction in the physical meaning of G we will show the relationship between G and the Fermi surface (FS) of a particular system. The impact of crystal anisotropies on the propagation of electrons will then be discussed using simple toy models. In order to correctly describe the propagation in the host metal of our experimental systems, the band structure and the propagator of copper are then calculated using an LCAO (*linear combination of atomic orbitals*) approach.

3.2.1 The single electron propagator

In physics there exist different variants of Green functions and hence countless possibilities to introduce them. For a comprehensive review and formal deviations the reader is referred to literature [17] [12]. We will use the most general definition of the single particle Green function:

$$G_{\lambda,\nu}(t-t') = -i\langle |\mathcal{T}c_{\lambda}(t)c_{\nu}^{\dagger}(t')| \rangle \quad (3.1)$$

The expectation value in the above expression has to be calculated using the ground-state. The operators c/c^{\dagger} annihilate/create a particle in a state with quantum number λ/ν at time t/t' ; \mathcal{T} is the time-ordering operator. If c^{\dagger} acts prior to c ($t' < t$), $G_{\lambda,\nu}$ describes the propagation of a *electron* from state ν to λ . Otherwise,



Figure 3.3: *wave propagation in an isotropic system*

if an electron is removed from the ground state and reinserted later ($t' > t$), the propagation of a *hole* is described. Only two Green functions are of particular interest in the context of this work. In the first one used in this chapter c^\dagger and c are the field-operators $\hat{\psi}^\dagger(\mathbf{x})/\hat{\psi}(\mathbf{x}')$ that create/annihilate an electron at a certain positions \mathbf{x}/\mathbf{x}' in the crystal. The second one will be used later and corresponds to a creation/annihilation of an electron in an impurity d-orbital using the operators c_d^\dagger/c_d . Throughout the following we will use the Fourier transforms with respect to the time $G(\mathbf{x}, \mathbf{x}', \varepsilon)$ and $G_{dd}(\varepsilon)$ respectively.

We now focus on the Green function $G(\mathbf{x}, \mathbf{x}', \varepsilon)$ of the conduction electrons. This property describes, how electrons of energy ε propagate from a point-source at \mathbf{x}' to other positions \mathbf{x} in the crystal. The ripple extending from a drop falling into still water (Fig. 3.3) and the Huygens wave in optics are examples of propagators in other fields of physics. The drop example corresponds to an excitation that is δ -like in space *and* time and would be described by the time-dependent Green function $G(\mathbf{x}, \mathbf{x}', t - t')$ of equation 3.1. Thus the corresponding analog for the energy-dependent propagator $G(\mathbf{x}, \mathbf{x}', \varepsilon)$ is the wave extending from a needle being continuously dipped into the water at position \mathbf{x}' with a constant angular frequency $\omega = \varepsilon/\hbar$.

The single electron propagator in vacuum is a spherical wave similar to the Huygens wave in free space or isotropic optical media. This is not the case if an electron propagates within a crystal potential. Using *spectral representation*, G can be expanded

using the eigenfunctions $\Psi_{\mathbf{k}}(\mathbf{x})$ and the band structure $E(\mathbf{k})$:

$$G(\mathbf{x}, \mathbf{x}', \varepsilon) = \lim_{\eta \rightarrow 0} \int_{\mathbf{k}} d^3k \frac{\Psi_{\mathbf{k}}(\mathbf{x}) \Psi_{\mathbf{k}}^*(\mathbf{x}')}{\varepsilon - E(\mathbf{k}) + i\eta} \quad (3.2)$$

We can gain further insight into implications of equation 3.2 by using the identity:

$$\frac{1}{\varepsilon - E(\mathbf{k}) + i\eta} \xrightarrow{\lim_{\eta \rightarrow 0}} \mathcal{P} \frac{1}{\varepsilon - E(\mathbf{k})} - i\pi \delta(\varepsilon - E(\mathbf{k})) \quad (3.3)$$

where \mathcal{P} denotes the principal value of the above integral. From this it can be seen that the local density of states (LDOS), that was defined in Chapter 2, is related to the imaginary part of G for $\mathbf{x} = \mathbf{x}'$

$$\rho(\mathbf{x}, \varepsilon) = \sum_{\mathbf{k}} |\Psi_{\mathbf{k}}(\mathbf{x})|^2 \delta(\varepsilon - E(\mathbf{k})) = -\frac{1}{\pi} \text{Im} G(\mathbf{x}, \mathbf{x}, \varepsilon) \quad (3.4)$$

The second conclusion that can be derived from equation 3.3 is that the imaginary part of the propagator can be expressed as a superposition of all wave functions having identical Energy ε

$$\begin{aligned} \text{Im} G(\mathbf{x}, \mathbf{x}', \varepsilon) &= -\pi \sum_{\mathbf{k}} \Psi_{\mathbf{k}}(\mathbf{x}) \Psi_{\mathbf{k}}^*(\mathbf{x}') \delta(\varepsilon - E(\mathbf{k})) \\ &= -\pi \sum_{\mathbf{k} \in \Omega(\varepsilon)} u_{\mathbf{k}}(\mathbf{x}) u_{\mathbf{k}}^*(\mathbf{x}') e^{i\mathbf{k}(\mathbf{x} - \mathbf{x}')} \end{aligned} \quad (3.5)$$

In the previous equation $u_{\mathbf{k}}(\mathbf{x})$ is the lattice-periodic part of the Bloch functions. One can see that the G is directly associated with the geometry of the corresponding iso-energy surface $\Omega(\varepsilon)$ because the δ -function selects only those states having the correct energy ε . Thus the shape of the Fermi surface (FS) is of particular interest if the propagation of electrons at the Fermi energy ε_F is considered.

In the following we will neglect the lattice-periodicity of the wave functions $u_{\mathbf{k}}(\mathbf{x}) = 1$. This will cause the propagator to depend only on the difference vector $\mathbf{x} - \mathbf{x}'$. If $u_{\mathbf{k}}(\mathbf{x})$ is only weakly varying with \mathbf{k} , our approach would describe an envelope function of the exact propagator. If the variation of $u_{\mathbf{k}}(\mathbf{x})$ across the iso-energy surface is significant, one possibility would be to expand the lattice periodic part in terms of atomic wave functions similar to the LCAO ansatz that will be used later to determine $E(\mathbf{k})$ of copper (section 3.2.3). This would lead to a matrix equation for G , similar to those obtained within a KKR (*Kohn, Koringa, Rostocker*) formalism [44]. However, we leave this part to the *ab-initio* experts (see 3.5.5) and will maintain this simplifying assumption throughout the following.

3.2.2 G of anisotropic media, electron focusing

We will now demonstrate how the propagation of electrons is influenced by the shape of the Fermi surface using a few illustrative examples. With $u_k(\mathbf{x}) = 1$ our system gained full translational invariance instead of lattice periodicity - it is now homogeneous but may still possess anisotropies. We can set the position of the source to the origin $\mathbf{x}' = \mathbf{0}$ and analyze the interrelation between the shape of the propagator and the geometry of several fictitious iso-energy surfaces. For simplicity, this is performed in 2 dimensions. Furthermore we concentrate on the imaginary part of the propagator and assume that (within a band) the main characteristics (wavelength, directional dependence, spatial decay...) can already be derived from the $\text{Im}G$. A more detailed discussion of $\text{Re}G$ can be found in Appendix B.

Since the imaginary part (equation 3.5) is a simple *superposition* of plane waves, the mechanism behind all effects elucidated in the following is constructive and destructive *interference* of eigenfunctions.

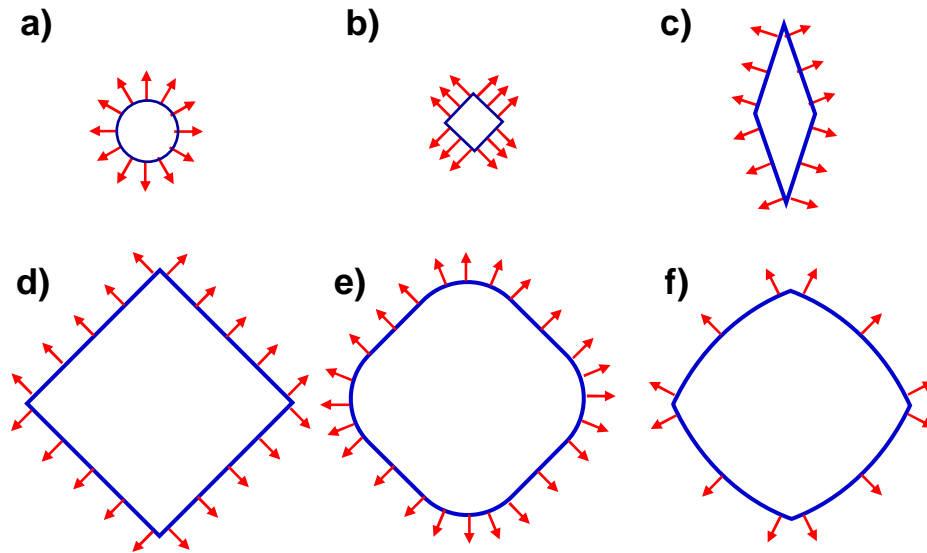
Model Fermi surfaces

We start the discussion with an isotropic band structure. In this case the Fermi surface is a sphere with radius k_F , and the corresponding Green function is a spherical wave decaying with $|\mathbf{x} - \mathbf{x}'|^{-1}$ in amplitude ($|\mathbf{x} - \mathbf{x}'|^{-1/2}$ in 2 dimensions) [Fig 3.4a]. For the vast majority of crystals the Fermi surface deviates from a spherical shape. Interesting effects can arise in this case, which will be demonstrated using rather extreme FS geometries.

In the most extreme case (Fig. 3.4b) where the Fermi surface is composed of flat areas¹, the wave functions of equation 3.5 interfere constructively in beam-like regions perpendicular to these facets and interfere destructively elsewhere in space. In contrast to the isotropic example, the Green functions amplitude *does not* decay along the beams, which is similar to the Green function of a one-dimensional system. This implies that electrons emitted from point-like sources or scattered at point-like defects do not propagate in a spherical wave like in free space, but are in general *focused* in preferential directions and are detectable in much larger distances from the source than in the case of an isotropic band structure. In this case the Huygens wave assumes a much more complex shape.

¹the Fermi surface of the two-dimensional non-interacting s-band Hubbard-model has such a geometry at half filling, if only nearest-neighbor hopping processes are considered

I: Fermisurface / group velocity



II: Propagator

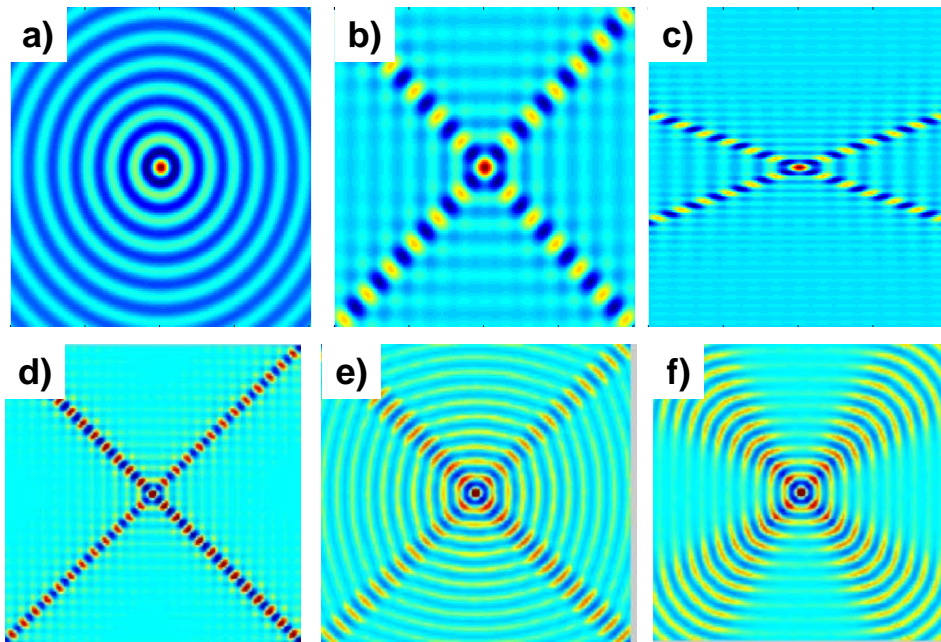


Figure 3.4: Illustration of the relationship between the geometry of the Fermi surface (I) (blue contours), the group velocities (red arrows) and the corresponding propagator (II) of a given system: constructive interference of the wave-functions occurs in the directions of the group velocities. Flat or weakly curved areas on the Fermi surface produce an accumulation of electron flux in certain directions.

If the inclination of the facets is modified (Fig. 3.4c) the directions of preferred propagation change in the same way but stay perpendicular to the flat areas. Here one can even observe that the wave-fronts are not necessarily perpendicular to the direction of propagation. Fig. 3.4d) shows that an enlargement of the Fermi surface does not change the directional characteristic but reduces the wavelength and the width of the beam-like propagation paths. The FS does not need to be such "square-edged" as the examples discussed above in order to produce *electron focusing* effects. In Fig. 3.4e) we show a model FS of rounded square geometry i.e. it is flat in certain regions and has a constant curvature elsewhere. This example illustrates that the corresponding Green function shows a non-decaying propagation within beams in the diagonal directions *and* a decreasing amplitude in the other directions. The Fermi surface of Figure 3.4f), which is slightly curved on all facets, still shows a strongly directional propagation. But as the "beams" diverge, the amplitude of G *does* decay with increasing distance.

These examples help to get a feeling for the relationship between the Green function and the geometry of the iso-energy surface. It was shown that if the FS is non-spherical, the propagator is anisotropic and has high intensities in the directions connected with the normal vectors on the FS. In the case of flat regions (equivalent to zero curvature) the normal vectors point in identical direction and the beam does not diverge. If a slight curvature is present on the FS, the distribution of normal vectors explains how the propagation paths diverge with increasing distance. The physical reason why normal vectors and surface curvatures seem to be important in the connection between $G(\mathbf{x} - \mathbf{x}', \varepsilon)$ and $\Omega(\varepsilon)$ will be extracted in the next section.

Stationary phase

We stated before that, since equation 3.5 is an ordinary superposition of plane waves, all effects and anisotropies we observed on the toy models can be attributed to constructive and destructive interference. The question is, how the positions \mathbf{x} , at which constructive interference occurs, depend on the chosen set of states $\Omega(\varepsilon) = \{\mathbf{k} | E(\mathbf{k}) = \varepsilon\}$ that are superposed. For this discussion we go back to the three-dimensional case.

The behavior can be generally understood with the well-known concept of stationary phase from wave mechanics. The wave functions of equation 3.5 possess a \mathbf{k} - and \mathbf{x} -dependent phase $\Phi = \mathbf{k}\mathbf{x}$. If this phase varies during the integration over the Fermi surface, rapid oscillation of the waves will result in cancellation. Maximum constructive interference occurs at those positions \mathbf{x} , where the phase is stationary,

i.e. $\nabla\Phi = \mathbf{0}$. If the iso-energy surface is parameterized using two coordinates φ, θ , this gives:

$$\frac{d\mathbf{k}}{d\theta}\mathbf{x} = \frac{d\mathbf{k}}{d\varphi}\mathbf{x} = 0 \implies \mathbf{x} \parallel \left[\frac{d\mathbf{k}}{d\varphi} \times \frac{d\mathbf{k}}{d\theta} \right] \quad (3.6)$$

Stationary phase and therefore maximum constructive interference occurs in directions normal to the surface. Alternatively, with $\Phi = \mathbf{k}\mathbf{x} - \omega t$, the stationary phase condition yields: $\mathbf{x}/t = \nabla_{\mathbf{k}}\omega(\mathbf{k}) = \mathbf{v}_{Gr}(\mathbf{k})$ i.e. the positions of constructive interference are determined by the group-velocity. This gives the same result, since the group velocities are always normal vectors on the iso-energy surfaces.

The model Fermi surfaces indicated that the amplitude does not decay along the focusing beams in the case of flat facets on the FS while the Green function does decay perpendicular to curved regions. Concerning this spatial decay of G , we perform a Taylor approximation of $\Omega(\varepsilon)$ near \mathbf{k}_0 :

$$\mathbf{k}(\varphi, \theta) = \mathbf{k}_0 + \varphi \frac{d\mathbf{k}}{d\varphi} + \theta \frac{d\mathbf{k}}{d\theta} + \frac{\varphi^2}{2} \frac{d^2\mathbf{k}}{d\varphi^2} + \frac{\theta^2}{2} \frac{d^2\mathbf{k}}{d\theta^2} \quad (3.7)$$

The orientation of the coordinates φ and θ was chosen appropriately so that $\frac{d^2\mathbf{k}}{d\varphi d\theta} = \mathbf{0}$. This means that the second derivatives in eq. 3.7 correspond to the *principal curvatures* $\mathbf{K}_j = \frac{d^2\mathbf{k}}{dj^2}|_{\mathbf{k}_0}$ ($j = \varphi, \theta$) at \mathbf{k}_0 . The iso-surface integration is then:

$$\iint e^{i\mathbf{k}(\varphi, \theta)\mathbf{x}} d\varphi d\theta = e^{i\mathbf{k}_0\mathbf{x}} \left[\int e^{i\varphi \left(\frac{d\mathbf{k}}{d\varphi}\mathbf{x} + \frac{\varphi}{2}\mathbf{K}_\varphi\mathbf{x} \right)} d\varphi \right] \left[\int e^{i\theta \left(\frac{d\mathbf{k}}{d\theta}\mathbf{x} + \frac{\theta}{2}\mathbf{K}_\theta\mathbf{x} \right)} d\theta \right] \quad (3.8)$$

Here the integrals in brackets can be regarded separately and recomposed later. If the curvature in the particular direction (φ or θ) is zero, evaluating the integral yields an envelope function that confines the beam laterally:

$$\int_{-\Delta/2}^{\Delta/2} e^{i\varphi \frac{d\mathbf{k}}{d\varphi}\mathbf{x}} d\varphi = \frac{2 \sin \Delta \frac{d\mathbf{k}}{d\varphi}\mathbf{x}}{\frac{d\mathbf{k}}{d\varphi}\mathbf{x}} = \Delta \text{sinc} \left(\Delta \frac{d\mathbf{k}}{d\varphi}\mathbf{x} \right) \quad (3.9)$$

The lateral width of this envelope function depends on the extension Δ of the flat area. When Δ is increased, the beam becomes narrower and higher in amplitude. This behavior was observed with the toy-model, where the beams of the larger Fermi surface in Fig. 3.4d) were thinner than those of the small square FS in Fig. 3.4a). The above expression does not include any terms that would cause a decay of the amplitude with increasing distance.

If a curvature around \mathbf{k}_0 is present in the particular direction (φ or θ), the evaluation of the integral in the directions of stationary phase yields:

$$\int_{-\infty}^{\infty} e^{i\frac{\varphi^2}{2}\mathbf{K}_\varphi\mathbf{x}} d\varphi = \left(-\frac{\pi}{2|\mathbf{K}_\varphi\mathbf{x}|} \right)^{1/2} e^{i\frac{\pi}{4}\text{sn}(\mathbf{K}_\varphi\mathbf{x})} \quad (3.10)$$

the last term gives $e^{-i\pi/4} / e^{+i\pi/4}$ phase shifts, if the surface is concave/convex near \mathbf{k}_0 . The important property is the spatial decay $\propto 1/\sqrt{|\mathbf{x}||\mathbf{K}_i|}$. If the principal curvature \mathbf{K}_i is reduced, the decay becomes weaker but stays $\propto |\mathbf{x}|^{-1/2}$ unless $\mathbf{K}_i = 0$.

Finally it is only important whether both, one or none of the brackets in eq. 3.8 give an $|\mathbf{x}|^{-1/2}$ - behavior. If *both* principal curvatures are non-zero ($K_i, K_j \neq 0$), which is the case for *spherical, ellipsoidal* or *hyperboloidal* areas, this results in a $|\mathbf{x}|^{-1}$ decay of G . A $|\mathbf{x}|^{-1/2}$ decay arises from *cylindrical* facets ($K_i = 0, K_j \neq 0$), where one principal curvature vanishes while the area is curved in the other direction. A non-decaying propagation will occur perpendicular to *flat* regions ($K_i, K_j = 0$). A similar derivation of indirect exchange interaction of systems with non-spherical Fermi surfaces was performed by Roth *et al.*[11]. The overall phase shift of both terms in brackets will be $+\pi/2$ (ellipsoidal maximum), $+\pi/4$ (cylindrical maximum), 0 (flat area or saddle point), $-\pi/4$ (cylindrical minimum), and $-\pi/2$ (ellipsoidal minimum).

If G is known, normal vectors, principle curvatures and phase-shifts are of minor relevance. But they are useful for a qualitative estimation of the shape of G from a "quick look" at the iso-energy surfaces $\Omega(\varepsilon)$ without performing the integration of equation 3.5.

3.2.3 Calculating G of the Host

After the discussion of simple Fermi surface geometries we will now analyze the realistic FS of the host material (copper) used for the experiments. As demonstrated in the last section, the propagator of a certain system is directly associated with the iso-energy-surfaces. Therefore it is of particular interest whether the band structure of copper shows anisotropies that could explain the experimental observations.

The Fermi surface of copper is well known from extensive experimental and theoretical studies. In contrast to the complex Fermi surfaces of other materials it looks rather normal, being "nearly" spherical with eight neck-like band gaps in the L-directions. It will now be shown that these small deviations from a spherical shape are responsible for the observed interference patterns. An overview of the Fermi surfaces of many materials can be found in [45]. Our analysis will be initially performed using this published data. Thereafter it will be necessary to *calculate* the iso-energy surfaces for various energies ε using an LCAO-technique.

Fermi surface from an Internet-Database

The most quick and easy way to analyze the propagation of electrons in copper is to use published Fermi surface data and to perform the identical analysis that was already done to our "toy model" examples. The URL www.phys.ufl.edu/fermisurface [45] contains Fermi surfaces for a large number of solid elements. They are available in both graphical data formats and as *vrml*-files (*Virtual Reality Modeling Language*). The latter one is a file format for interactive 3-dimensional vector graphics that allows the user to look at a 3D object from different perspectives. Within the file, the Fermi surface is stored as a 3D polygon, whose vertices are listed in plain text and can be easily extracted. This also allows to directly perform the identical analysis on any other material.

The *vrml*-files contain about 6700 k-points, which are irregularly distributed over the Fermi surface. In some regions, which are stronger curved (e.g. the "necks" of the Fermi surface), a high density of k-points is present while the file contains a smaller k-point density in other areas. Consequently the first step is to interpolate this data into a regular grid in spherical coordinates, which gives $k_F(\varphi, \theta)$. The set of coordinates $[\varphi, \theta, k_F(\varphi, \theta)]$ was transferred to cartesian coordinates $[k_x(\varphi, \theta), k_y(\varphi, \theta), k_z(\varphi, \theta)]$. From this the Jacobian determinant $J(\varphi, \theta)$ was calculated, describing the surface area of each grid "tile". Finally, by superposing all states lying on the Fermi surface, we obtained²:

$$-\frac{1}{\pi} \text{Im}G(\mathbf{x} - \mathbf{x}', \varepsilon_F) \propto \sum_{\varphi, \theta} J(\varphi, \theta) e^{i\mathbf{k}(\varphi, \theta)(\mathbf{x} - \mathbf{x}')} = \sum_{\varphi, \theta} J(\varphi, \theta) \cos(\mathbf{k}(\varphi, \theta)(\mathbf{x} - \mathbf{x}')) \quad (3.11)$$

In the last term the antisymmetric part of the exponential function was omitted because of time-inversion symmetry leading to $E(\mathbf{k}) = E(-\mathbf{k})$.

This quick and simple calculation already gives a general insight into the electron propagation in copper. The obtained Green function of copper is depicted in Figure 3.5 and demonstrates that significant effects of electron focusing are present in the host metal. Due to the crystal potential, the spherically symmetric propagator of a free electron constricts into eight slightly distorted hollow cones around the [111] directions. The propagation is strongly suppressed within a certain angle β around [111] that is much larger than the angle α , within which no states exist at the Fermi energy due to the pseudo-band gap in the L-directions. This directly explains, why the interference patterns observed on the (111) surface become larger in their diameter the deeper the defects were buried below the surface. An interesting

²equation 3.11 is approximate, since the summation lacks a factor $|\mathbf{v}_{Gr}(\varphi, \theta)|^{-1}$ that is not obtainable from the *vrml*-files

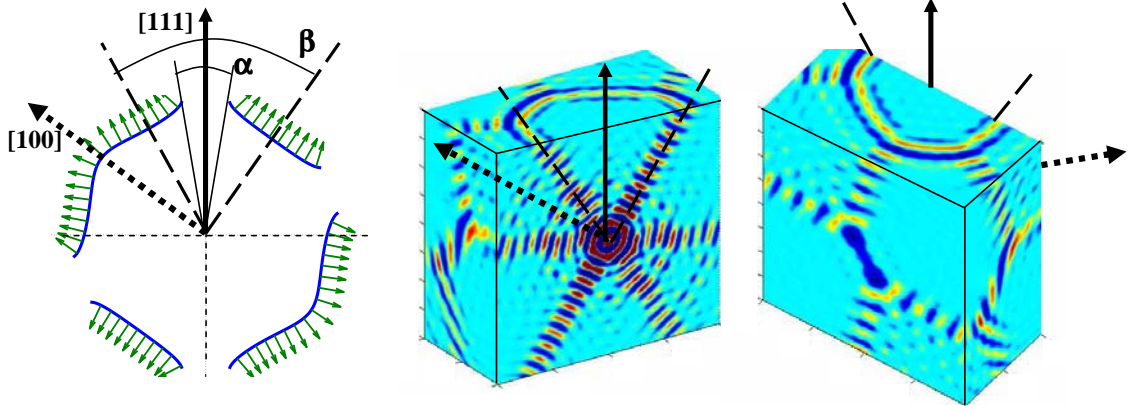


Figure 3.5: a) Fermi surface (cross section) of copper showing areas of reduced curvature b,c) corresponding propagator of copper: strong electron focusing onto hollow-cones around [111].

detail in Figure 3.5 is that the wall width of the focusing cone does not broaden with increasing distance. This in turn explains, why the width of the radial envelope was constant for the different observed STM patterns (≈ 1.5 oscillations).

Calculation of $E(k)$ by LCAO

In the following (especially in chapter 4) we will be interested in the energetic behavior of the propagation. Thus the iso-energy-surfaces for values different from ε_F are needed. Furthermore, as we will also need the real part of G_0 , the whole band structure $E(\mathbf{k})$ of copper has to be calculated. In this work we used a LCAO-technique (*linear combination of atomic orbitals*) for this purpose. The data available in the Fermi surface database had been calculated using identical method and parameters [46] as we are using here.

To calculate the band structure of copper, a set of 9 basis functions (1 s-state, 3 p-states and 5 d-states) was used. The required \mathbf{k} -dependent overlap $S_{ij}(\mathbf{k})$ and Hamiltonian matrices $H_{ij}(\mathbf{k})$ were calculated from a set of LCAO parameters. These were taken from literature [46]. The authors obtained the parameters by fitting the band structures to the results of "first-principle" calculations. By this they obtain RMS deviation from the *ab-initio* results of 7meV and a maximum error of 15meV. Consequently it is possible to obtain realistic data of the host-metal's band structure by easy calculations. A brief introduction into the LCAO-technique as well as the expressions for the matrix elements ($S_{ij}(\mathbf{k})$, $H_{ij}(\mathbf{k})$) and the parameters we used can be found in Appendix A.

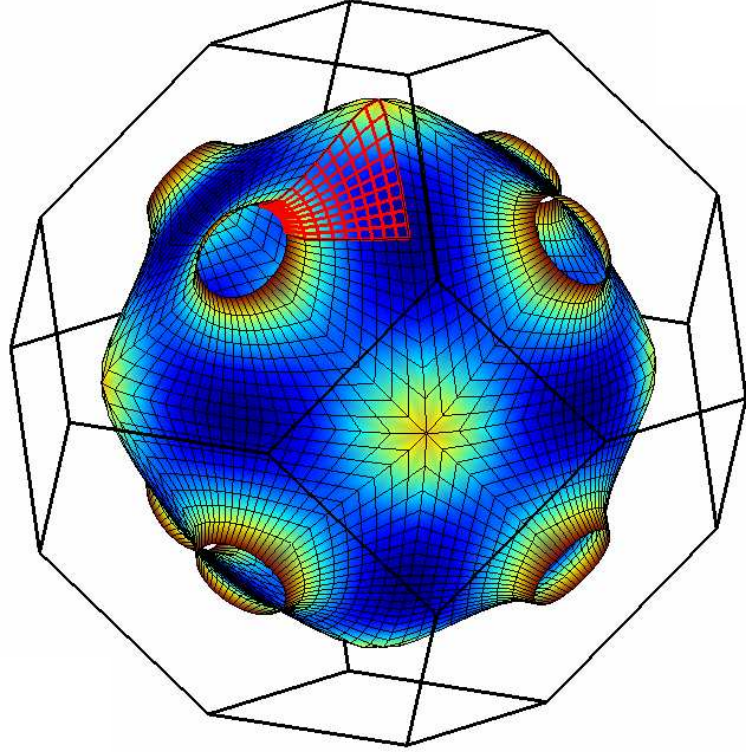


Figure 3.6: *Fermi surface calculated using the LCAO technique. A specialized curvilinear coordinate system was used to seamlessly cover the Fermi surface while reflecting the symmetries of the fcc-point-group. A 10x10 Grid within the irreducible part of the first Brillouin zone is plotted in red.*

Since the fcc-Brillouin zone is invariant under various symmetry transformations, computational effort can be reduced by restricting the calculations to the irreducible part of the first Brillouin zone (iFBZ). The iFBZ is 1/48 of the full Brillouin zone. In order to seamlessly cover the Fermi surface, a special angular grid was used. This can be seen in Figure 3.6 and is described in Appendix A. The computational time for a such a 10x10 grid is 15 seconds and gives already acceptable results in the subsequent calculation of G . For most of the calculations we used a 20x20 grid which corresponds to a total number of 19200 k-points.

At every grid point (φ, θ) , Fermi wavevector $\mathbf{k}(\varphi, \theta)$, the Jacobi determinant $J(\varphi, \theta)$ and the group-velocity $\mathbf{v}_{Gr}(\varphi, \theta)$ (which was not available in the *vrml*-files) were determined. From this, the imaginary part of the propagator was calculated:

$$\text{Im}G(\mathbf{x} - \mathbf{x}', \varepsilon) = -i\pi \sum_{\mathbf{k} \in \Omega(\varepsilon)} \frac{J(\mathbf{k})}{|v_{Gr}(\mathbf{k})|} e^{i\mathbf{k}(\mathbf{x} - \mathbf{x}')} \quad (3.12)$$

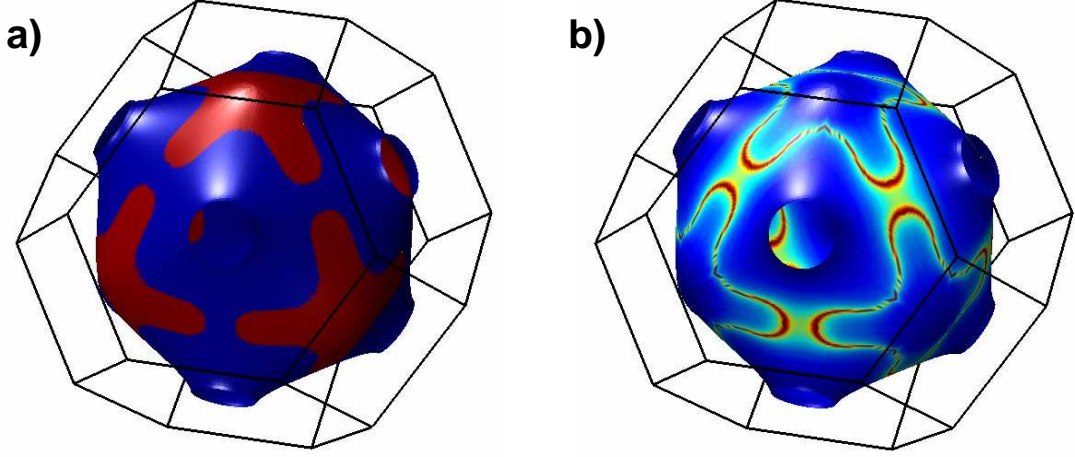


Figure 3.7: a) the sign of the Gaussian curvature and b) the inverse mass tensor are represented on the Fermi surface with colors. a) red regions are local maxima while blue regions correspond to saddle points b) red values correspond to low curvatures and hence to high intensities in the resulting Green function. The calculation was performed using the LCAO technique.

The real part of G was either calculated using the Kramers-Kronig relation [47, 48] from a set of $\text{Im}G(\varepsilon)$ at different energies ε or approximately from the iso-energy surface $\Omega(\varepsilon)$. For sake of readability this is described in Appendix B.

As stated before the propagator can be obtained directly from the band structure $E(\mathbf{k})$ and without the prior calculation of group-velocities, effective mass tensors, curvatures etc. However, these concepts are useful in understanding why the propagator has high intensities in some directions and electron flux is suppressed in other directions. Before coming back to the description of subsurface impurities we want to analyze some topological properties of the copper FS. Figure 3.7a) shows the sign of the Gaussian curvature on different parts of the Fermi surface. The Gaussian curvature is the product of both principal curvatures, i.e. it is positive in the case of minima and maxima and negative in the case of saddle-points. We can see that the Fermi surface is convex in cross-like regions centered around $[100]$, while the blue-regions have a negative Gaussian curvature. Obviously, along the connection line between both regions the Gaussian curvature has to be zero. This means that at least one of both principal curvatures has to be zero at these positions which in turn produces an electron focusing effect. Figure 3.7b) shows the inverse effective mass tensor of the quasi-particles at the Fermi energy. This concept is also commonly used in the theory of interlayer-exchange coupling [3]. It is a direct measure of the

flatness of the particular area and describes the strength of the electron flux in the particular direction. Of course this concept breaks down, if one principal curvature is zero. From the inverse mass tensor we can see that high intensities occur at the junctions between the red and blue areas of Fig. 3.7a).

From analyzing the geometry of the host metal's Fermi surface and from the deduced shape of the conduction electron propagator we can already understand the experimental observations. The bulk electrons that are scattered at the subsurface atoms are focused in preferential directions. Thus the standing wave pattern has high intensities in these directions. Up to now we did not calculate any local density of states and regarded only the "Huygens wave" of electrons in copper. We now require a physical concept that properly describes the perturbation of the conduction electrons by the impurity.

3.3 Interaction: single impurity scattering

So far we regarded G , a property of the infinite, unperturbed host metal describing the response of such a system to a mono-energetic, point like excitation. The next step is to introduce perturbations in this system and to analyze how these affect the local density of states.

3.3.1 The t-matrix

In general, the effect of any perturbations (surface, interfaces, impurities) can be subsumed in a specific t-Matrix $t(\mathbf{x}, \mathbf{x}', \varepsilon)$ which is due the potential change $\Delta V = V - V_{host}$ between the perturbed system and ideal host. We will now term the Green function of the ideal host G_0 . The propagator G of the perturbed system can then be obtained from the unperturbed propagator G_0 and the t-matrix using the Dyson equation [49]:

$$G(\mathbf{x}, \mathbf{x}', \varepsilon) = G_0(\mathbf{x}, \mathbf{x}', \varepsilon) + \iint d^3x'' d^3x''' G_0(\mathbf{x}, \mathbf{x}''', \varepsilon) t(\mathbf{x}''', \mathbf{x}'', \varepsilon) G_0(\mathbf{x}'', \mathbf{x}', \varepsilon) \quad (3.13)$$

The most simple perturbation is a single point scatterer. In this case the t-Matrix is reduced to a complex number $t_{imp}(\varepsilon) = t(\mathbf{x}_i, \mathbf{x}_i, \varepsilon)$ at the position of the impurity \mathbf{x}_i . The Green function of the system including the impurity is then modified by an additional term, describing the propagation from \mathbf{x}' to the impurity at \mathbf{x}_i , the scattering described by $t_{imp}(\varepsilon)$ and the propagation to \mathbf{x}

$$G(\mathbf{x}, \mathbf{x}', \varepsilon) = G_0(\mathbf{x}, \mathbf{x}', \varepsilon) + G_0(\mathbf{x}, \mathbf{x}_i, \varepsilon) t_{imp}(\varepsilon) G_0(\mathbf{x}_i, \mathbf{x}', \varepsilon) \quad (3.14)$$

The complex number $t_{imp}(\varepsilon)$ describes the scattering amplitude and -phase shift of the electrons due to the interaction with the impurity.

3.3.2 LDOS in the vicinity of a single impurity

For the STM-experiment we are interested in the local density of states in the vicinity of the impurity. Thus we need the diagonal elements ($\mathbf{x} = \mathbf{x}'$) of the perturbed propagator G , as they correspond to the stationary part of the spectral electron density :

$$\varrho(\mathbf{x}, \varepsilon) = -\frac{1}{\pi} \text{Im} G(\mathbf{x}, \mathbf{x}, \varepsilon) = \varrho_0(\varepsilon) + \Delta\varrho(\mathbf{x}, \varepsilon) \quad (3.15)$$

Here the unperturbed local density of states ϱ_0 is independent of the position \mathbf{x} as we neglected the lattice-periodic part $u_{\mathbf{k}}(\mathbf{x})$ in the Green function. This first term just produces the "grey background" in the STM-images. Due to time-inversion symmetry, the values of G_0 for the propagation to and forth the impurity are identical. The observed oscillations in the LDOS are contained in the last term of equation 3.15, which is:

$$\Delta\varrho(\mathbf{x}, \varepsilon) = -\frac{1}{\pi} \text{Im} [t_{imp}(\varepsilon) G_0(\mathbf{x}, \mathbf{x}_i, \varepsilon)^2] \quad (3.16)$$

Consequently, with the assumption of a point-scatterer, the three dimensional LDOS-oscillations in the vicinity of the impurity can be directly obtained, once the propagator is calculated. The envelope of these oscillations is solely determined by G_0 . The quantity describing the position of LDOS maxima and -minima within this envelope is the phase of the unknown complex number $t_{imp}(\varepsilon)$.

If the impact of the surface (reflections) on the propagation is neglected - we will abandon this assumption later - the LDOS at the surface corresponds to two-dimensional cross-sections normal to certain directions and in certain distances through the three-dimensional LDOS-modulation described by equation 3.16. An example of (111) sections in distances of 6,8,10 and 12 ML from the point scatterer can be seen in figure 3.8 ³.

The results for [100] and [111] planes in certain distances from the impurity are shown in Fig. 3.9. They show some qualitative similarity to the measured STM-images, i.e. they show features increasing in size with increasing distance from the impurity that poses a significant anisotropy. The latter is also directly connected to the host metals band structure (3-fold symmetry for (111) and 4-fold symmetry for

³In reality G_0 was calculated only on these planes instead of computing three-dimensional data and discarding most of it afterwards

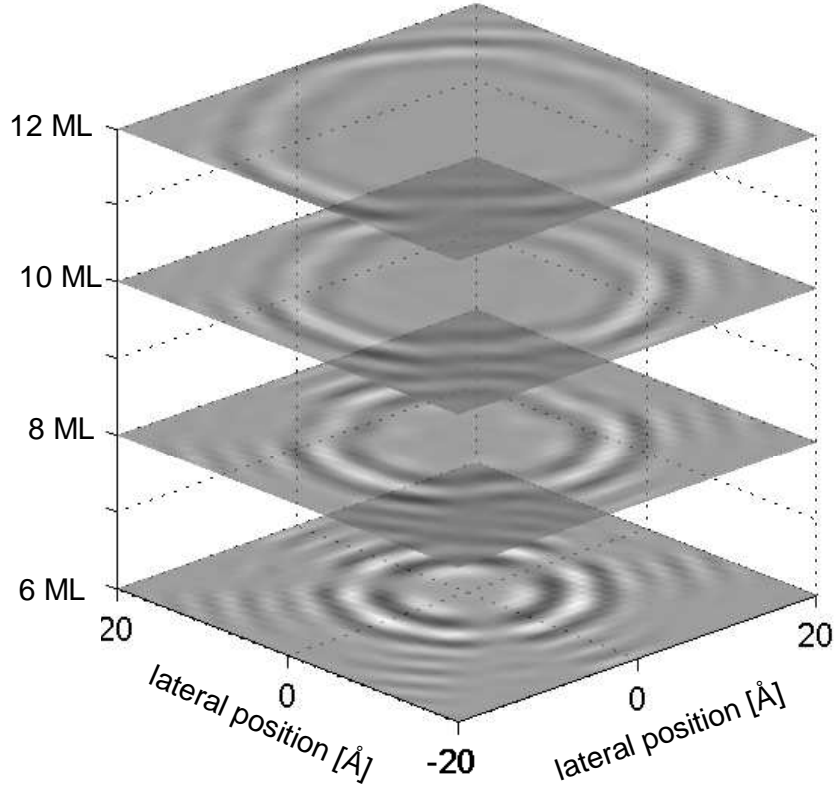


Figure 3.8: *LDOS oscillations on planes in distances of 6,8,10 and 12 ML to the impurity and perpendicular to the $[111]$ direction*

(100) planes) and explains, why no LDOS modulation is present within a certain angle above an impurity below the (111) surface.

Although the result show some similarity to the experiments, there are some significant differences. A quantitative comparison reveals that the wavelength of the calculated oscillations is shorter than in the experiments. Additionally, the calculations appear "wrinkled" and show beams extending in radial directions. These beams are along the intersections of the "surface" and the cones which are oriented in a certain angle relative to the surface. In the case of the (111)-surface, these are the focusing cones around $[11\bar{1}]$, $[1\bar{1}1]$ and $[\bar{1}11]$ which produce open curves at the surface. The identical mechanism is responsible for the 4 beams on the (100)-planes that arise from intersecting $[111]$, $[11\bar{1}]$, $[1\bar{1}1]$ and $[\bar{1}\bar{1}\bar{1}]$ oriented cones. This is sketched in Figure 3.10.

In fact we do not observe any of these conic sections in the experiments and thus the presented results are unsatisfactory. Therefore we have to remember *what* the STM

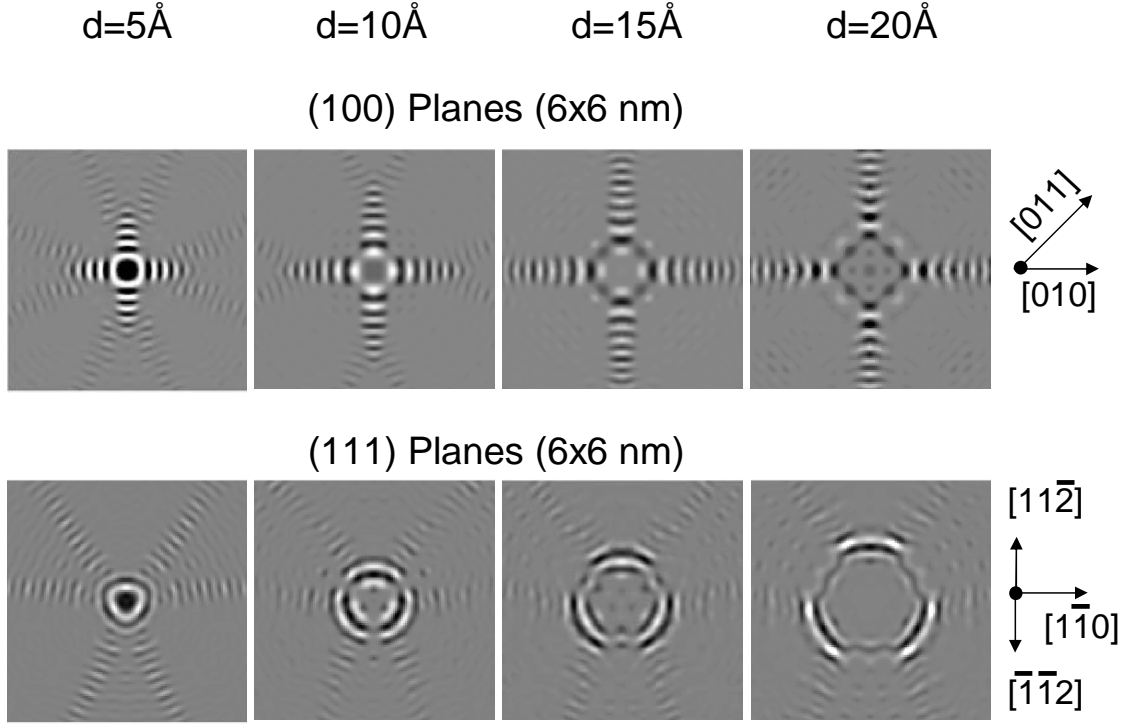


Figure 3.9: *calculated LDOS on planes in different distances (5\AA , 10\AA , 15\AA and 20\AA) from the impurity and normal to certain directions ((100) and (111)).*

is sensitive to and we have to consider the way, how the model needs to be modified in order to reproduce the experimental observations. Obviously an important physical effect has not been considered so far. Most probably this is the role of the surface, which was treated in a very unrealistic way so far.

3.4 Detection

In the previous section it was described, how the LDOS is modulated in the vicinity of a single subsurface point scatterer. It was shown that due to the *electron-focusing* effect, the LDOS is influenced only in narrowly confined directions from the impurity. Therefore the standing wave pattern is mainly restricted to eight slightly distorted hollow cones around the $\{111\}$ -directions. Intersecting $[111]$ planes therefore show LDOS modulations in a ring-like area while $[100]$ planes show square-like patterns. In this section we will include one final physical effect in order to correctly describe the experimental data. This is the role of the surface and the tunnelling-junction.

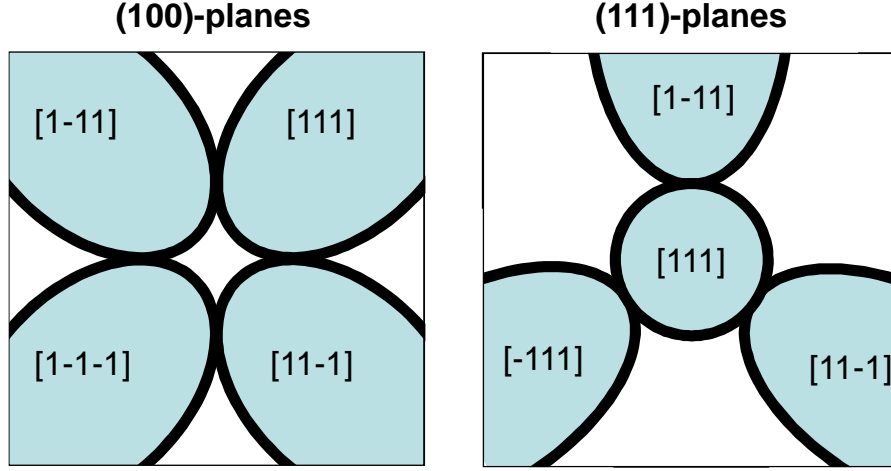


Figure 3.10: Sketch to illustrate the sections of the focusing cones that are oriented in certain angles relative to the surface.

As was described in Chapter 2 (STM Theory of Tersoff and Hamann) the sample LDOS inside the *vacuum* at a certain distance h - corresponding to a position well within the STM-tip - is *mathematically* adequate to describe the measured tunnelling current. This distance h is basically the sum of the tip-sample separation h_0 and the tip's curvature radius R . Both may vary under different experimental conditions, although the particular values are usually not known with absolute precision. h_0 can be modified by changing the tunnelling resistance V_T/I_T while R can be changed by modifying the tip's morphology using *in-situ* tip preparations, i.e. voltage pulses or gentle tip-sample contacts. Before investigating this experimental behavior, we want to analyze how the *vacuum* LDOS in certain distances h from the surface is modified by the presence of the impurity. Our model, which presently contains only the (anisotropic) propagation within the bulk and the scattering at the impurity has to be extended by a third physical process: the reflection of the electrons by the surface and their exponential decay into the vacuum.

3.4.1 Vacuum LDOS at different distances - a first approach

The tunnelling current has contributions of multiple states, which are decaying differently into the vacuum. If we assume full translational invariance parallel to the surface, the parallel component of wave vector k_{\parallel} is conserved. Inside the vacuum the electrons obey the Schrodinger equation [50] of a free-electron:

$$\frac{\hbar^2}{2m}(k_{\parallel}^2 - \kappa^2) = \Delta E - \Phi \quad (3.17)$$

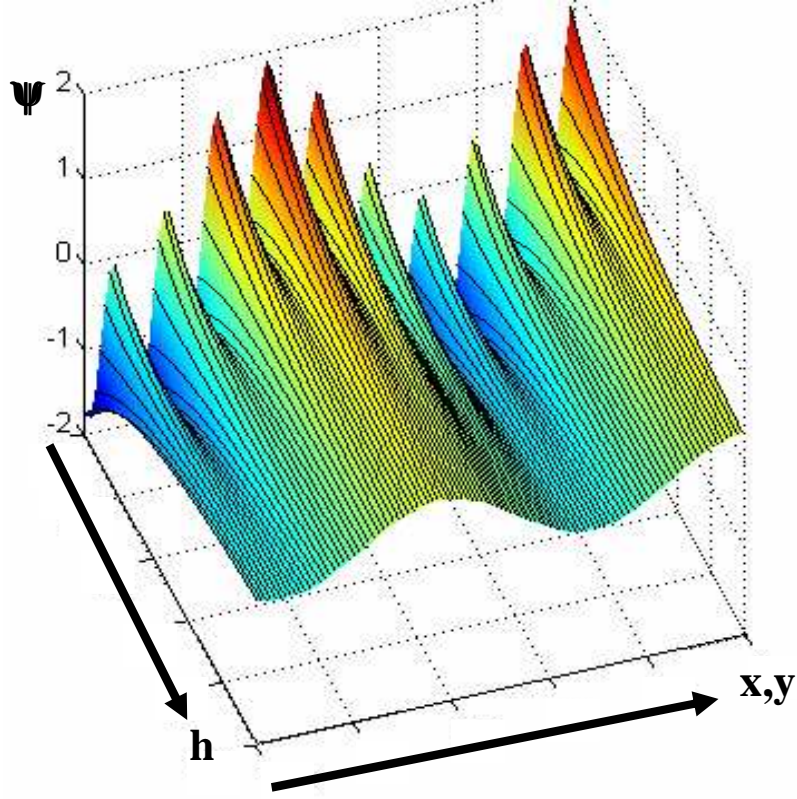


Figure 3.11: *Sketch to illustrate the effect of an k_{\parallel} -dependant exponential decay on the vacuum LDOS. The short wavelength contribution gets suppressed and will not be detected for higher tip-sample distances h .*

Here Φ is the work function of the material and $\Delta E = E - \mu$ the electron energy with respect to the chemical potential. From this a k_{\parallel} -dependant decay constant κ can be derived:

$$\kappa(k_{\parallel}) = \sqrt{\frac{2m}{\hbar^2}(\Phi - \Delta E) + k_{\parallel}^2} \quad (3.18)$$

This equation is the most important reason, why the LDOS oscillations calculated in the previous section had only a fair agreement with the experimental observations. The above expression shows that states with high k_{\parallel} -values have a higher κ and therefore decay faster into the vacuum. Consequently the STM is more sensitive to states near the center of the surface Brillouin-zone, while short-wavelength contributions to the LDOS oscillations will be suppressed. This is sketched in Fig. 3.11 showing that at higher distances h , the wave function is dominated by the long wavelength contributions.

In the vacuum, the wave-function of state $|k\rangle$ is then:

$$\Psi(\mathbf{x}_{\parallel}, h) \sim \exp(i\mathbf{k}_{\parallel}\mathbf{x}_{\parallel}) \cdot \exp\left(-h\sqrt{\mathbf{k}_{\parallel}^2 + \kappa_0^2}\right) \quad (3.19)$$

where we defined $\kappa_0 \equiv \kappa(k_{\parallel} = 0) = \sqrt{2m(\Delta E - \Phi)}/\hbar$. In order to get an idea how this effect influences the observed patterns we perform a Taylor approximation of eq. 3.19 up to third order:

$$\sqrt{k_{\parallel}^2 + \kappa_0^2} \approx \kappa_0 + \frac{k_{\parallel}^2}{2\kappa_0} \quad (3.20)$$

This approximation is valid for $k_{\parallel} < \kappa_0$. For the case of copper this is a good treatment of states having $k_{\parallel} < 1.1\text{\AA}^{-1}$ while states having higher k_{\parallel} values are over-suppressed (the approximate radii of the Cu-Fermi surface are $\approx 1.3\text{\AA}^{-1}$ in [110] and $\approx 1.45\text{\AA}^{-1}$ in [100] direction). Inserting 3.20 in 3.19 gives a handy expression:

$$\exp(-\kappa h) \approx \exp(-\kappa_0 h) \cdot \exp\left(-\frac{k_{\parallel}^2 h}{2\kappa_0}\right) \quad (3.21)$$

This is, apart from a general attenuation ($\exp(-\kappa_0 h)$) of the wave function's amplitude, a Gaussian with a standard deviation of $\sigma_k = \kappa_0/h$. This implies that one can transform the wave functions from a smaller distance h_1 to greater distances h_2 by a convolution (symbol $*$) with a Gaussian of standard deviation $\sigma_x = h/\kappa_0$:

$$\Psi(\mathbf{x}_{\parallel}, h_2) = \exp(-\kappa_0(h_2 - h_1)) \cdot \Psi(\mathbf{x}_{\parallel}, h_1) * \exp\left(-\frac{\mathbf{x}_{\parallel}^2}{2\sigma_x}\right) \quad (3.22)$$

This is very helpful as the effect of the tip-sample distance h can be described by a simple Gauss filtering. If we increase h either by choosing tunnelling conditions, where the tip is at a larger distance from the surface or by using a blunter tip, the wave functions probed by the tip will be increasingly smeared out. If the approximation 3.21 is not valid, the convolution has to be performed using a function different from a Gaussian (the Fourier transform of the last term in eq. 3.19), but the whole effect can still be understood as a kind of smoothing filter. This convolution can also be applied to any superposition of wave functions as well as to the Green functions.

For a moment we assume that the intersecting planes of the 3-dimensional Friedel oscillation calculated in the previous section *are* the surface LDOS at $h = 0$. This approach neglects reflections of the electrons induced by surface and will be abandoned later. In this case we can obtain the vacuum LDOS at distances $h > 0$ by the procedure described above: the Green function G_0 describing the propagation of electrons from the position of the impurity to the "surface" is convoluted with a Gaussian of width $\sigma_x(h)$. Thereafter the obtained propagator $G_0(\mathbf{x}, \mathbf{x}_1, h, \varepsilon)$ is

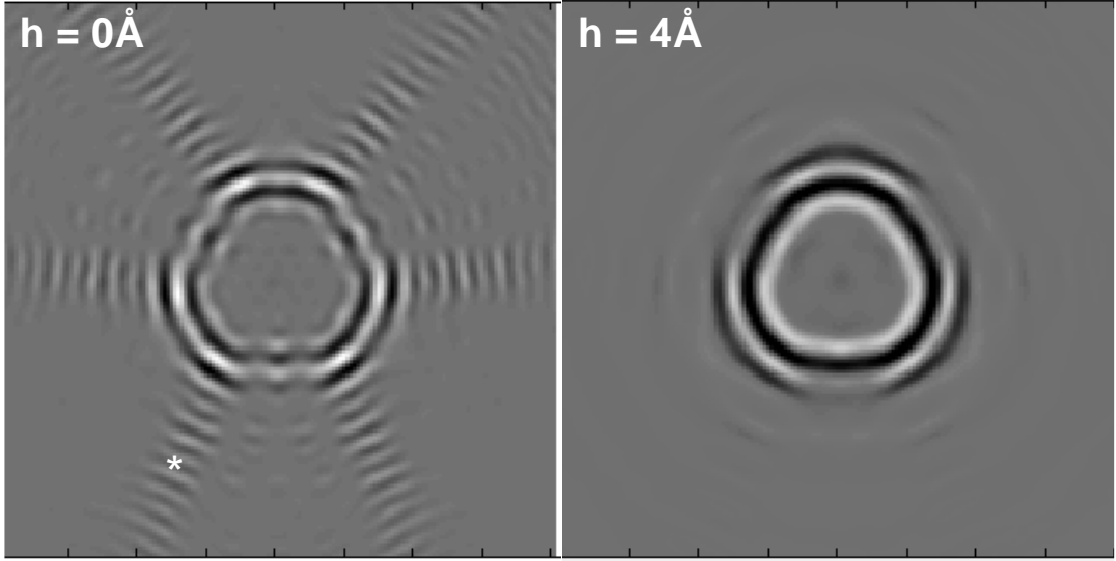


Figure 3.12: *Impact of different tip-sample distances h on the calculated LDOS: enlarging h suppresses short-wavelength contributions.*

inserted in equation 3.16. The result is depicted in Figure 3.12 for $h = 0\text{\AA}$ and $h = 4\text{\AA}$. This brings the results of the calculations more closely to the experimental data: as short wavelength states are suppressed, increasing h increases the observed wavelength. The six beams (*) visible in the LDOS of the (111) surface - they correspond to the intersections of the focusing cones around $[\bar{1}11]$, $[1\bar{1}1]$ and $[11\bar{1}]$ - have disappeared. Finally, the whole pattern, which appeared rather wrinkled at $h = 0$ becomes more smoothed for higher tip-sample distances.

Obviously the propagation of the electrons in the vacuum is also an important physical process in our experimental system. The convolution technique gives an illustrative insight into the impact of these effect on the experimental observations. As a last refinement of this model we will now include the effect of surface reflections in a more detailed approach. After that we will go back to the experimental data and perform a detailed comparison with the results of the calculations.

3.4.2 Implementing a semi-infinite crystal geometry

Previously, the behavior within the bulk and the vacuum have been treated separately. The unperturbed propagator of the host material showed strong anisotropies that explained the directional dependence of the LDOS modulations while the k_{\parallel} -dependent decay within the vacuum could be approximated by the effect of a simple

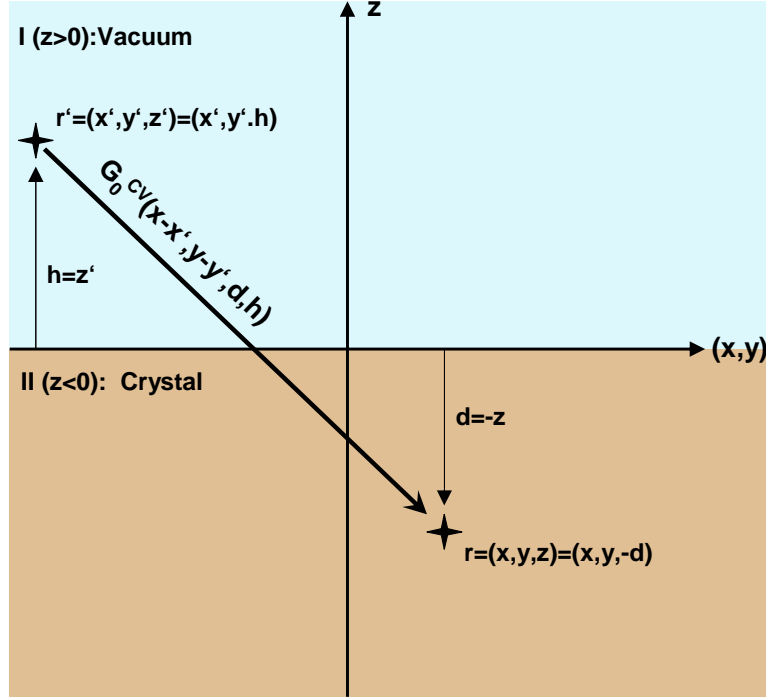


Figure 3.13: *Coordinate system used for the semi-infinite crystal geometry. The propagator G^{CV} describes the propagation from a position \mathbf{r}' within the vacuum to a position \mathbf{r} inside the crystal.*

Gauss filter. Up to now, we did not match these two processes together so that the continuity of wave function's derivative at the surface was not given. The impact of the surface on the bulk propagation (reflections) was completely ignored. These effects should not be neglected, especially since they can easily be implemented without increasing the computational effort.

We now choose the z -axis perpendicular to the surface and define two adjacent subspaces "vacuum" (V) ($z > 0$) and "crystal" (C) ($z \leq 0$) in which the wave functions are denoted $\Psi_{\mathbf{k}}^{(V)}$ and $\Psi_{\mathbf{k}}^{(C)}$, respectively. In order to clarify whether a position is within C or V, we will use the variables d ("depth", $d = -z | z \leq 0$) and h ("height"; $h = z | z > 0$) for the two subspaces. The chosen geometry is depicted in Fig. 3.13.

We again assume a full translational invariance parallel to the surface so that \mathbf{k}_{\parallel} is conserved. The perpendicular wave vector component $k_{\perp}^{(i)}$ of an incident electron is now reflected into $k_{\perp}^{(r)}$. The connection between $k_{\perp}^{(i)}$ and $k_{\perp}^{(r)}$ depends on the symmetry of the band structure with respect to the particular surface direction. In

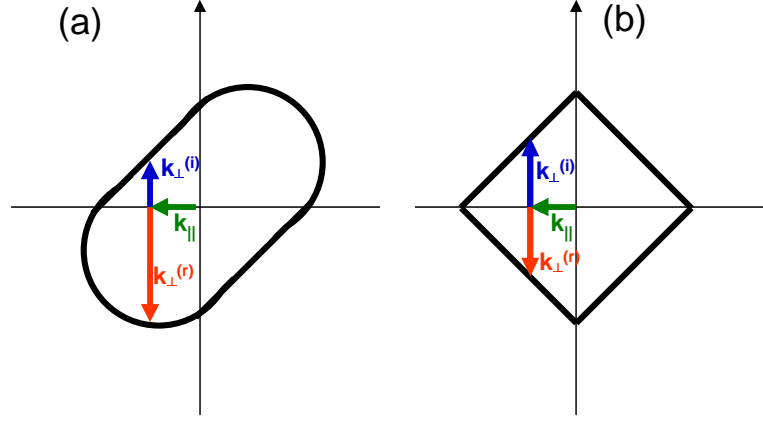


Figure 3.14: *The role of the surface: an incident electron $(\mathbf{k}_{\parallel}, k_{\perp}^{(i)})$ is reflected by the surface into state $(\mathbf{k}_{\parallel}, k_{\perp}^{(r)})$, which depends on the symmetry of $\Omega(\varepsilon)$ with respect to the particular surface direction.*

Figure 3.14a) this is sketched for a Fermi surface, which does not have reflection symmetry in the surface direction. If the surface constitutes a mirror plane of the crystal, which is the case for (100) and (110) surfaces, this results in $k_{\perp}^{(r)} = -k_{\perp}^{(i)}$ (Figure 3.14b).

A certain state $|\mathbf{k}\rangle$ is described inside the crystal by the wave function

$$\Psi_k^{(C)}(\mathbf{x}_{\parallel}, d) = n(\mathbf{k})e^{i\mathbf{k}_{\parallel}\mathbf{x}_{\parallel}} \left[e^{-ik_{\perp}^{(i)}d} + a(\mathbf{k})e^{-ik_{\perp}^{(r)}d} \right] \quad (3.23)$$

and within the vacuum by the wave-function

$$\Psi_k^{(V)}(\mathbf{x}_{\parallel}, h) = n(\mathbf{k})b(\mathbf{k})e^{i\mathbf{k}_{\parallel}\mathbf{x}_{\parallel} - \kappa(\mathbf{k})h} \quad (3.24)$$

with $\mathbf{x}_{\parallel} = (x, y)$ and $\mathbf{k}_{\parallel} = (k_x, k_y)$. $n(\mathbf{k}) = (V(1 + |a(\mathbf{k})|^2))^{-1/2}$ is a normalization constant with V being the crystal volume. The coefficients $a(\mathbf{k})$ (reflection) and $b(\mathbf{k})$ (transmission) have to be chosen to meet the boundary conditions $\nabla\Psi^{(C)} = \nabla\Psi^{(V)}$ and $\Psi^{(C)} = \Psi^{(V)}$ at the surface $h = d = 0$. This results in:

$$a(\mathbf{k}) = -\frac{ik_{\perp}^{(i)} + \kappa(k_{\parallel})}{ik_{\perp}^{(r)} + \kappa(k_{\parallel})} \quad b(\mathbf{k}) = \frac{i(k_{\perp}^{(r)} - k_{\perp}^{(i)})}{ik_{\perp} + \kappa(k_{\parallel})} \quad (3.25)$$

with $\kappa(\mathbf{k}_{\parallel})$ being the decay constant that was defined in equation 3.18.

From the last equation it is evident that high k_{\parallel} -components are suppressed in vacuum LDOS not only due to their faster decay but also because of their lower transmissivity $b(\mathbf{k})$ at the surface.

By knowing the wave functions in both subspaces we can now define four possible Green functions that depend on whether the electron is created or annihilated in crystal and vacuum, respectively. This is again done using the spectral representation:

$$G^{VV}(\mathbf{x}, \mathbf{x}_i, \varepsilon) = \int_{\mathbf{k}} d^3k G(\mathbf{k}, \varepsilon) \Psi_{\mathbf{k}}^{(V)}(\mathbf{x}) \Psi_{\mathbf{k}}^{*(V)}(\mathbf{x}_i) \quad (3.26)$$

$$G^{VC}(\mathbf{x}, \mathbf{x}_i, \varepsilon) = \int_{\mathbf{k}} d^3k G(\mathbf{k}, \varepsilon) \Psi_{\mathbf{k}}^{(V)}(\mathbf{x}) \Psi_{\mathbf{k}}^{*(C)}(\mathbf{x}_i) \quad (3.27)$$

$$G^{CV}(\mathbf{x}, \mathbf{x}_i, \varepsilon) = \int_{\mathbf{k}} d^3k G(\mathbf{k}, \varepsilon) \Psi_{\mathbf{k}}^{(C)}(\mathbf{x}) \Psi_{\mathbf{k}}^{*(V)}(\mathbf{x}_i) \quad (3.28)$$

$$G^{CC}(\mathbf{x}, \mathbf{x}_i, \varepsilon) = \int_{\mathbf{k}} d^3k G(\mathbf{k}, \varepsilon) \Psi_{\mathbf{k}}^{(C)}(\mathbf{x}) \Psi_{\mathbf{k}}^{*(C)}(\mathbf{x}_i) \quad (3.29)$$

Here we used $G(\mathbf{k}, \varepsilon) = (\varepsilon - E(\mathbf{k}) + i0^+)^{-1}$. Computational effort can be reduced by calculating only those quantities that are really needed for the current topic. The impurity atom will *always* be positioned within the *crystal* (C) and our primary interest is *restricted* to the LDOS $\varrho(\mathbf{x}_{\parallel}, h)$ within the *vacuum* (V). Without the impurity the vacuum LDOS would be

$$\varrho_0(h, \varepsilon) = -\frac{1}{\pi} \text{Im} G^{VV}(\mathbf{x}, \mathbf{x}, \varepsilon) = \int_{\mathbf{k}} d^3k \delta(\varepsilon - E(\mathbf{k})) |n(\mathbf{k})b(\mathbf{k})|^2 e^{-2\kappa(\mathbf{k})h} \quad (3.30)$$

The insertion of the impurity requires the consideration of additional propagation paths to the impurity (G^{CV}) and back (G^{VC}). Due to time-inversion symmetry these two quantities are equal and need to be calculated only once. With $\Delta\mathbf{x}_{\parallel} = \mathbf{x}_{\parallel} - \mathbf{x}'_{\parallel}$ we obtain the expression:

$$G^{VC}(\Delta\mathbf{x}_{\parallel}, h, d, \varepsilon) = \int_{\mathbf{k}} d^3k G(\mathbf{k}, \varepsilon) |n(\mathbf{k})|^2 b(\mathbf{k}) e^{i(\mathbf{k}_{\parallel}\Delta\mathbf{x}_{\parallel} + k_{\perp}d) - \kappa(\mathbf{k}_{\parallel})h} \quad (3.31)$$

In the context of single impurity scattering, the propagator G^{CC} is not needed. The vacuum LDOS in a distance h from the surface, which is modified by a single point defect having the scattering behavior $t_{imp}(\varepsilon)$ and being placed in a depth d below the surface, is described by:

$$\varrho(\mathbf{x}_{\parallel}, h, \varepsilon) = \varrho_0(h, \varepsilon) - \frac{1}{\pi} \text{Im} \left[(G^{VC}(\mathbf{x}_{\parallel}, h, d, \varepsilon))^2 t_{imp}(\varepsilon) \right] \quad (3.32)$$

This is the final expression that will be used throughout the following.

After this last refinement we included all prominent physical effects: i) the (anisotropic) propagation of the electrons in the host metal, ii) the scattering at a (single) impurity and iii) the role of the surface resulting in reflections of the electrons and

in a (\mathbf{k}_{\parallel} -dependent) decay into the vacuum. All these effects have been considered in the simplest possible way. Concerning the propagation the lattice-periodic part of the wave-functions has been neglected. The impurity has been simplified to a point-scatterer and the surface was assumed to be step-like with full translational invariance parallel to the surface (instead of lattice-periodicity).

It is now time to go back to the experimental data and to analyze if the effects we saw in the model can be observed in "reality". We start with the last process added to the model and analyze how different tip-qualities and tunnelling resistances affect the observed STM-images and if calculations with different values of h can reproduce the effect.

3.4.3 Impact of the tip quality

It is a matter of common experience to all STM-users that different tip conditions result in different acuities of the obtained images. These are usually attributed to "dull" or "sharp" tips and tip preparations by applying voltage pulses or gentle tip-sample contacts can significantly affect the image quality. As described in section 2.2.2, when assuming an s-like tip, the effects of different tip curvature radii R can be included by regarding the sample LDOS "in the middle" of the tip. This is quite reasonable since in the case of a "dull" tip having a big curvature radius, the LDOS has to be regarded at larger distances than in the case of tips having a small radius of curvature. Since we know that the wave functions at greater distances can be approximately obtained by Gauss filtering the wave function at smaller distances, it is obvious that the STM images obtained with "dull" tips are more smeared out.

In the experiments performed within the context of this work, these effects played a prominent role. Identical defects measured with the same tunnelling parameters (V_T , I_T) but with different tip qualities showed unressembling topographies. On the left side of Figure 3.15 experimental data with atomic resolution can be seen. The resolved lattice allows an attribution of the individual defect pattern to even and odd impurity depths. On the right side data obtained with a mediocre tip is shown. The two identical defects in Fig. 3.15a) - they will later be attributed to third layer Co-atoms - show a central elevation. From this, it could be presumed that the observed data in Fig. 3.15f), obtained with a dull tip, also shows 3rd layer impurities because the patterns are of comparable size and also shows a central elevation. For a closer analysis we convoluted the topographies obtained with the sharp tip by a Gauss function. This is depicted in the middle column of Figure 3.15. Although in principle only the wave-functions at different values of h can be transformed by a Gaussian convolution and this procedure is not valid for the transformation of

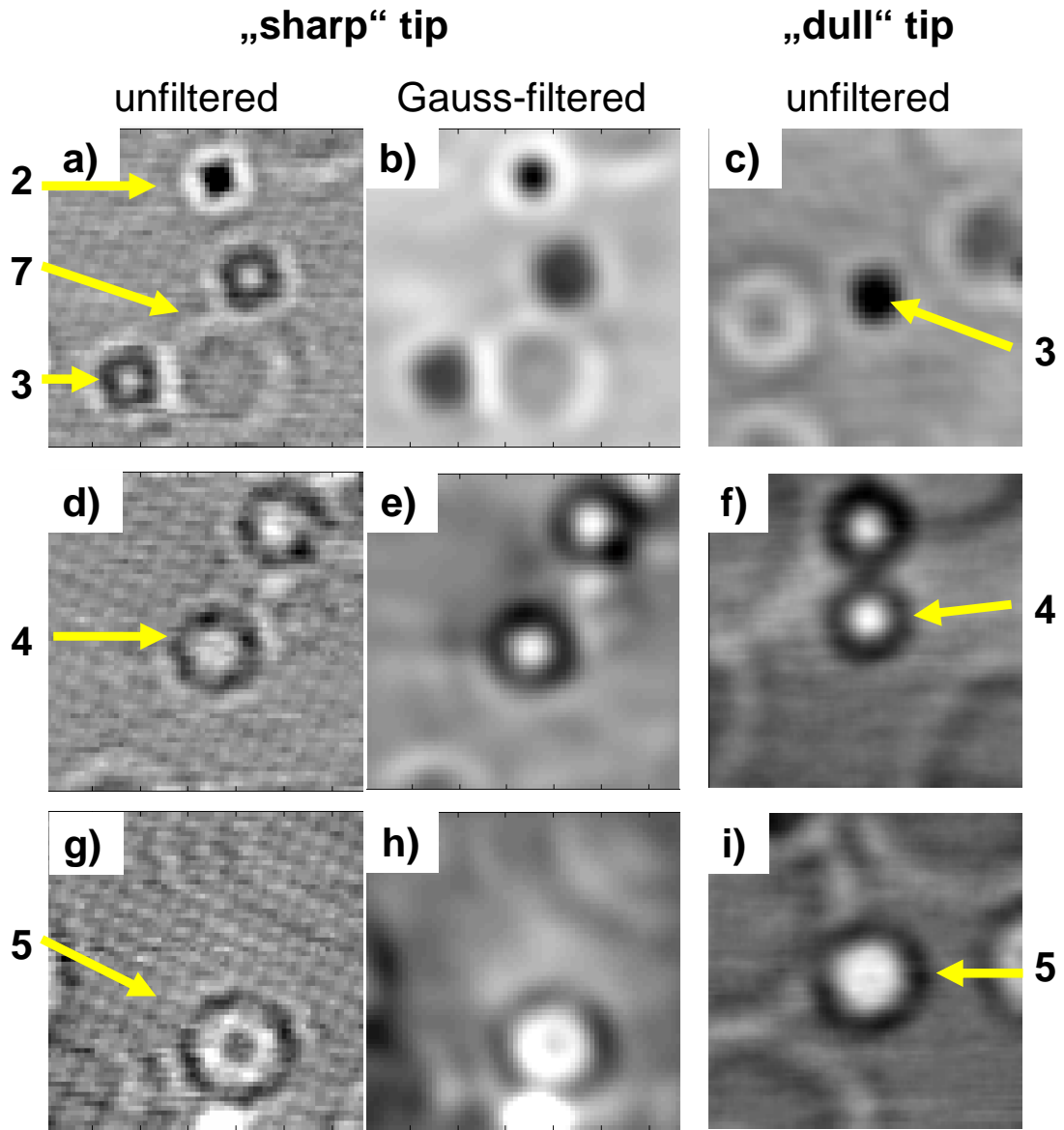


Figure 3.15: *Effect of different tip-conditions on STM-measurements ($3.5 \times 3.5 \text{ nm}$) taken at identical tunnelling parameters ($U_B = -50 \text{ mV}$, $I_T = 1 \text{ nA}$): The left side shows the unfiltered data taken with a new tip. The identical data is shown in the middle after convolution with a $\sigma = 1.8 \text{ \AA}$ Gaussian. The right side shows data measured after several tip-sample collisions.*

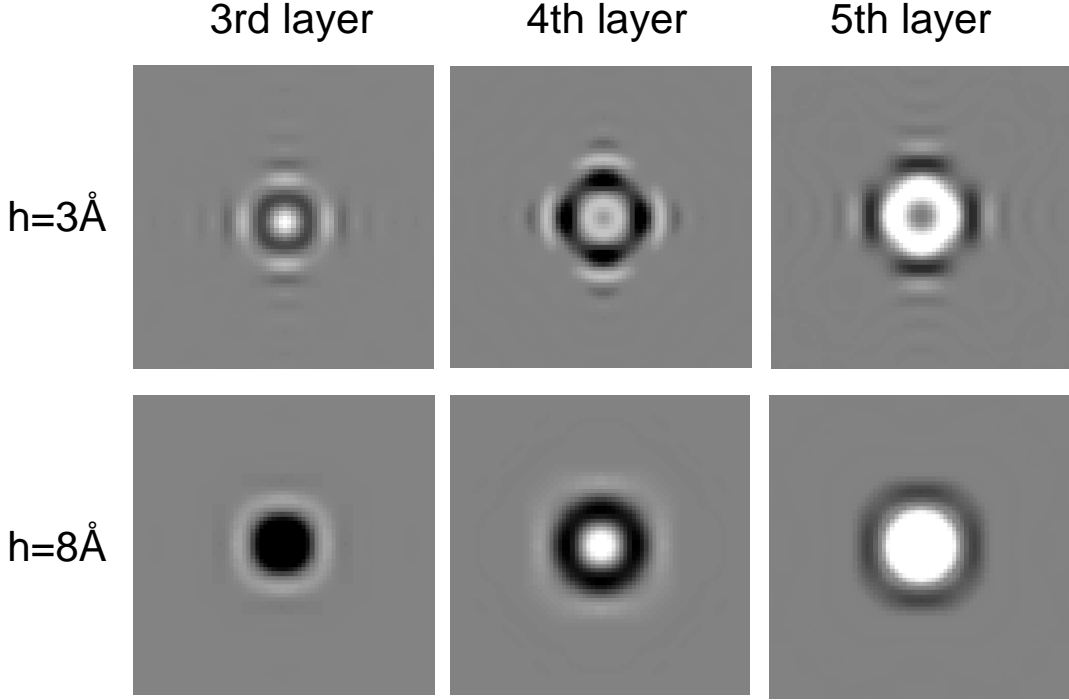


Figure 3.16: Calculations ($3.5 \times 3.5 \text{ nm}$) for different tip-sample distances h . The impact of different tip-qualities can be reproduced in the calculations.

LDOS-distributions, the filtered images have a striking similarity to the topographies measured with a dull tip. Under inferior tip conditions 3rd layer impurities are imaged as broad depressions. The patterns in Fig. 3.15f), however, correspond to 4th layer impurities, whose atomically resolved STM-image is depicted in Fig. 3.15d). The identical effect can also be observed on 5th-layer defects (Fig. 3.15i)), which have a plateau-like maximum at mediocre tunnelling conditions and are thus similar to the 4th layer atoms of Fig. 3.15d). The atomically resolved 5th-layer impurity, however, shows a minimum in the center of the defect pattern, which is also the case for non-atomically resolved 6th-layer impurities.

We will now test, if the calculations can reproduce this observe behavior. If all approximations are valid, the measured topographies should be described by the identical parameters d and t_{imp} , while h should be larger for the topographies measured using the "dull" tip. For this current analysis we use those values of d and t_{imp} that will later be shown to be appropriate for these impurities and calculate the LDOS for different parameters h . This is done in Figure 3.16

3.4.4 Impact of the tunnelling resistance

Another possibility to check the influence of the tip-sample distance h on the measured patterns is to change the tunnelling resistance. In order to avoid voltage-dependent effects (that will be intensively described in Chapter 4) this analysis is most suitably done by varying the set point current I_T , while keeping the bias voltage V_T constant. The dynamics in tip-sample distance achieved by this approach are very limited as high currents increase the risk of tip-modifications while small values of I_T worsen the signal to noise ratio.

In Figure 3.17 I_T was varied over three decades between $2pA$ and $1.8nA$. Here we used a data acquisition mode, in which every scan line was measured 16 times with different set-point currents I_T before proceeding to the subsequent scan line (*multi-bias spectroscopy*, see Chapter 4.3.1). This mode allows a direct "pixel-by-pixel" comparison of the relative tip-sample distances $h(\mathbf{x}_{||})$ at different tunnelling parameters. Since the chosen values of I_T followed an exponential sequence, the single STM-traces are almost equally separated. The span of h is slightly above 3\AA which is, as I_T is varied about three orders of magnitude, in good agreement with our "rule of thumb". As a variation of 3\AA is small compared to the dynamic of h -values observed in the previous section, we can expect the effect of the different set-point currents I_T on the topographies to be smaller than the impact of different tip conditions.

Figure 3.17 c) shows the STM cross-sections of a 5th-layer Fe atom below the Cu(100)-surface whose topographies are depicted in Figure 3.17 d). These correspond to set-point currents of $1.8nA$ and $20pA$, respectively and thus to a difference in tip-sample distance h of $\approx 2\text{\AA}$. The STM-patterns look quite similar for all set-point values although the size of the local minima directly at and in 0.7 nm distance from the center of the pattern is reduced. Although one could imagine that the $I_T = 20pA$ pattern is a smoothed $I_T = 1.8nA$ STM-image, the effect of a $\Delta h = 2\text{\AA}$ is not as significant than the effect of different tip qualities.

As a second aspect we can focus on the analysis of the "grey background" in the data-set i.e. the relative tip-sample distances on the free surface - a property that should be described by $\varrho_0(\varepsilon_F, h)$. The plot of the logarithmic set-point current versus the relative tip-sample distances follows a perfect linear behavior. A fit results in a slope of $\kappa_{eff} = 1.050(4)\text{\AA}^{-1}$, which would correspond to a work function of $4.20eV$ in a 1D- tunnelling model. However, we discussed earlier that states of different $\mathbf{k}_{||}$ have a different κ . The overall decay of LDOS should be larger at smaller distances and converge to the κ_0 at larger distances. This behavior can be observed in the calculations but obviously not in the experimental data.

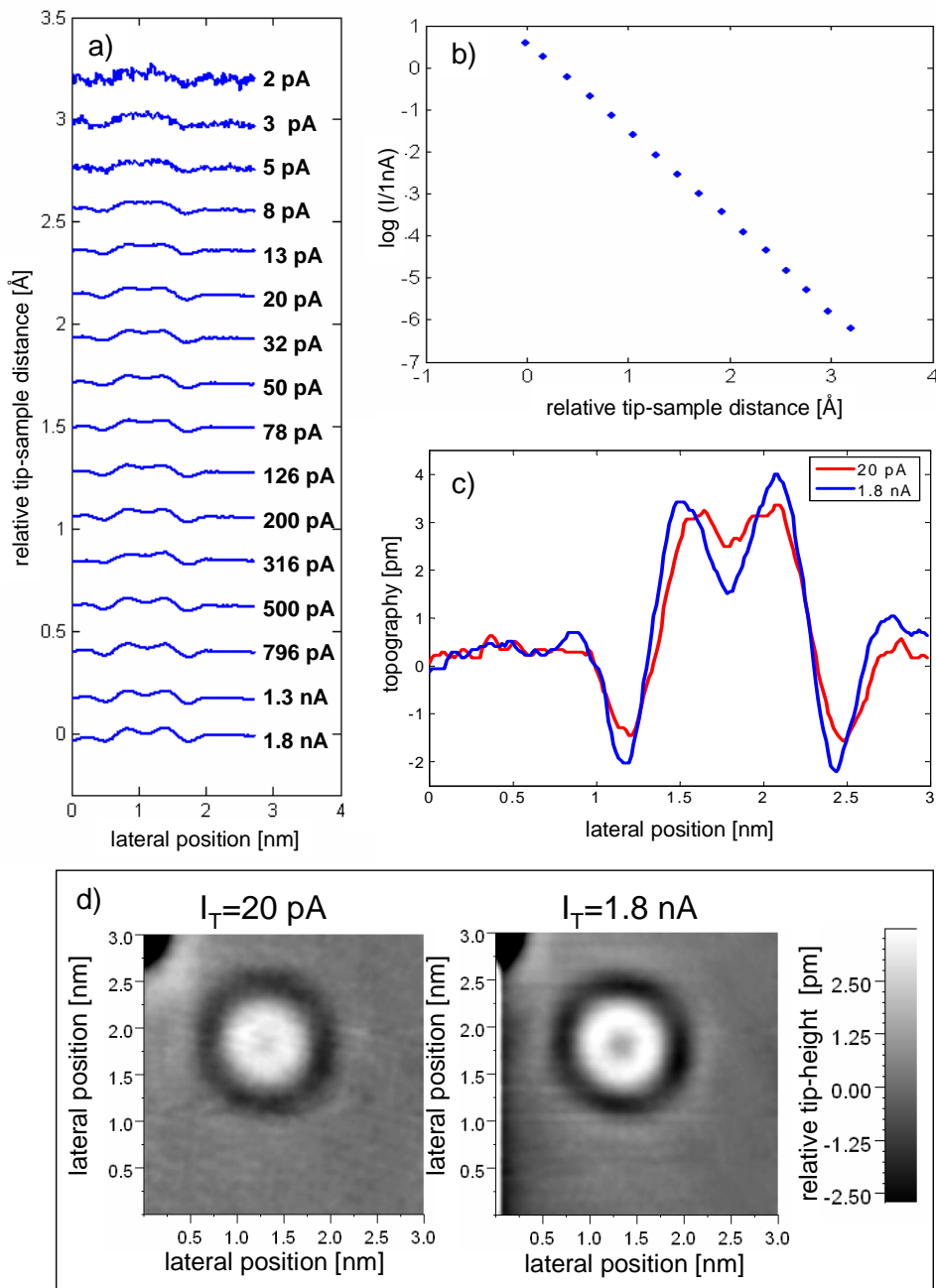


Figure 3.17: Impact of the setpoint-current I_T on the STM-measurements. a) direct comparison of the STM-traces - at $I_T=3\text{pA}$ the tip is in 3\AA larger distance to the sample then for $I_T=1.8\text{nA}$; b) the relative tip-sample distances on the free surface follow an exponential behavior; c) STM traces taken in $\approx 2\text{\AA}$ different tip-sample distances; d) corresponding constant current topographies.

This discrepancy between the expected decay of LDOS into the vacuum and the measured $I(h)$ -characteristic was already elucidated in the early days of STM by Binnig himself [51]. He analyzed the tunnelling current versus tip-sample distance and showed that it unexpectedly follows a purely exponential behavior. He showed that the classic image-potential of an STM tip placed near a metal surface indeed produces a constant logarithmic derivative of the tunnelling current with respect to the distance. The measured decay constant is the square-root of the *average* work function of tip and sample. Here the Tersoff-Harmann approximation, which our calculations are based on, gives inaccurate results.

3.5 Comparison between experiments and calculation

With the knowledge achieved in the last sections, we can now try a detailed comparison between experiments and the calculations. It will now be revealed whether all the assumptions and approximations ($u_k(r) = 1$, point scatterer, step-function surface potential) are legitimate.

The model contains the smallest possible number of parameters while considering all prominent physical effects. Attempts to improve the model e.g. by assuming an extended impurity potential, by modeling the surface in a more realistic way or by including $u_{\mathbf{k}}(\mathbf{x})$ would inevitably result in additional parameters, which are neither *a-priori* known nor under experimental control. In our approach we only have three parameters:

1. d : the depth of the impurity below the "surface"
2. h : the distance between the "surface" and the center of the STM-tip
3. t_{imp} : the (complex) t-matrix containing scattering amplitude and -phaseshift.

The possible depths d of the impurity should differ by integer multiples of the layer spacings $a_{[100]} = a_0/2$, with $a_0 = 3.61\text{\AA}$ being the lattice constant of copper. Of specific interest is the unknown quantity a_s in Figure 3.18, the distance between the plane of the topmost nuclei and the "surface", i.e. the supposed plane, where the electrons switch from an oscillatory propagation to an exponential decay. If the atoms were treated as hard spheres, a_s would correspond to $0.7a_{[100]}$. The nucleus of e.g. a 4th layer impurity would in this case be expected 3.7 mono-layers (ML) below the "surface". However, since we do not want to restrict ourselves to a hard sphere picture, d is leaved as an continuous parameter in the model.

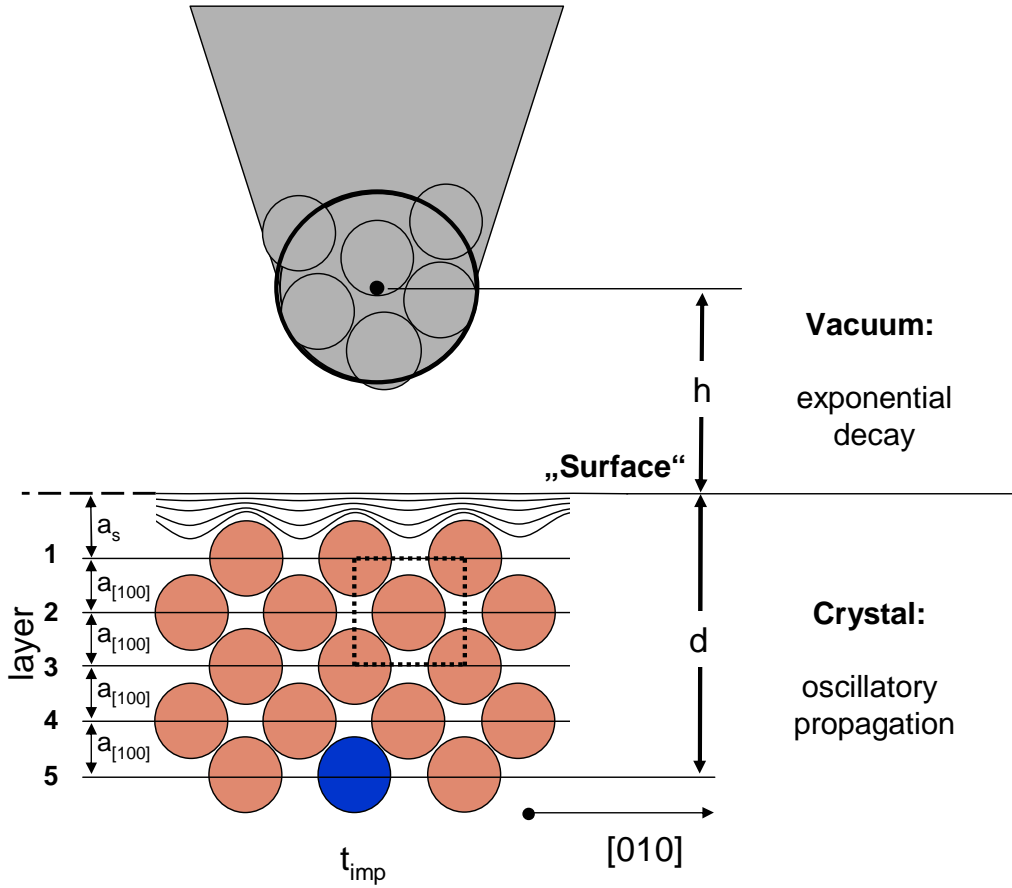


Figure 3.18: Overview of model parameters and notations of impurity depths. The distance from the topmost nuclei to the "surface" is denoted by a_s . First layer impurities correspond to defects in the surface layer and are described with $d = a_s$.

3.5.1 Data processing and fitting

In order to perform a quantitative comparison between the experimental data and the calculations, it has to be assured that the STM data is properly calibrated. As atomic resolution was achieved at least once during the experiments of each prepared sample, direct information about the orientation of crystallographic directions, the inaccuracy of the chosen piezo constants and the mis-angle of x and y -axis are available. These atomically resolved data were used to calibrate the STM-topographies of the entire data-set. For this a 2×2 -Matrix M was calculated defining a shearing, stretching and rotation of the image's coordinate system. This procedure is shown in Figure 3.19. The raw data were Fourier transformed and the positions of the the lattice peaks were determined. After that a matrix \tilde{M} was obtained that mapped

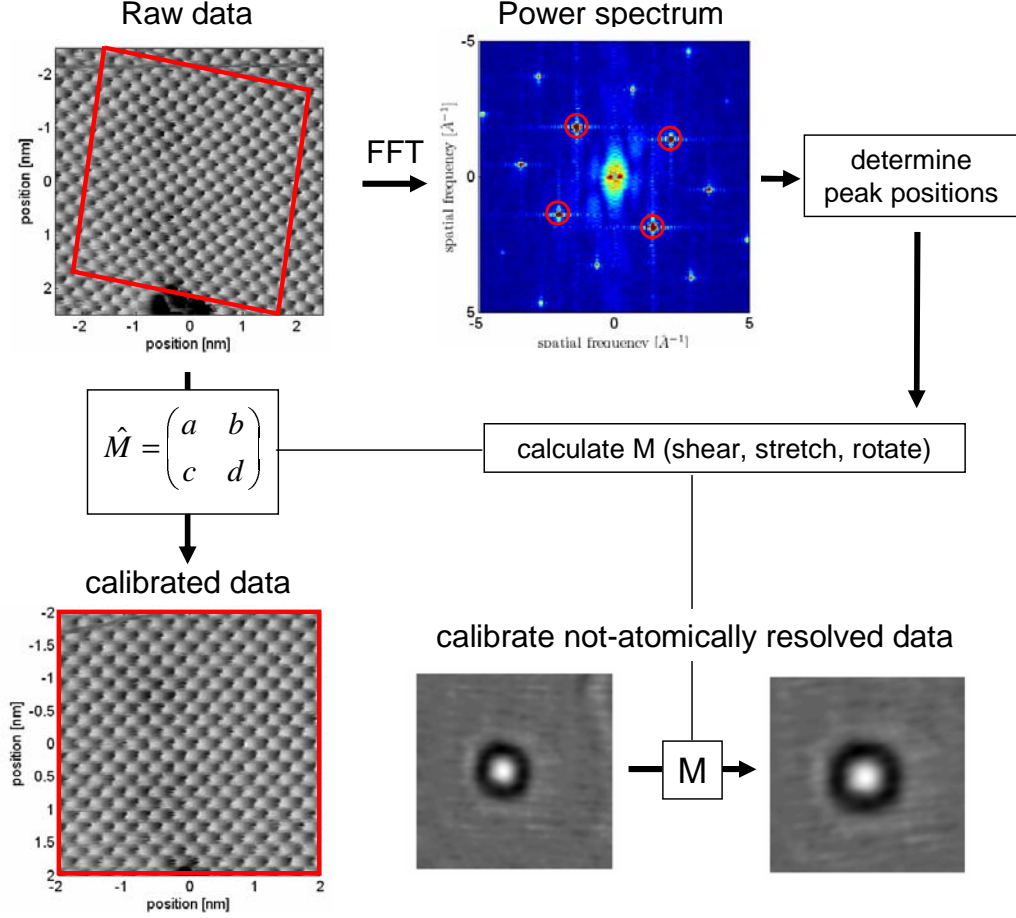


Figure 3.19: Procedure used for the calibration of the STM-data

the k-space positions of the lattice peaks onto the desired positions by solving a system of linear equations. The required matrix M necessary to correct the real space coordinates can be obtained from the "k-space" matrix \tilde{M} by $M = (\tilde{M}^\dagger)^{-1}$. The calibrated images were oriented with the [001] axis parallel to the x-axis. The STM-data on the corrected coordinate grid were finally interpolated into an regular, orthogonal grid.

This procedure has been performed on every data set that was used for the comparison. After these calibrations cross sections were taken along high-symmetry directions through the center of the measured STM-pattern. To determine the appropriate parameters (d, t_{imp}, h) of our model it was attempted to fit the LDOS - as calculated along a line - to these experimental cross-sections. From the theoretical side, the Green function G^{VC} was calculated for a variety of different impurity depths d (0..15ML, increment 0.1ML) and tip-sample distances h (0..20 \AA , increment

1\AA), while $\Delta\mathbf{x}_{\parallel} = \mathbf{x}_{\parallel} - \mathbf{x}'_{\parallel}$ was restricted to the one crystallographic direction, which was also chosen for the cross-section (mostly [001]). For any pair of values (h, d) a nonlinear least-squares data-fitting routine was used to obtain the optimal values for scattering amplitude and phase shift (parameter $t_{imp}(h, d)$) and the squared 2-norm of the residual $\chi^2(h, d)$. The latter is a measure for the quality of the obtained agreement. For those values of d and h that gave the best agreement, G^{VC} was calculated unrestricted in $\Delta\mathbf{x}_{\parallel}$ to allow the computation of two-dimensional LDOS patterns.

It should be noted that the measured topographies can - to a certain extent - be fitted with different parameters. Although the accuracy in d is better than 1 mono layer (i.e. the attempt to fit a 5th-layer calculation to a 4th layer topography will result in a poor agreement), a small variation in d of $+0.1ML$ can be compensated by a reduction of the scattering phase-shift ϕ of about -0.14π : if we move the impurity away from the surface, the phase fronts have to be pushed outward from the impurity in order to obtain a comparable pattern at the surface. This may result in confusion because the fitting of different impurities may result in different values of a_s , which in turn results in non-uniform phase-shifts. To avoid this we now present only data with a preselected $a_s = 1.3a_{[100]}$, which turned out to give the most consistent results for all analyzed experimental data. If the possible impurity depths are restricted to $d = X.3 ML$, this results in a uniform phase shift of $\approx 1.1\pi$. This will be shown in the next section.

3.5.2 Defects below the Cu(100)-surface

The comparison will be performed using a calculated $\varrho(\mathbf{x}, \varepsilon_F)$ at the Fermi energy and measured constant current topographies taken at bias voltages close to $0V$. Although only little change can be observed in the measured topographies within $\pm 10mV$ for the case of cobalt atoms, the observed modulations of Fe atoms are very sensitive to the applied bias voltage close to $0V$. This energy dependence will be extensively discussed in the next chapter. From this it is important for the present analysis to compare all impurity depths at identical tunnelling voltages and to use the identical impurity species. The following comparison was performed at $V_B = -10mV$ and $I_T = 1.8nA$ using cobalt impurities. This choice has been made because for these tunnelling parameters the largest amount of experimental data was available.

Since the presented calculations are based on the (anisotropic) propagation of electrons in copper there must be at least one layer of host material between the impurity and the surface. We therefore start the classification with 2nd layer defects. They

are depicted in figure 3.20 a) and are characterized by a sharp minimum of topography in the center of the defect pattern surrounded by a weak, halo-like elevation. The distinctness of this halo depends on the tip quality. An atomically resolved 2nd-layer Co atom was already depicted in Figure 3.15 a). In general one has to be very careful not to mix up these defect patterns with some kind of adsorbates (e.g. CO , H_2) that also produce depressions in the constant current topographies and are also of small lateral extension. This discrimination can be more clearly done for impurities deeper in the bulk because they reveal *oscillations* rather than just a depression. Anyhow, the calculations show that such narrow signatures are expected from 2nd layer point scatters and can be reproduced using the identical values for h and t_{imp} that will also show to be appropriate for the other impurity depths.

The STM signatures produced by third layer impurities are also depressions but are more broadened compared to those of the 2nd-layer Co atoms. Here, tiny local maxima can be observed in the middle of the signature and in a lateral distance of 5\AA . In this case the term LDOS-*oscillation* is more justified than for the 2nd layer defects since more than one wavelength can be identified. Here, the characteristic four-fold symmetry can also be observed, which is related to the symmetry of the Fermi surface in $[100]$ direction.

The four fold symmetry and the clear presence of oscillations in the STM-pattern can also be seen for all impurities that are buried deeper below the surface. Here the lateral envelope due to the electron focusing effect has sufficiently widened to observe more than one oscillation.

3.5.3 Defects below the Cu(111)-surface

We now want to have a quick look at the Cu(111)-data. Here, only systems of subsurface cobalt impurities have been prepared. As could be seen in Figure 3.1a) an isotropic surface state is present on these surfaces and produces omnipresent and long-range standing wave-patterns near step-edges and point-defects. While these observations are fascinating in some way, they hinder the analysis of the subsurface defects as the amplitude of the surface state oscillations is comparable to the amplitudes of the LDOS-modulations induced by subsurface defects. This can be seen in Figure 3.21 where long-wavelength surface state oscillations and four short-wavelength signatures of deeply buried defects can be observed.

The impurities in general show different signatures depending on their depths below the surface. Adsorbates or impurities in the surface layer produce only strong,

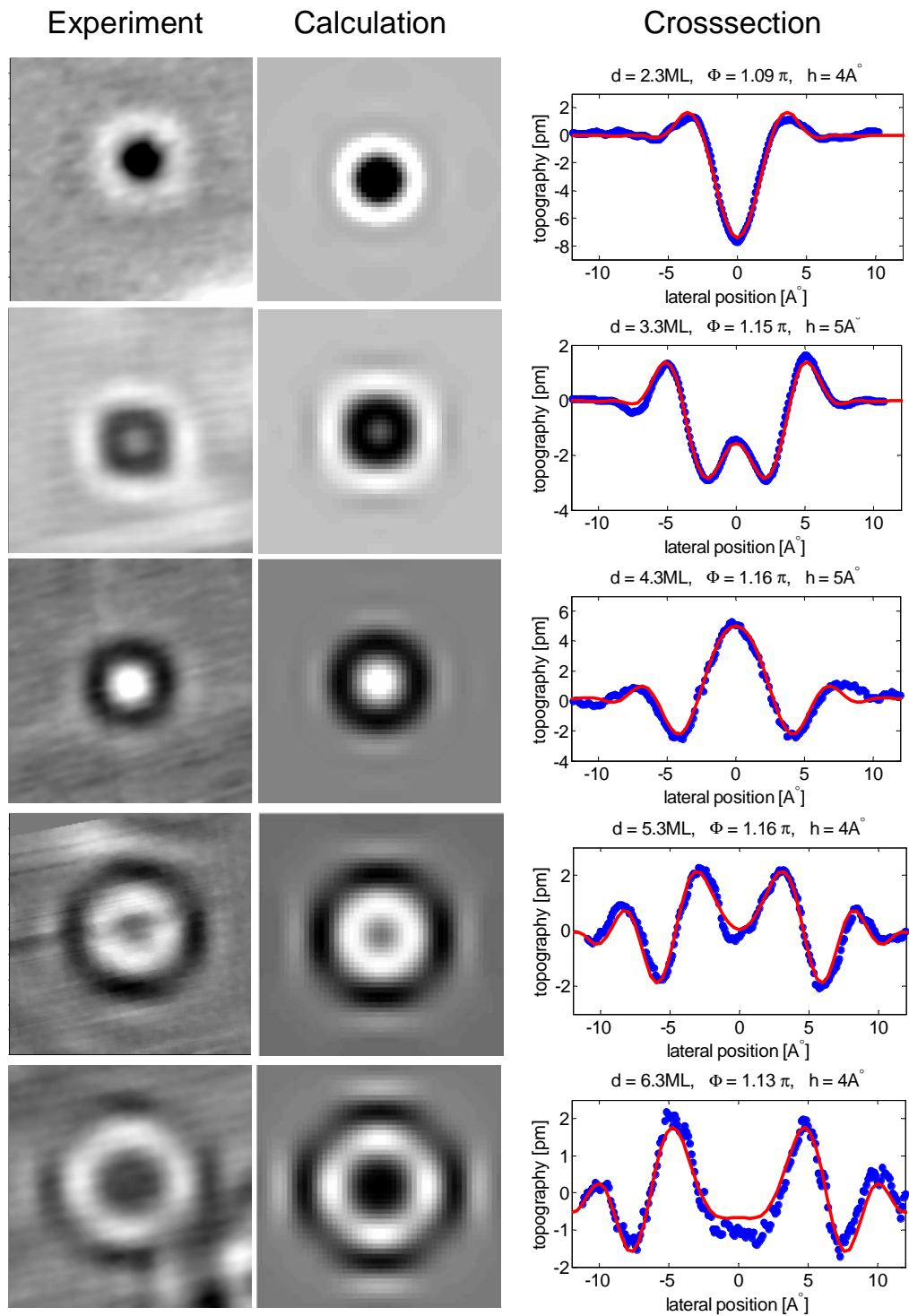


Figure 3.20: Comparison between the experimental data and the calculations for impurities in the layers 2 to 6. In the depicted cross-sections blue markers correspond to measured topographies while red lines are calculations.

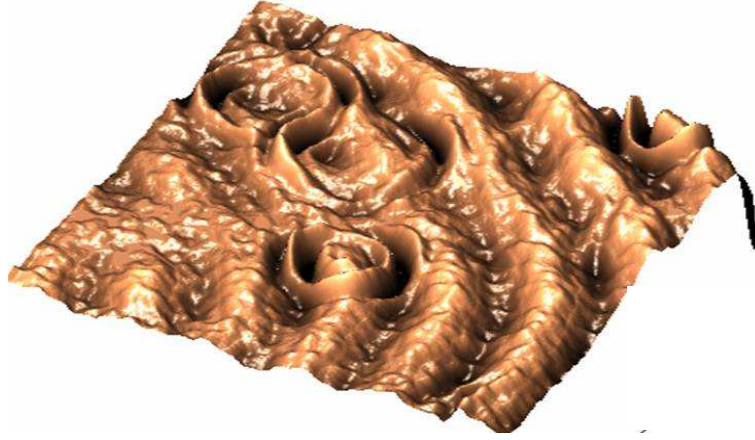


Figure 3.21: *Constant current topography Co impurities in Cu(111): interference patterns of surface-states (long wavelength) and bulk states (short wavelength).*

circular symmetric interference pattern of the surface state electrons. If the impurities are positioned within the first five subsurface layers the long wavelength pattern becomes weaker and additional, short wavelength modulations can be observed. Impurities which are buried deeply below the surface (as seen in Fig. 3.1 a)) do not show any perturbation of the surface state and show the ring-like focusing patterns that were discussed previously. All these different patterns are described in detail in the author's diploma thesis [29] as well as in the Ph.D-thesis of Quaas [28, 52].

The presented model is based on the bulk band structure and does not contain any surface states. Also processes where an incident surface state electron is scattered into a bulk state and vice-versa are not included. Thus, only impurities being out of range of the surface state electrons can be properly described by the model. According to [43] this applies to impurities below the 5th layer.

To allow a successful fitting of the calculations to the experimental data, the surface state oscillations have to be removed. This was done by Fourier filtering and is shown in the upper part of Figure 3.22. The extracted bulk-state interference patterns show a slight threefold symmetry as it is expected from the symmetry of fcc Brillouin zone in [111]-direction. The same symmetry can also be observed on the calculations, which are depicted below. From this, the four subsurface impurities can be allocated to the 6th, 7th 9th and 10th layer.

Especially the fact that the surface state patterns have to be removed by Fourier filtering to allow a successful fitting hinders the further spectroscopic investigation of

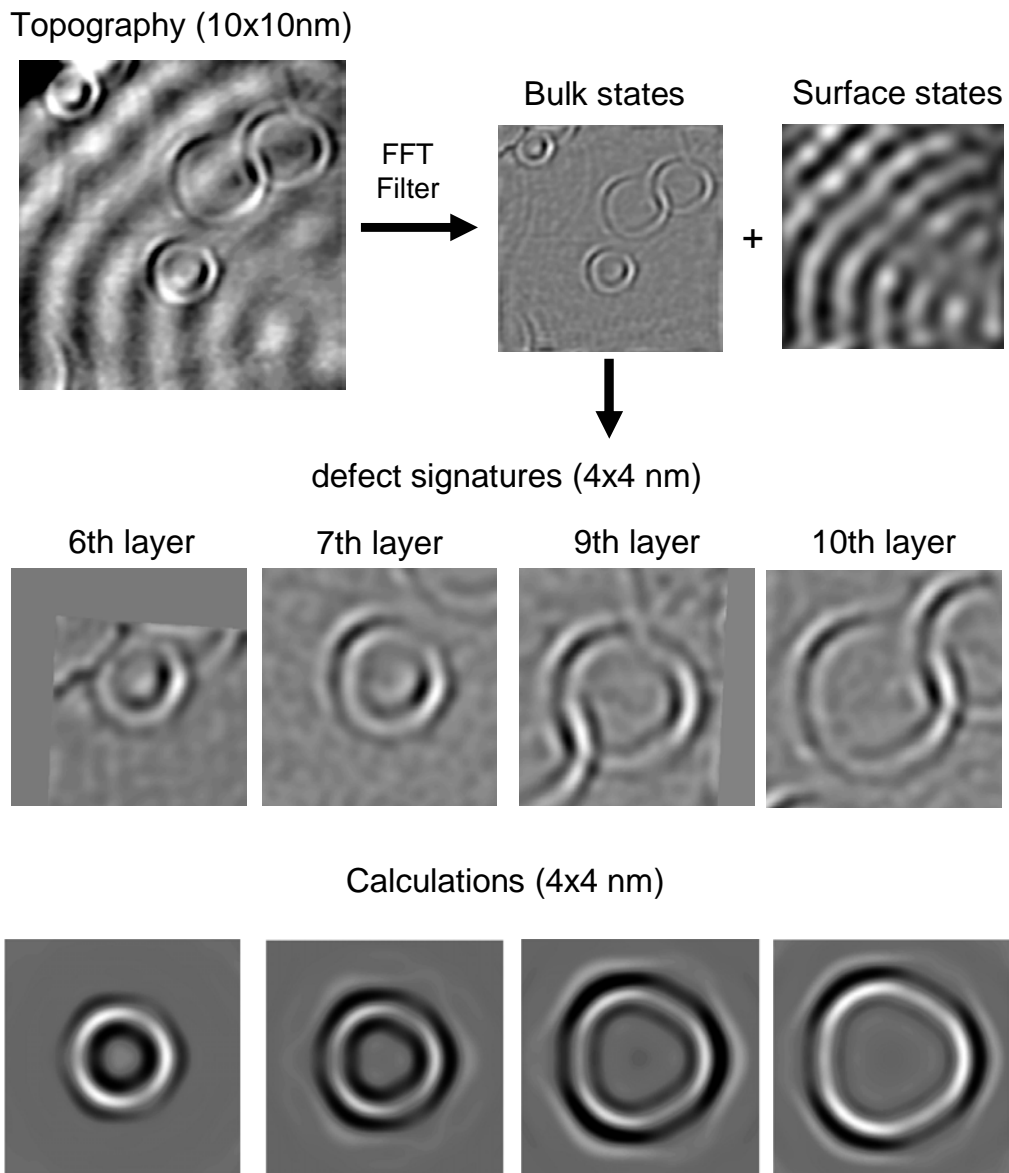


Figure 3.22: *impurities below the Cu(111) surface. The upper part shows the removal of the long wavelength oscillations arising from the surface state electrons by Fourier filtering. The filtered STM signatures and the corresponding calculations are depicted below.*

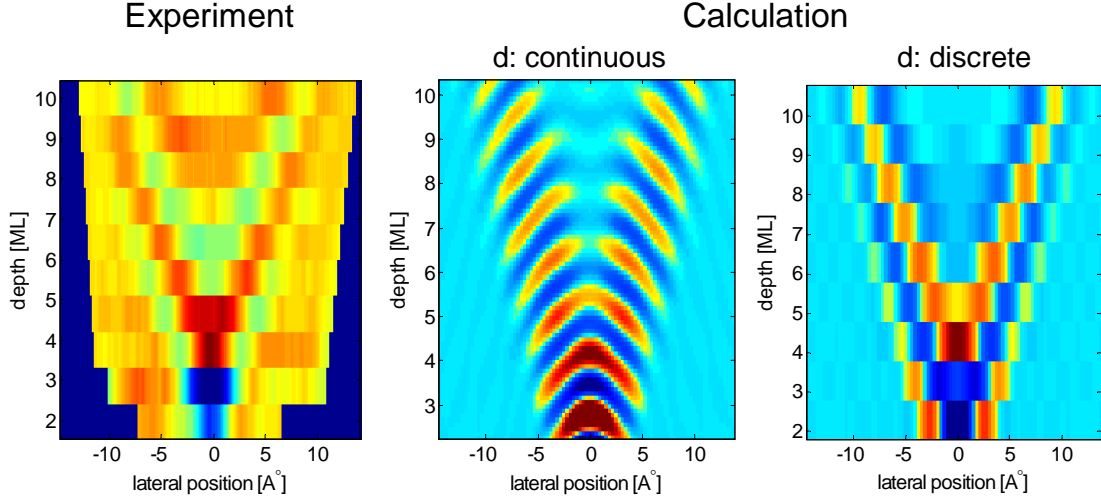


Figure 3.23: a) experimental cross-sections of impurities in layers 2-10 are plotted in series; b) calculated $-\text{Im}(t_{imp}G_0^2)$ for continuous values of d and c) for $d = X.3ML$ $X=2..10$ and a phase-shift of 1.15π .

the subsurface defects. If the bias voltage is modified the standing wave-patterns of the surface state electrons change significantly. This is impressed on the information contained in dI/dV -spectra. If a spectrum is considered only at a single position these contributions from surface- and bulk-states cannot be distinguished. And even if STS data at different lateral positions is compared, a separation of both contributions is only approximately possible. Thus, the further spectroscopic analysis of subsurface defects was only performed on impurities below the (100) surface.

3.5.4 Reconstruction of the propagator from STM-data

As stated before, the LDOS-pattern in the vicinity of the impurity is associated with interference term $G_0 t_{imp} G_0$ containing the squared propagator and the scattering behavior t_{imp} of the impurity. The comparison between experiments and our calculations revealed a roughly constant scattering phase-shift for all impurity depths. Thus, if we assemble the measured topographies in the correct order, this should allow a direct mapping of the squared Green function. This was performed in Figure 3.23 a). Here, the cross-sections of Co impurities buried 2-10 ML below the Cu(100) surface have been plotted in series. It can be seen that this procedure provides a consistent pattern and that the positions of the maxima shift outward linearly if the depth is increased. This indicates that the depth classification was done correctly and that a reconstruction of the propagator should be possible.

We now use those values for h and t_{imp} that successfully described the experimental observation and plot the function $-\text{Im}(t_{imp}G_0^2)$ versus \mathbf{x}_{\parallel} and d (Fig. 3.23b)). Since the fitting worked well, this should give a pattern comparable with Fig. 3.23a). However, a striking difference to the experimental results can be seen. The phase fronts of the calculated propagator have a completely different orientation than those of the "measured" (squared) Green function.

The explanation for this effect is an aliasing between the wavelength of the LDOS oscillations and the periodicity of the atomic lattice. The size of Fermi surface is close to the extension of the first Brillouin-zone. In some directions the Fermi wavevector even reaches the zone boundary. This means that the wavelength π/k_F of the LDOS oscillations is marginally larger than the inter-atomic distances. Although the STM can probe the LDOS pattern with a high resolution parallel to the surface, it can sample the perpendicular direction only in integer multiples of 1.8\AA . This is because the possible positions of the impurities differ by integer lattice spacings. The effect can be reproduced, if the calculated function $-\text{Im}(t_{imp}G_0^2)$ is plotted only for integer distances to the impurity (Fig. 3.23 c)).

3.5.5 Comparison with *ab-initio* calculations

The results presented before showed a good agreement with the experiments although many important points were neglected. While taking care of the correct shape of the Fermi surface the lattice-periodic part $u_{\mathbf{k}}(\mathbf{r})$ of Bloch wave functions kept unconsidered. The crystal surface entered as a step-like switch-over from oscillatory propagation to exponential decay without considering a more realistic surface potential. The existence and possible perturbation of surface states for the case of Cu(111) was also not included in the calculations. The physical details of the impurity atom were parameterized as reflectivity and phase-shift. These parameters had to be adjusted as fitting parameters to obtain agreement with the experiment. However, this procedure produces accurate results within a few minutes of computational time.

In contrast to this, an *ab-initio* approach results in heavy calculations since the LDOS is disturbed in large regions resulting in hundreds of unit-cells that have to be considered. Lounis *et al* [53] met the challenge and simulated up to 3000 atomic cells using the full-potential, scalar-relativistic Korringa-Kohn Rostoker (KKR) Green function method within *Density Functional Theory*. He constructed a slab of 18 layers copper enclosed 6 "vacuum" layers on top and below. For this system he calculated the Green function, which - in contrast to the one used in this work - included surface states and the lattice periodic part of the wave functions. He afterwards calculated the t-matrix of a single cobalt atom within an infinite copper

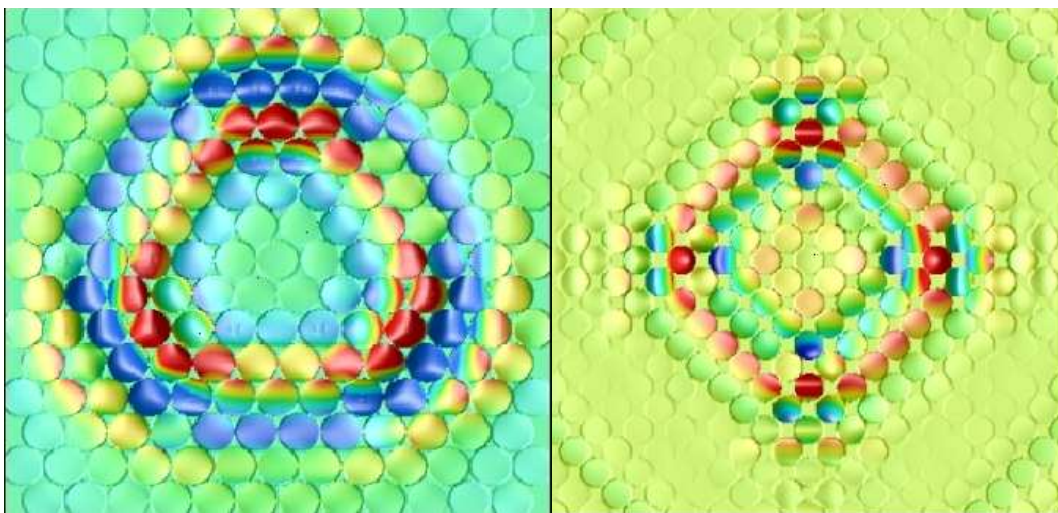


Figure 3.24: Results of DFT calculations performed by Lounis et al [53] showing the vacuum LDOS of a buried Co-atom in copper: a) $(3 \times 3 \text{ nm})$ 7 ML below the $\text{Cu}(111)$ surface and b) $(4 \times 4 \text{ nm})$ 9 ML below $\text{Cu}(100)$.

crystal and combined these two quantities to a Green function of the perturbed system using the Dyson equation. The results of the local density of states are shown in Figure 3.24. They are in quite nice agreement with both, our experimental results and the LDOS distribution obtained by our calculations.

Chapter 4

Kondo Effect of subsurface magnetic atoms

The previous chapter dealt with the identification of single subsurface impurity atoms in STM topographies and their allocation to different depths. We presented a simple model based on the host metal's band structure that showed good agreement with both, the experiments and the results of more elaborate *ab-initio* calculations. Up to now we did not consider the fact that *magnetic* impurities have been prepared below the copper surface. As mentioned in the introduction such systems are known to show characteristic low-temperature anomalies, which are summarized by the term "Kondo Effect" [13, 15]. The task of this chapter is to study the Kondo signatures of bulk-impurities in real space with the STM.

After a short introduction into the phenomenology of the Kondo Effect, the single impurity Anderson model (SIAM)[54] will be discussed. It is one of the two important models for Kondo systems and will help to deduce the physical key-quantities. Using a toy model we will demonstrate the influence of a Kondo impurity on the spectral density of the surrounding electrons. This knowledge will then be transferred to our experimental system by including the realistic band structure of copper. Thereafter Scanning Tunnelling Spectroscopy (STS) and the different graphical representations used in this work will be introduced. The experimental investigation of the prepared systems will start with the most simple approach: the comparison of Co and Fe impurities concerning the bias dependence of their constant current topographies near $V_T = 0$. We will show that Fe and Co atoms show different behaviour near zero bias. Thereafter, a detailed analysis of STS measurements performed on both impurity species in different depths will be presented. Using the Green function of copper that was calculated in the last chapter we will finally fit

energy dependent LDOS calculations to the measured STS-spectra in order to determine the scattering phase shift and scattering amplitude as a function of energy. This will allow to extract the dynamics of the impurity.

4.1 Phenomenology

The liquefaction of helium, developed by *H. K. Onnes* in 1908, opened the door to a new world of physics, which directly led to the discovery of many new effects in the following years. Immediately after gaining the possibility to achieve low temperatures, he discovered superconductivity on mercury [55]. The abrupt loss of electrical resistance below a critical temperature T_C demonstrated that many aspects of charge transport were not yet understood.

In the following years, the low temperature behaviour of many materials was intensively studied. In 1933 Hildebrand *et al* [14] discovered an increase in the resistance with decreasing temperature leading to a *resistivity minimum* around a specific temperature. Later the temperature, around which the increase of resistivity was observed, was termed Kondo temperature T_K . For both cases, superconductivity as well as the observed resistivity minimum, the application of a magnetic field B destroyed the observed anomalies [56] [57] if the corresponding Zeeman energy $\mu_B B$ exceeded the specific energies scales $k_B T_K$ and $k_B T_C$, respectively.

Jun Kondo [13] showed in 1964 using perturbation theory that a resistivity minimum can be explained by the presence of magnetic impurities. By including scattering processes, where the spin of both the impurity and a conduction electron is likewise flipped, he described experimental observations around T_K correctly but got an unphysical divergence of resistivity at $T = 0$. In contrast the experiments revealed a saturation of the electrical resistance for $T \ll T_K$. This fact initiated intensive theoretical interest in the field of the Kondo Effect leading to the development of new techniques (e.g. the renormalization group [58] or the variational $1/N$ expansion [59]). It was shown that a narrow many-body resonance (the Abrikosov-Suhl [16] resonance) builds up in the one-particle spectrum of the impurity at the chemical potential if the temperature is decreased below T_K . Since the charge transport is dominated by quasi-particles near the Fermi energy and this resonance implies a strong scattering at the chemical potential, the behaviour of the electrical resistance was explained.

Near the characteristic temperature T_K , which depends on the combination of impurity and host material, multiple physical quantities as the susceptibility, the thermoelectric power, the specific heat among others show characteristic features. They

are summarized in [15]. As an example the susceptibility shows that the magnetic impurity apparently loses its magnetic moment for $T < T_K$. This is due to the fact that the many-body ground state of the system is a *singlet* and the spin of the impurity is screened by the conduction band electrons. Thus the spin-expectation value of both the impurity and the conduction band electrons is zero but a correlation of both spins is present near the impurity.

4.2 Energy dependence of $\rho(\mathbf{x}, \varepsilon)$ near an impurity

In this chapter we are particularly interested in those aspects of the Kondo Effect that can be measured with STM. As was mentioned in chapter 2 the STM is sensitive to the *local density of states* $\rho(\mathbf{x}, \varepsilon)$. While topographies with bias voltages close to 0V correspond to the LDOS at the Fermi energy, Scanning Tunnelling Spectroscopy, which will be introduced in Chapter 4.3, will give us access to the *energetic* dimension of the quantity $\rho(\mathbf{x}, \varepsilon)$.

In a many-body system the term *density of states* has to be replaced by the single-particle spectral density at a certain position and a certain energy [17]. We will use the same symbol for both quantities, since their formalism concerning the Green functions and t-matrices is identical.

We now want to analyze how $\rho(\mathbf{x}, \varepsilon)$ is modified in the vicinity of an impurity and how this property is affected by the Kondo Effect. We will again start with a simple one-dimensional toy-model and apply the achieved knowledge to the realistic band structure of copper afterwards.

4.2.1 Resonant impurity scattering and Fano line shapes

A standard model to describe the interaction between a localized state and a continuum of conduction band states is the Anderson impurity model [54], which is - in addition to the sd-model [60] - commonly used in the context of Kondo physics. The corresponding Hamiltonian is:

$$H = \sum_{\mathbf{k}, \sigma} E(\mathbf{k}) c_{\mathbf{k}\sigma}^\dagger c_{\mathbf{k}\sigma} + \epsilon_d c_{d\sigma}^\dagger c_{d\sigma} + \sum_{\mathbf{k}, \sigma} \left(V_k c_{\mathbf{k}\sigma}^\dagger c_{d\sigma} + V_k^* c_{d\sigma}^\dagger c_{\mathbf{k}\sigma} \right) + U c_{d\downarrow}^\dagger c_{d\downarrow} c_{d\uparrow}^\dagger c_{d\uparrow} \quad (4.1)$$

Here the operators $c_{\mathbf{k}\sigma}^\dagger/c_{\mathbf{k}\sigma}$ create/annihilate an electron with spin σ in a conduction band state $|\mathbf{k}\rangle$ with energy $E(\mathbf{k})$, c_d^\dagger/c_d create/annihilate an electron in the impurities localized orbital $|d\rangle$ at energy ϵ_d and V_k describes the hybridization between the conduction band and the impurity. U is the coulomb repulsion between two electrons within the localized orbital.

One-particle example (1D)

First of all we want to analyze how the LDOS is influenced in a one-particle system. For convenience this is performed in one dimension and the generalization to the 3D many-particle case will be done later. With only one particle in the system, the two-particle interaction U is of no relevance. This *non-interacting* Anderson model can be solved analytically as described in the book of *Mahan* (Chapter 4.1) [17]. The example presented here was solved by computational matrix diagonalization.



Figure 4.1: *geometry of the one-dimensional impurity model.*

By using the basis set $\{|d\rangle, |k_1\rangle, |k_2\rangle, \dots, |k_n\rangle\}$ the ansatz for the single-particle wave functions is

$$\Psi_\alpha = v_{1,\alpha}|d\rangle + \sum_{i=1}^n v_{1+i,\alpha}|k_i\rangle = v_{1,\alpha}c_{d\sigma}^\dagger|0\rangle + \sum_{i=1}^n v_{1+i,\alpha}c_{k_i}^\dagger|0\rangle \quad (4.2)$$

Within this representation the single-particle Hamilton matrix is:

$$H = \begin{pmatrix} \epsilon_d & V_{k_1} & V_{k_2} & \cdots & V_{k_n} \\ V_{k_1}^* & \epsilon_{k_1} & 0 & \cdots & 0 \\ V_{k_2}^* & 0 & \ddots & \ddots & \vdots \\ \vdots & \vdots & \ddots & \ddots & 0 \\ V_{k_n}^* & 0 & \cdots & 0 & \epsilon_{k_n} \end{pmatrix} \quad (4.3)$$

As we intend to show only the qualitative behaviour, we can freely choose appropriate parameters: i) a linear dispersion $E(\mathbf{k}) \propto |k|$ resulting in a constant, energy-independent LDOS ϱ_0 of the unperturbed system, ii) a k -independent $V_k = V$ resulting in point-like hybridization at position $x = 0$ and iii) ϵ_d inside the energetic

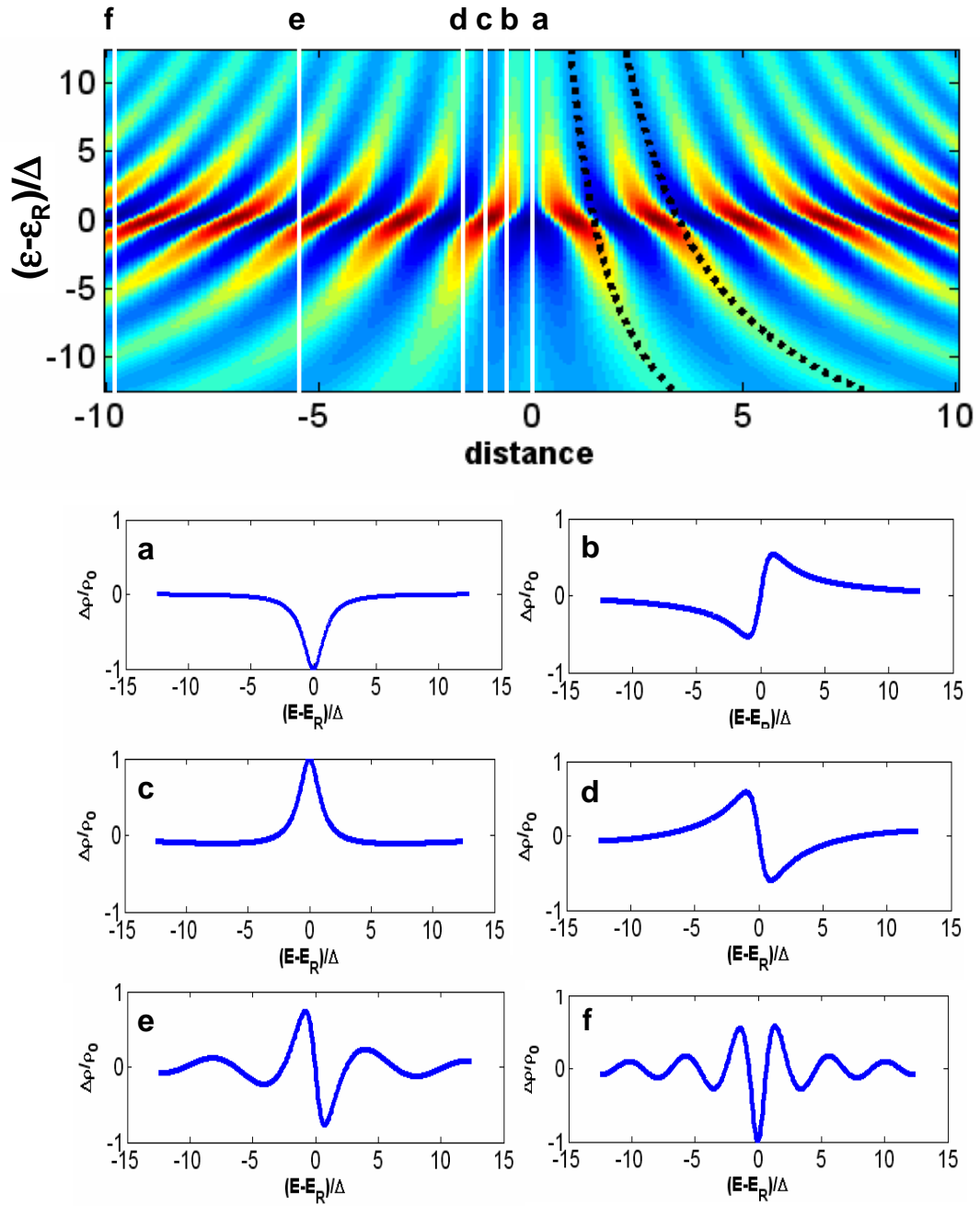


Figure 4.2: Influence of a scattering resonance on the LDOS in the vicinity of the impurity. The impact of the bare dispersion is indicated by a punctuated line. Coming from the low-energy side the wave pattern additionally "shrinks" about half a wavelength within the resonance. At the positions a)-f) according to different distances from the impurity, spectroscopic signatures of varying symmetry can be observed near ε_R .

range of the conduction band states. Diagonalizing the matrix H gives $(n + 1)$ eigenenergies E_α and eigenvectors $v_{i,\alpha}$. From this one can obtain the d-orbital DOS $\varrho_d(\varepsilon)$:

$$\varrho_d(\varepsilon) = \sum_{\alpha} |v_{1,\alpha}|^2 \delta(E_\alpha - \varepsilon) \quad (4.4)$$

as well as the conduction band local density of states $\varrho(\varepsilon, x)$ using $|k\rangle = \exp(ikx)$:

$$\varrho(x, \varepsilon) = \sum_{\alpha} \delta(E_\alpha - \varepsilon) \left| \sum_i v_{1+i,\alpha} \exp(ik_i x) \right|^2 \quad (4.5)$$

Without hybridization $V = 0$, the conduction band local density of states $\varrho(x, \varepsilon)$ is constant in x and ε (due to linear dispersion in 1D) while $\varrho_d(\varepsilon)$ is a δ -function at energy ε_d . If V is increased oscillations in $\varrho(x, \varepsilon)$ appear as depicted in Figure 4.2.

Such a graphical representation, where the LDOS (or the differential conductance dI/dV in STS) is depicted with colors versus position and energy, is termed **Spectrum section** in the following. As we currently discuss a 1D-model the full information of $\varrho(\varepsilon, x)$ can be represented in this way. Later, after generalizing to more spatial dimensions the coordinate x will correspond to the one direction of interest (mostly [100]).

Horizontal cross-sections correspond to the spatial arrangement of spectral electron density at a fixed energy. The wavelength of these LDOS oscillations in Figure 4.2 decreases with increasing energy as it is expected from the chosen dispersion relation: $\lambda = \pi/k \propto 1/\varepsilon$. Additionally it is observed that the amplitude of the oscillations shows a maximum around a certain energy ε_R . In the identical energetic range, the positions of maxima and minima are shifted half a wavelength towards the position of the impurity. The punctuated line represents the trajectory of the phase fronts due to the bare dispersion.

The d-orbital density of states $\varrho_d(\varepsilon)$ of this system essentially shows a Lorentzian at energy ε_R with a spectral line width (HWHM)

$$\Delta = \pi|V|^2 \varrho_0 \quad (4.6)$$

Generally this Lorentzian needs not be centered at the energy of the un-hybridized orbital ε_d but can be shifted in energy by a certain amount $\text{Re}\Sigma_d$ - the real part of the d-orbital self-energy Σ (compare [17] for analytical expressions).

If the LDOS at a fixed position x_0 is plotted versus energy this will be termed a **Single spectrum** throughout the following. It corresponds to a vertical cross-section through the depicted conduction band LDOS $\varrho(x, \varepsilon)$ of figure 4.2. At different positions denoted by a-f one can observe lineshapes that strongly depend on

the distance to the impurity. Directly at the position of the impurity a symmetrical antiresonance can be observed (section a). Moving away from the impurity the line shape becomes more asymmetric (section b), turns into a positive resonance at position c and back into an asymmetric line shape at position d. These spectral features are called *Fano line shapes* [61] and can be described by a formula including an asymmetry parameter q :

$$\frac{(q\Delta + \varepsilon - \epsilon_R)^2}{(\varepsilon - \epsilon_R)^2 + \Delta^2} \quad (4.7)$$

The corresponding values of q for the different positions are: a) $q = 0$ b) $q = +1$ c) $q = \infty$ and d) $q = -1$. If the distance from the impurity is further increased, additional oscillations can be seen in the single spectra (e,f). These are caused by the dispersion. Formula 4.7 does not account for these effects and can be applied only at short distances from the impurity.

The physical meaning of the parameter q in our case is somehow different to that originally presented in Fano's paper. He had discussed the impact of interfering transition channels on the measured *intensities* in situations where an experiment (such as photoemission) probes both, the d-level electrons and the conduction band states. In his case q was associated with the relative strength of the competitive transition channels. In contrast to this we solely discuss the conduction band LDOS *but* at different positions x . This effect is also nicely described in the work of *Ujsaghy et al* [27].

Although Fano's q -parameter is commonly used in literature, it is rather inconvenient since values of $q = \infty$ are needed to reproduce a positive Lorentzian line-shape. Thus we define a "q-phase" ϕ_q which can be related to the Fano parameter using $q = \tan(0.5\phi_q)$. With this we can replace equation 4.7 by

$$\frac{\tilde{\varepsilon} \sin \phi_q - \cos \phi_q}{\tilde{\varepsilon}^2 + 1} \quad (4.8)$$

where we defined $\tilde{\varepsilon} = (\varepsilon - \epsilon_R)/\Delta$. The single spectra of Fig. 4.2 can then be described using "q-phases" of a) $\phi_q = 0$ b) $\phi_q = 0.5\pi$ c) $\phi_q = \pi$ and d) $\phi_q = 1.5\pi$. The q-phase increases linearly with the distance to the impurity and has a periodicity of $\pi/k(\epsilon_R)$.

In conclusion, a single-particle scattering resonance produces Fano line shapes in the single spectra, whose asymmetry depends on the distance to the impurity. The LDOS oscillations at certain energies show a phase-shift of π around ϵ_R meaning that the standing wave patterns at energies below and above the resonance are approximately inverted compared to each other.

t-matrix of this system

As described in Chapter 3, modulations of the LDOS are caused by an interference term $G_0 t_{imp} G_0$ containing the propagation G_0 within the unperturbed host and the scattering t_{imp} at the impurity. Therefore, if an energy dependence of the LDOS is observed, this is either due to changes in G_0 or in t_{imp} , or both. As the propagator is directly connected to the band structure, changes in G_0 are due to *dispersion*: a change of the $\Omega(\varepsilon)$ versus energy results in a different wavelength and, potentially, in a modified spatial propagation characteristic. Changes in $t_{imp}(\varepsilon)$ can be connected with scattering resonances. Thus the result for $\varrho(\mathbf{x}, \varepsilon)$ that was calculated by matrix diagonalization can be also obtained by combining the conduction electron Green function of the unperturbed one-dimensional electron gas:

$$G_0(\mathbf{x}, \mathbf{x}', \varepsilon) = -i\pi\varrho_0 e^{i|k(\varepsilon)(\mathbf{x}-\mathbf{x}')|} \quad (4.9)$$

with suitable t-matrix $t_{imp}(\varepsilon)$ that correctly describes the scattering amplitude and phase-shift of the conduction band electrons due to the interaction with the impurity $|d\rangle$. The t-matrix of this system is directly connected to the d-orbital Green function $G_{dd}(\varepsilon)$, which is a local quantity:

$$t_{imp}(\varepsilon) = |V|^2 G_{dd}(\varepsilon) \quad (4.10)$$

Due to the hybridization V , the possible propagation paths of a conduction band electron are extended by processes, where it hops into the localized orbital (V^*), propagates within $|d\rangle$ (described by $G_{dd}(\varepsilon)$) and escapes back into the band (V). The above formula is the product of these three processes. In the same way as the conduction band LDOS was associated with the imaginary part of $G(x, x, \varepsilon)$ (equation 3.4), the d-orbital DOS can be obtained from $G_{dd}(\varepsilon)$:

$$\varrho_d(\varepsilon) = -\frac{1}{\pi} \text{Im} G_{dd}(\varepsilon) \quad (4.11)$$

In the presently discussed case, where the system shows a *scattering resonance* around ε_R , the localized orbital Green function is a complex Lorentzian:

$$G_{dd}(\varepsilon) = \frac{1}{\varepsilon - \varepsilon_R + i\Delta} \quad (4.12)$$

If the hybridization V is further increased, bound states will appear and $t_{imp}(\varepsilon)$ is only weakly energy dependent within the band. We omit the discussion of this case and refer to the literature [17].

Generalizing this example from 1D to higher dimensions (2D, 3D) will result in a decay of the amplitude of the standing wave pattern with increasing distance from the impurity. But this behaviour is fully incorporated in the spatial decay of the corresponding conduction electron propagator in higher dimensions (see Chapter 3.2.2 - electron focusing). The connection between the scattering behaviour $t_{imp}(\varepsilon)$ and the impurities dynamics $G_{dd}(\varepsilon)$ remains valid.

Generalization to the many-body case

If particle interactions are neglected ($U = 0$) the Hamiltonian contains only single-particle operators. Therefore, apart from a shift in the chemical potential, the result keeps unchanged even if the system contains more than one particle. This situation changes if the Coulomb interaction is switched on. The single-particle properties will be *modified* by many-body effects. In the Anderson model, the particles are interacting only within the d-orbital while electron-electron interaction within the conduction band is neglected. Thus these modifications can be derived from a renormalized d-orbital Green function $G_{dd}(\varepsilon)$ that now accounts for many-body effects. The single particle spectral density $\varrho(\mathbf{x}, \varepsilon)$ in certain distances from the impurity can be still calculated using equation 3.16 with using a suitable t-matrix $t_{imp}(\varepsilon)$. The relation between the scattering behaviour $t_{imp}(\varepsilon)$ and the dynamics $G_{dd}(\varepsilon)$ of the impurity (eq. 4.10) can be derived directly from the equations of motion of the Anderson model 4.1 (see [15] Chapter 5.2) and is universally valid even in the many-body case. $G_{dd}(\varepsilon)$ is the key quantity that describes the behaviour of our system.

$G_{dd}(\varepsilon)$ in various parameter regimes

In contrast to the non-interacting case discussed above the d-orbital Green function for $U \neq 0$ reveals a rich structure that depends on the temperature and the parameter regime of the system. Its calculation requires elaborate many-body techniques [15, 17]. Here we shortly summarize the general behaviour.

If $\mu - \epsilon_d \gg \Delta$ and $\epsilon_d + U - \mu \gg \Delta$ the d-orbital is single occupied $\langle n_d \rangle = 1$ and charge fluctuations are suppressed ("*local moment*" regime). $\varrho_d(\varepsilon)$ within this parameter regime is depicted in Figure 4.3 for different temperatures. For temperatures below the Kondo temperature a sharp peak, the Kondo resonance or Abrikosov-Suhl [16] resonance gets superimposed to the d-electrons spectral function at energy ϵ_K near the chemical potential. As charge transport is dominated by quasi-particles near

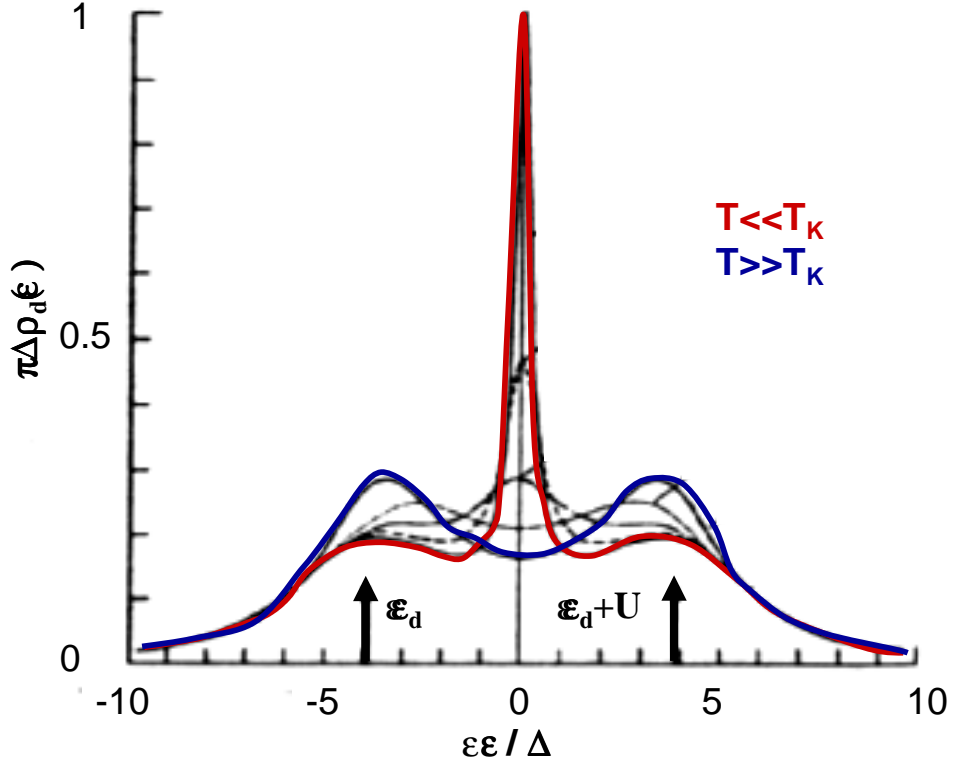


Figure 4.3: *d*-orbital spectral function for the symmetric Anderson model at different temperatures: for $T \ll T_K$ (red curve) a sharp many-body resonance is present at $\varepsilon = 0$, which vanishes above the Kondo temperature (blue curve). Figure reproduced from [62].

the chemical potential [17] and the strength of the impurity scattering is associated with $|V|^2 G_{dd}(\varepsilon)$, the building up of this resonance for low temperatures explains the increase of electrical resistivity that was mentioned in the introduction.

Below and above the chemical potential at energies $\bar{\varepsilon}_d$ and $\overline{\varepsilon_d + U}$ broad resonances of width Δ can be observed, which are termed lower and upper Hubbard band. They correspond to charge excitations where n_d is decreased/increased by one electron.

The Kondo resonance is centered at an energy ε_K , whose position depends on the filling of the orbital, i.e. on the ratio between the number $\langle n_d \rangle$ of electrons in the localized orbital and its degeneracy N_d . This can be derived from the Friedel sum rule (see Hewson [15], chapter 5.3)

$$\frac{\langle n_d \rangle}{N_d} = \frac{1}{2} - \frac{1}{\pi} \tan^{-1} \left(\frac{\varepsilon_K}{k_B T_K} \right) \quad (4.13)$$

In the case of particle-hole symmetry, which implies $\langle n_d \rangle = N_d/2$, the Kondo resonance lies directly at the Fermi energy. For impurities having less than half filled d- or f-shells (e.g. cerium) the Kondo resonance is above ϵ_F . For impurities with an occupation $\langle n_d \rangle > N_d/2$ (e.g. cobalt), the position of the resonance is below the Fermi energy. It has to be considered that the actual degeneracy N_d including possible modifications due to spin-orbit or crystal-field splittings is important.

In the local moment regime *Ujsaghy et al* [27] proposed to model the d-electrons Green function as a sum over three Lorentzians¹:

$$G_{dd}(\varepsilon) = \frac{Z_d}{\varepsilon - \bar{\epsilon}_d + i\Delta} + \frac{Z_U}{\varepsilon - \bar{\epsilon}_d - \bar{U} + i\Delta} + \frac{Z_K}{\varepsilon - \epsilon_K + ik_B T_K} \quad (4.14)$$

In the above formula Z_d , Z_U and Z_K are quasi-particle renormalization factors describing the spectral weight of each of the three resonances. It can be seen in Figure 4.3 that spectral weight gets transferred from the Hubbard bands to the Kondo resonance if the temperature is decreased. For $T \ll T_K$ the Kondo resonance reaches the unitary limit resulting in $Z_K \leq \pi k_B T_K / \Delta$ [63]. For $\varepsilon = \epsilon_K$ and deep within the Kondo regime this gives $t_{imp}(\epsilon_K) = -i/(\pi\rho_0)$, meaning unitary scattering. In the above 1D-example this would result in a complete depletion of spectral electron density at $x = 0$ and $\varepsilon = \epsilon_K$.

The behaviour in parameter regimes different from the Kondo regime is approximately sketched in Figure 4.4. The single particle spectral density $\varrho_d(\varepsilon)$ describes the probability that system changes its total energy by a certain amount ε if a *single electron* is added to the impurities d-orbital or removed from it. If the d-orbital is *double occupied* such *single-particle* processes will only result in a single occupied orbital. Therefore the spectral weight of the lower Hubbard band is strongly reduced resulting in $Z_d \rightarrow 0$. The situation in the *empty orbital*-regime is the opposite and suppresses the spectral weight of the upper Hubbard band $Z_U \rightarrow 0$. In the *mixed valence regime* a Hubbard band crosses the Fermi level resulting in non-integer occupation numbers n_d . Here the decomposition of $G_{dd}(\varepsilon)$ into three separate quasi-particle resonances is no longer possible. Hence, the spectral densities of the *mixed valence regime* plotted in Figure 4.4 are unrealistic [64, 65].

Reason for the Kondo resonance

The Kondo resonance appears in $\varrho_d(\varepsilon)$ only if the d-orbital is neither completely empty nor fully occupied. In this regime the impurity has an *internal degree of*

¹here we changed the sign of the imaginary part in the denominators compared to Ref. [27] in order to maintain the retarded representation of G_{dd} used throughout this text.

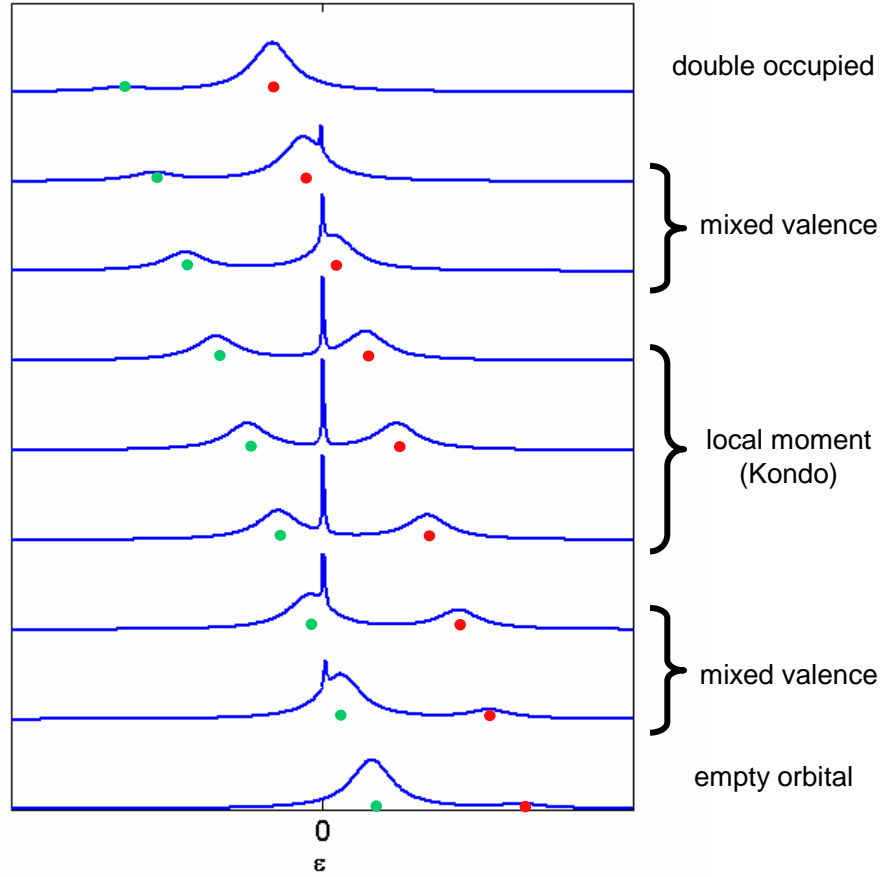


Figure 4.4: *Estimated sketch of the d-orbital spectral function in various parameter regimes: green dots represent ϵ_d while red dots correspond to $\epsilon_d + U$. Please note that the plotted line shapes in the mixed valence regime are unrealistic.*

freedom - there exist scattering processes that change the internal quantum numbers of the impurity without changing the total energy. In the above example the degree of freedom was the spin of the electron in the localized orbital; the peak near μ is associated with *spin fluctuations*. In general this degree of freedom can also be connected with an *orbital degeneracy* ("orbital Kondo Effect").

We keep in mind that - if we know the conduction band propagator $G_0(\mathbf{x}, \mathbf{x}', \epsilon)$ of the unperturbed host - the system is completely characterized by one complex scalar function of energy $t_{imp}(\epsilon)$ that depends on the spectral properties of the impurity. If equation 4.14 is valid and the Kondo resonance can be described by a Lorentzian, the surrounding LDOS would be modified in the identical way than in the case of a single-particle resonance. The only difference is that the spectroscopic features

arising from the Kondo resonance are always centered at an energy ϵ_K near the Fermi energy. We therefore expect a phase-shift of the LDOS-oscillations and Fano lines shapes at or near zero bias.

4.2.2 $\varrho(\mathbf{x}, \varepsilon)$ in Copper

In Chapter 3 the conduction electron propagator was calculated only for $\varepsilon = \epsilon_F$ in order to obtain the local density of states at the Fermi energy. To include the effects of dispersion the iso-energy surfaces $\Omega(\varepsilon)$ in the irreducible part of the first Brillouin zone were calculated for energies within $[-2.3\text{eV}, +4\text{eV}]$ i.e. within the entire 6th band of the copper band structure. From this $\text{Im}G_0^{VC}(x, d, h)$ and $\text{Im}G_0^{VV}(h)$ were obtained for one lateral coordinate x (along [010]) and different values of h and d by integration over $\Omega(\varepsilon)$. The real part was obtained using the Kramers-Kronig relation[47, 48]. From this one can calculate **spectrum sections** $\Delta\varrho(x, \varepsilon)/\varrho_0(\varepsilon)$ as well as **single spectra** in the same way as described in Chapter 3:

$$\frac{\Delta\varrho(\mathbf{x}_{\parallel}, \varepsilon)}{\varrho_0(\varepsilon)} = \frac{\text{Im} [G_0^{VC}(\mathbf{x}_{\parallel}, d, h, \varepsilon)^2 \cdot t_{imp}(\varepsilon)]}{\text{Im}G_0^{VV}(h, \varepsilon)} \quad (4.15)$$

We will later discuss a method how to extract this quantity $\Delta\varrho/\varrho_0$ from the experimental data. This will allow a direct comparison of STS-data and the calculations. Therefore this normalization will be used throughout the following.

The unknown quantity for the this purpose is the energy dependence of the t-matrix $t_{imp}(\varepsilon)$ that is connected with the dynamics of the impurity. Realistic spectral functions of Co and Fe impurities in copper are not accessible. Many-body techniques are usually based on highly idealized model-Hamiltonians and are valuable in showing the general behaviour in the different physical regimes. Their results depend on a number of parameters, whose particular values for our systems are unknown. *Ab-initio*-calculations in contrast are solely based on the atomic numbers, but they have up to now difficulties in treating electron correlations in a realistic way. Although DTF calculations of Co and Fe atoms in Cu are possible and give reasonable predictions of many physical properties [53], the Kondo resonance can not be reproduced by this technique. Currently efforts are being made in combining these two methods [66]. First-principles techniques could be used in obtaining the parameters of a given experimental system as $\varrho_0(\varepsilon)$, ϵ_d , V and approximately U . Thereafter state-of-the-art many-body calculations can be used to calculate the dynamics. In the following we will treat $t_{imp}(\varepsilon)$ of our systems as a well-defined but *unknown* quantity.

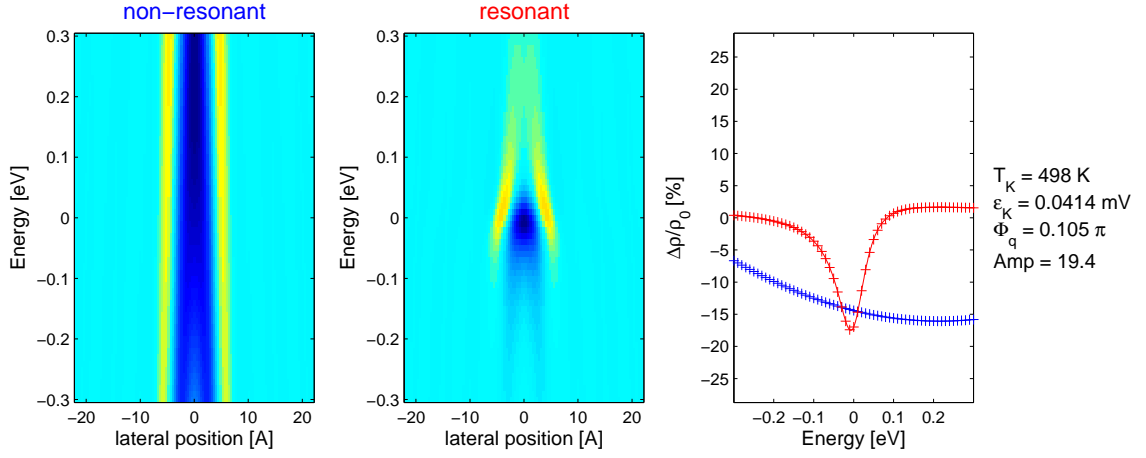


Figure 4.5: *calculated LDOS of a $d=3.3ML$ impurity in $h=7\text{\AA}$ above the surface*

The impact of $t_{imp}(\varepsilon)$ will now be discussed for two cases. In the first one the impurity scattering is energy-independent i.e. the phase of $t_{imp}(\varepsilon_F)$ at the Fermi energy obtained by the fitting the constant current topographies in Chapter 3 is used for all energies ε and the amplitude of $t_{imp}(\varepsilon)$ is fixed at $1/(\pi\rho_0)(\varepsilon)$ (unitary limit). This gives the reference, where all effects are due to dispersion and no scattering resonance is present. In the second case we use equation 4.14 to obtain a *hypothetical* t-matrix. For this we used guessed values of $\epsilon_d = -1V$, $\epsilon_K = 0V$, $U = 3V$, $\Delta = 100mV$ and $T_K = 500K$. This shows the behaviour if the scattering is purely due to the interaction with the localized orbital $|d\rangle$, if the ($N_d = 2$)-Anderson model is suitable for describing a "real" Co or Fe atom and if no additional scattering channels are present. Possible "background"-scattering could be due to a local strain field or a hybridization with the impurity's s-orbital [67].

We will always consider LDOS-sections with the spatial coordinate in $[010]$ direction and a single spectrum which is calculated directly above the impurity atom (i.e. at position $\mathbf{x}_{\parallel} = \mathbf{0}$). Both quantities are both normalized to $\Delta\rho/\rho_0$. As was already mentioned, the experiments described later will also give access to the quantity $\Delta\rho/\rho_0$. Thus the calculated spectra sections correspond to the experiment in which the STM tip is scanned along a line in $[010]$ -direction at a distance of h above the surface centrally through the interference pattern produced by an impurity in a depth d below the surface. The single spectrum will correspond to the (normalized) tunnelling spectrum taken in the middle of the defect pattern. Here blue curves correspond to the measured STS-data for the non-resonant case while red curves show the single spectra that are obtained using the hypothetical resonant t-matrix. Modified Fano functions described in eq. 4.8 (which use the "q-phase" Φ_q instead of the q-parameter q) are fitted to the single spectrum for the resonant case as this will

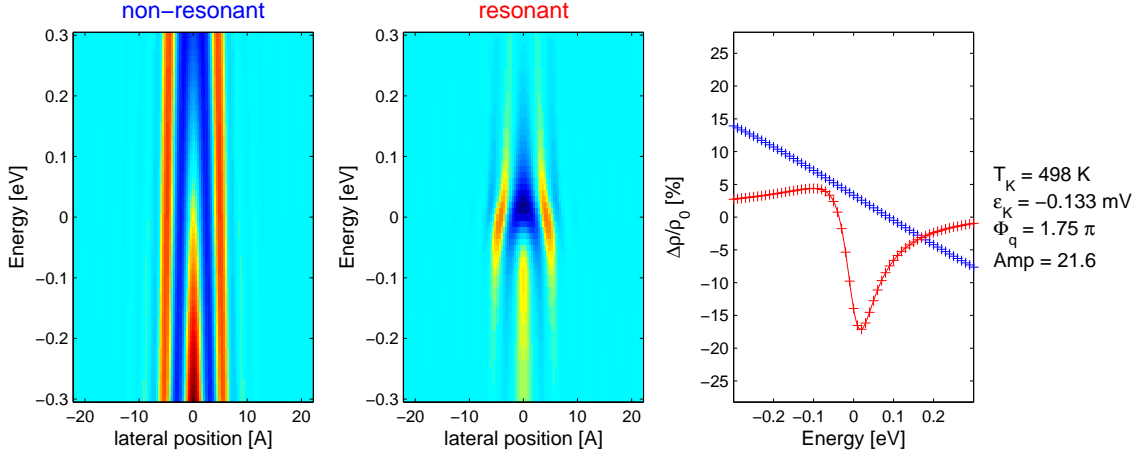


Figure 4.6: *calculated LDOS of a $d=3.3ML$ impurity in $h=3\text{\AA}$ above the surface*

also be later performed to the experimental data. This should help to analyze how the depth d of the impurity and the tip-sample distance h influence the resulting line shapes and the obtained fitting results.

We start with a 3rd layer impurity ($d=3.3ML$) probed at 7\AA above the surface. On the left of Figure 4.5 side the non-resonant case using a constant phase-shift of 1.1π is shown. Here no significant changes in the LDOS can be observed and the broad minimum that was visible in the constant current topographies of 3rd layer Co atoms (see Chapter 3) is present for all energies within $\pm 300mV$. The single spectrum of the non-resonant case shows a $-5\% \dots -15\%$ depletion of LDOS directly above the impurity. In contrast, the resonant case shows a full π -phase shift around zero bias in the spectrum section. The LDOS far above $\varepsilon = 0$ is approximately inverted compared with the LDOS for $\varepsilon \ll 0$. The amplitude of the oscillations becomes weaker the further the energy ε is chosen away from the resonance at ε_K . A clear anti-resonance can be observed in the single-spectrum and the Fano-fit nearly perfectly reproduces the Kondo temperature of $500K$ inserted into the t-matrix.

As discussed in chapter 3 the parameter h combining the tip-sample distance and the "sharpness" of the tip has a strong influence on the observed topographies. It was demonstrated in Figure 3.15 that a 3rd layer Co atom is imaged under mediocre tip conditions as a broad minimum in topography near zero bias while with tips permitting atomic resolution a central maximum can be observed. Whether a minimum or a local maximum is observed in the topographies directly depends on the electron's average phase-relation between the position of the impurity and the position of the tip. Therefore this effect does also play an essential role in the obtained LDOS-spectra. This can be seen in figure 4.6, where the 3rd layer impurity of figure 4.5 is

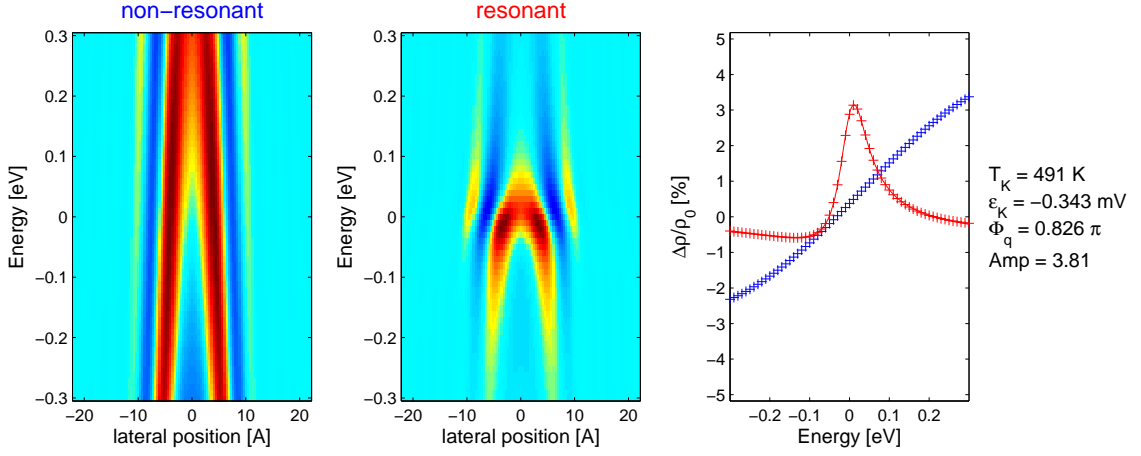


Figure 4.7: *calculated LDOS of a $d=6.3ML$ impurity in $h=7\text{\AA}$ above the surface*

probed in 3\AA distance. The measured Kondo temperature obtained by fitting the Fano-function is insensitive to this effect and reproduces the "correct" value. The line shape however and hence the q -phase differs from the results obtained in 7\AA distance. From this one can conclude that the line-shape and the amplitude of LDOS modulation are sensitive to the prevailing tip-condition and may differ between measurements using different tips. Probing the vacuum LDOS in larger distances from the surface will result in increased q -phases in the spectral line-shapes. This can be easily understood if we remember that moving the tip away from the surface suppresses the contribution of high \mathbf{k}_{\parallel} states to the tunnelling current. In the case of a spherical or nearly-spherical Fermi surface these high \mathbf{k}_{\parallel} states have a low perpendicular wave-vector component k_{\perp} . As the q -phase at a position directly above the impurity (i.e. with $\mathbf{x}_{\parallel} = \mathbf{0}$) is directly proportional to the perpendicular wave-vector component and to the distance between impurity and surface, an increased value of h results in a higher average k_{\perp} -value of the contributing electrons and hence in a higher q -phase. Thus we cannot expect that all experimental data performed on a certain impurity species in a certain depths below the surface will show the identical line shapes.

We now want to analyze which behaviour is expected if the impurity is placed at larger distances below the surface. While the non-resonant case did not show a significant bias dependence for the 3rd layer defects an impurity in 6 ML depths shows (Fig. 4.7) a significant slope of the phase fronts within $\pm 300mV$ causing nearly an inversion of the interference pattern from $-300mV$ to $+300mV$ even without a scattering resonance. Anyhow, this crossover happens continuously over the full energy range and the single spectrum still shows a monotonous behaviour. It is clearly discriminable from the resonant case which now shows a peak like resonance

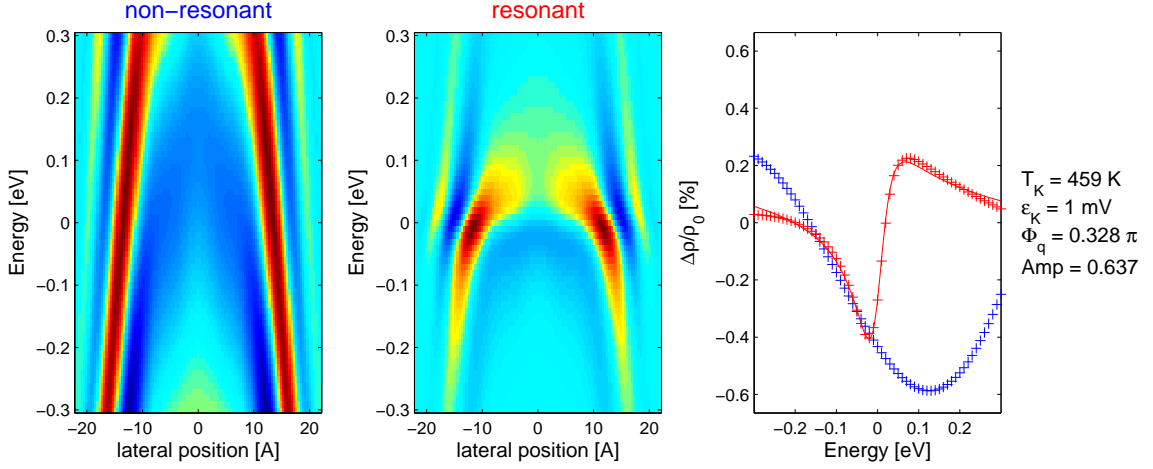


Figure 4.8: calculated LDOS of a $d=14.3ML$ impurity in $h=7\text{\AA}$ above the surface

with a q -phase close to π .

The spectrum sections calculated for the 14th layer impurity show that in the non-resonant case the bare dispersion already causes a shift of the phase fronts at the surface of more than half a wavelength i.e. the maxima and minima move significantly towards the center of the LDOS pattern even without a Kondo resonance. This could be misinterpreted as a phase shift of π . The single spectrum shows an oscillatory energy dependence for the non-resonant case which could be mixed up with a broad resonance. However, the lineshape of the resonant case is clearly distinguishable but the fitted Fano-function reveals a lower Kondo temperature than the one entered into the model t -matrix. The additional oscillations in the single spectra that are caused by the dispersion, constrict the observed resonance. This leads to an underestimation of the Kondo temperature if only the single spectrum is regarded. A similar behaviour was observed in the 1D example. Here the spectra in Fig.4.2f) shows an anti-resonance that appears much narrower than the one directly at the position of the impurity (Fig.4.2a).

As we have seen the impact of the dispersion becomes stronger for defects buried deeper below the surface. This is obvious: if the dispersion causes a change in the wavelength of $\Delta\lambda$ the n -th wavefront will be shifted by an amount $n \cdot \Delta\lambda$. Thus the shift of maxima and minima due to the dispersion increases linearly with distance:

$$\frac{dr}{d\varepsilon} = \frac{r}{k_F v_{Gr}} \quad (4.16)$$

In contrast to this the phase-shift due to a scattering resonance shows an arc tangent behaviour versus energy and has the steepest slope in the middle of the resonance

corresponding to a $\lambda/2$ shift within $\pi k_B T_K$. This $\lambda/2$ shift occurs at all distances from the impurity and corresponds to a "movement" of the phase fronts due to Kondo resonance of:

$$\frac{dr}{d\varepsilon} = \frac{1}{2k_F k_B T_K} \quad (4.17)$$

It becomes more difficult to distinguish between both effects the more the distance to the impurity is increased. This was already observed in the one-dimensional example (Fig. 4.2). The dispersion and the resonant phase-shift have comparable impact on the LDOS in a critical distance r_c :

$$r_c = \frac{v_{Gr}}{2k_B T_K} \equiv 0.5\xi_K \quad (4.18)$$

The quantity ξ_K is the Kondo coherence length [15, 68, 69, 70]. It is a length scale that also describes spatial decay of correlation between the spins of impurity and the conduction band electrons and thus the extension of the *Kondo screening cloud*. We should note that any ordinary single-particle resonance of identical width and energetic position has the *same impact* on the single-particle spectral density as the Kondo resonance.

In the case of copper as the host metal the mean Fermi velocity, as obtained from the LCAO calculations (see Appendix A), is $\approx 7.5eV \cdot \text{\AA}$. Thus an impurity having a Kondo temperature of $T_K = 500K$ can be clearly distinguished from a non-resonant point scatterer up to a depth of $r_c=48$ ML. From the opposite point of view it can be derived that the Kondo Effect of a 16th-layer impurity can be identified unless the Kondo temperature exceeds 1500 K. A 3rd layer impurity may have an Kondo temperature up to 8100 K without masking the resonance by dispersive effects.

After showing that $\varrho(\mathbf{x}, \varepsilon)$ is indeed modified by the Kondo Effect we want to discuss now, how these physical quantities can be extracted from an STM-experiment. After that we will show experimental data and check whether all calculated effects can be also observed in "reality" .

4.3 Scanning Tunnelling Spectroscopy

Up to now the interpretation of the STM-topographies was based on the theory of Tersoff and Harmann [35, 37], which states that for low bias voltages and low temperatures the tunnelling current I is proportional to the local density of states at the Fermi energy ε_F . In the following we will maintain the assumption of low

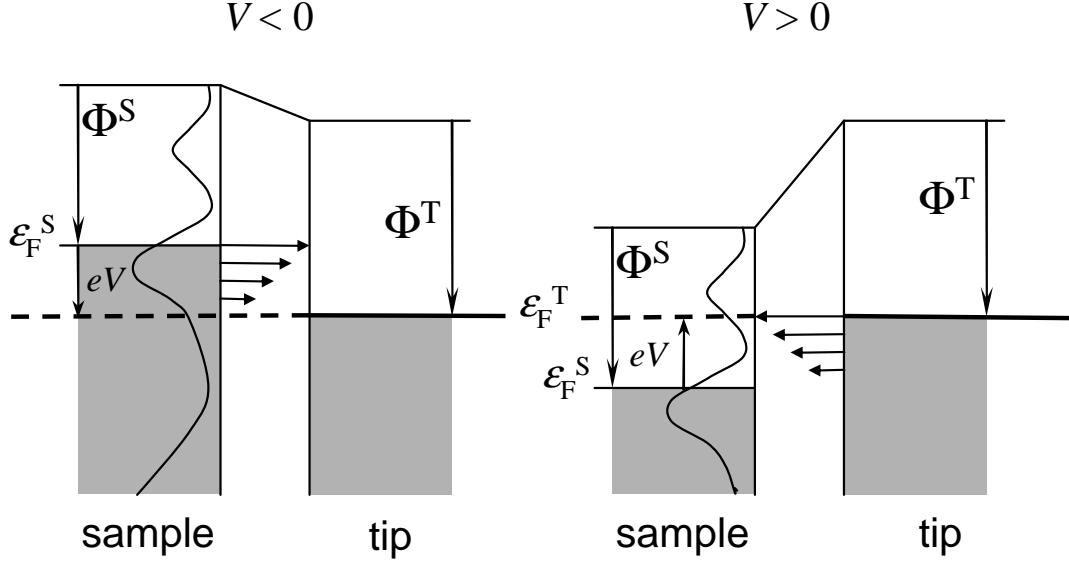


Figure 4.9: Schematic representation of the tunnelling junction at different bias voltages. The energy dependence of the transmission factor T is indicated by arrows of different length

temperatures but regard the situation at variable bias voltages V . This will give us access to *spectroscopic information*.

If a finite bias voltage V is applied to the tunnelling junction, the Fermi levels of tip and sample are shifted relatively by an amount eV as it is depicted in Figure 4.9. In the experiment V is applied to the sample while the tip is virtually grounded by an I/V converter. The tunnelling current I is the result of a spatial overlap between occupied states of one electrode and empty states of the other electrode. Using a set of sample states $|\mu\rangle$ with energies ϵ_μ and tip states $|\nu\rangle$ with energies ϵ_ν one obtains:

$$I(V) = \frac{4\pi e}{\hbar} \sum_{\mu\nu} \left[f(\epsilon_\nu - \epsilon_F^{(T)}) - f(\epsilon_\mu - \epsilon_F^{(S)}) \right] |M_{\mu\nu}|^2 \delta(\epsilon_\mu - \epsilon_\nu - eV) \quad (4.19)$$

where $f(\epsilon)$ are the Fermi-Dirac distributions and $M_{\mu\nu}$ is the tunnelling matrix element that was already defined in Chapter 2. The difference of the Fermi distributions of tip and sample defines an energetic window of states, which contribute to the tunnelling current. For low temperatures the Fermi functions can be replaced by step functions so that the above equation can be transformed into an integral containing

only transitions within a finite energy range between ϵ_F and $\epsilon_F + eV$:

$$I(V, \mathbf{x}_{\parallel}) \propto \int_{\epsilon_F}^{\epsilon_F + eV} d\varepsilon \varrho(\mathbf{x}_{\parallel}, \varepsilon) \varrho_T(\varepsilon - eV) T(\varepsilon, V, h(\mathbf{x}_{\parallel})) \quad (4.20)$$

here $\varrho(\mathbf{x}_{\parallel}, \varepsilon)$ and $\varrho_T(\varepsilon)$ are the local density of states of sample and tip, respectively. T is an energy- and bias-dependent transmission factor that can be related to an effective barrier height $\Phi_{eff} = 0.5 \cdot [(\Phi_S - eV) + \Phi_T]$ using the WKB approximation [34]:

$$T(\varepsilon, V, h) = \exp\left(\frac{-2h\sqrt{2m}}{\hbar} \sqrt{\frac{\Phi_T + \Phi_S + eV}{2} - \varepsilon}\right) \quad (4.21)$$

where Φ_T and Φ_S denote the work functions of tip and sample and h is the tip-sample distance.

4.3.1 Multi bias spectroscopy

If the tip-sample distance is adjusted in order to keep the tunnelling current constant at every scan point \mathbf{x}_{\parallel} , the corresponding topography $h(\mathbf{x}_{\parallel})$ is a function, which leaves integral 4.20 invariant. If the work function of the sample is laterally constant, the only \mathbf{x}_{\parallel} dependent term is the sample LDOS $\varrho(\mathbf{x}_{\parallel}, \varepsilon)$. Therefore this measurement provides contours on which the integrated LDOS within ϵ_F and $\epsilon_F + eV_T$ is constant. The energy dependent weighting factor within this integral is the tip DOS $\varrho_T(\varepsilon)$ and the transmissivity T , so that states of different energy may contribute differently to the tunnelling current and hence may differently influence the topography $h(\mathbf{x}_{\parallel})$. If the variations of $\varrho_T(\varepsilon)$ and $T(h, V, \varepsilon)$ are negligible within ϵ_F and $\epsilon_F + eV_T$, the obtained contours are proportional to the *average LDOS* in this energetic interval.

In *multi-bias mode*, every scan line is scanned n -times using different tunnelling parameters $(V_T^{(n)}, I_T^{(n)})$ before proceeding to the subsequent scan line. This allows a pixel-by-pixel comparison of the obtained contours $h^{(n)}(\mathbf{x}_{\parallel})$.

4.3.2 I(V) - spectroscopy

In this spectroscopy mode the tip scans the surface in constant current mode at a given set of tunnelling parameters (V_T, I_T) . At every scan point the feedback loop is temporarily deactivated, holding the tip in a fixed distance to the sample, and a

$I(V)$ spectrum is recorded within a certain voltage range. After that, the feedback loop is switched on again and the tip is moved to the subsequent scan point. This measurement records a three dimensional data set $I(V, \mathbf{x}_{\parallel})$ along with the constant current topography $h(\mathbf{x}_{\parallel})$.

The quantity, which is of primary physical interest, is the sample LDOS (or single particle spectral density) $\varrho(\mathbf{x}_{\parallel}, \varepsilon)$ at a certain lateral position \mathbf{x}_{\parallel} and a certain energy ε . This quantity can be approximately derived from the differential conductance $dI/dV(V)$ at a certain bias voltage V . Using Leibnitz's rule, the derivative of equation 4.20 with respect to the bias voltage gives three terms²:

$$\begin{aligned} \frac{dI}{dV}(V, \mathbf{x}_{\parallel}, h) &\propto \varrho(\mathbf{x}_{\parallel}, eV)\varrho_T(0)T(eV, V, h) \\ &+ \int_0^{eV} d\varepsilon \varrho(\mathbf{x}_{\parallel}, \varepsilon)\varrho_T(\varepsilon - eV)\frac{dT(\varepsilon, V, h)}{dV} \\ &+ \int_0^{eV} d\varepsilon \varrho(\mathbf{x}_{\parallel}, \varepsilon)\frac{d\varrho_T(\varepsilon - eV)}{dV}T(\varepsilon, V, h) \end{aligned} \quad (4.22)$$

If the spectroscopy is performed at voltages close to 0V the bias dependence of the transmission factor T can be neglected. If furthermore the tip LDOS $\varrho_t(\varepsilon)$ is assumed to be structureless the latter two terms in eq. 4.22 are zero and one obtains a handy expression:

$$\frac{dI}{dV}(V, \mathbf{x}_{\parallel}, h) \propto \varrho(\mathbf{x}_{\parallel}, eV)\varrho_T(0)T(eV, V, h) \quad (4.23)$$

Within this approximation, the differential conductance still depends on the unknown tip LDOS at the Fermi energy and the transmission factor T of the tunnelling junction at the chosen tunnelling parameters (V_T, I_T) . In other words, spectroscopies performed with the tip closer to the sample show in general higher values of dI/dV than spectra obtained at larger distances. In order to allow a quantitative comparison of the STS data taken with different tips and at different tunnelling parameters, we again decompose the sample LDOS $\varrho(\mathbf{x}_{\parallel}, \varepsilon)$ in an unperturbed part $\varrho_0(\varepsilon)$ plus a local variation $\Delta\varrho(\mathbf{x}_{\parallel}, \varepsilon)$. We can then try to eliminate both $\varrho_T(\varepsilon)$ and $T(\varepsilon, V, h)$ by relating $I(V)$ to a reference spectrum $I_0(V)$ taken on the free surface, i.e. obtained in an area where $\Delta\varrho(\mathbf{x}_{\parallel}, \varepsilon) = 0$:

$$\frac{\frac{dI}{dV}(V) - \frac{dI_0}{dV}(V)}{\frac{dI_0}{dV}(V)} = \frac{\Delta\varrho(\mathbf{x}_{\parallel}, eV)\varrho_t(0)T(eV, V, h)}{\varrho_0(eV)\varrho_T(0)T(eV, V, h)} = \frac{\Delta\varrho(\mathbf{x}_{\parallel}, eV)}{\varrho_0(eV)} \quad (4.24)$$

²in the following we will measure the energy of tip and sample states relative to the corresponding Fermi energy $\epsilon_F^{(T)}$ and $\epsilon_F^{(S)}$, respectively.

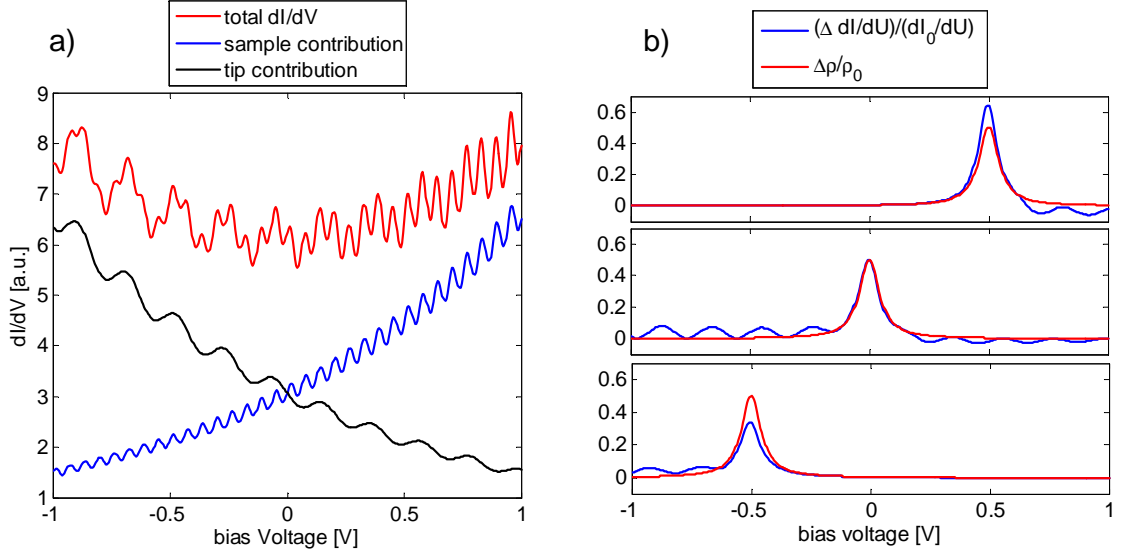


Figure 4.10: *a)* influence of tip and sample properties on the dI/dV spectrum. $\rho(\varepsilon)$ and $\rho_T(\varepsilon)$ have been "marked" with oscillations of different frequency. *b)* the normalization $(\Delta dI/dV)/(dI_0/dV)$ underestimates the strength of spectral features for negative bias voltages and vice versa.

The above expression is only valid, if both $I(V)$ and $I_0(V)$ are taken at identical tip-sample distance h so that the transmission factors can be cancelled down. This is in general not true since tip-sample distance is changed by the feedback loop above areas of modified LDOS in order to keep I constant. Since the topography $h(\mathbf{x}_{\parallel})$ is recorded simultaneously to the spectroscopy, the $I(V)$ curves can be normalized to a constant tip-sample distance h_0 afterwards. This procedure will be described in the next section.

It can directly be seen that equation 4.23 contains an unphysical asymmetry concerning a permutation of tip and sample. The differential conductance at a certain voltage V is related to the sample LDOS at the particular energy eV , the tip LDOS is only required at the Fermi level and T is monotonically increasing with bias voltage. If tip and sample were identical the dI/dV -spectrum has to be symmetrical around $V = 0V$. Obviously this is not satisfied by eq. 4.23. If the exponent of eq. 4.21 is replaced by approximation 3.20 (see Chapter 3), a more realistic expression for

dI/dV is obtained:

$$\begin{aligned} \frac{dI}{dV}(V) &= \frac{1}{2} [\varrho(eV)\varrho_T(0)T(eV, V, h) + \varrho(0)\varrho_T(-eV)T(-eV, -V, h)] \\ &+ \frac{1}{2} \int_0^{eV} d\varepsilon [\varrho'(\varepsilon)\varrho_T(\varepsilon - eV) - \varrho(\varepsilon)\varrho_T'(\varepsilon - eV)] T(\varepsilon, V, h) \end{aligned} \quad (4.25)$$

Here $\varrho'(\varepsilon)$ denote the derivatives of LDOS with respect to the energy. It can be seen that the $dI/dV(V)$ -spectrum is dominated by the tip DOS at negative bias voltages and by the sample LDOS at positive values of V . This behaviour can also be observed in Figure 4.10 a) where a dI/dV -spectrum has been calculated directly from equation 4.20 using $\Phi_T = \Phi_S = 4eV$ and $h = 6\text{\AA}$. For a better discrimination between tip and sample properties, 5%-modulations of different frequency have been added to the LDOS of tip and sample, respectively. The blue and black lines are the first and second terms of equation 4.25. This shows that in the strict sense the obtained identity $(\Delta dI/dU)/(dI_0/dU) = \Delta\varrho/\varrho_0$ is only valid at $V = 0$. This can be seen in figure 4.10 b). For negative bias voltages the normalization 4.24 underestimates the magnitude of spectroscopic features while for positive voltages the obtained values of $(\Delta dI/dU)/(dI_0/dU)$ are larger than the actual relative change of LDOS $\Delta\varrho/\varrho_0$. Additionally one can observe that spectroscopic features of the tip cannot be completely removed by this normalization. However, unless a better normalization is found, this is the best we can do.

The recorded spectroscopic information is a three dimensional data set and can be displayed in several ways:

1. **Single dI/dV -Spectra:** $dI/dV(V)|_{x_0, y_0}$ show the differential conductance versus bias voltage at one lateral position (x_0, y_0)
2. **dI/dV -Maps:** $dI/dV(x, y)|_{V_0}$ -Maps depict the spatial arrangement of differential conductance at a fixed bias voltage V_0 .
3. **Spectrum Sections:** $dI/dV(s, V)|_{x(s), y(s)}$ display the differential conductance versus bias and *one* spatial coordinate s along a line $(x(s), y(s))$.

Since the latter two compare spectroscopic information at different lateral positions, they are in general sensitive to artifacts, which are due to a local variation of tip-sample distance (*topography*). This in turn depends on the chosen tunnelling parameters (V_T, I_T) used for the constant-current feedback. As the elimination of these effects is important for the interpretation of some STS-data presented later, we will now discuss the origin of these artifacts.

4.3.3 STS normalization

If the tip is stabilized in constant current mode, the set-point current I_T is obtained at the chosen bias voltage V_T . Furthermore, if thermo voltages [71] across the tunnelling junction are neglected, the current I vanishes at $V = 0$. These two values $I(0, \mathbf{x}_{\parallel}) = 0$ and $I(V_T, \mathbf{x}_{\parallel}) = I_T$ are fixed throughout the data set, i.e. $\forall \mathbf{x}_{\parallel}$. If for example $\varrho(\mathbf{x}, \varepsilon)$ is modulated laterally but constant in energy within ϵ_F and $\epsilon_F + eV_T$, the local variations of the LDOS are fully compensated by the tip-sample distance. In this case, both the $I(V)$ -characteristic and $dI/dV(V)$ will *not* differ laterally within this energy range, although the sample-LDOS *is* laterally dependent. The spectroscopy is "blind" within a certain energy range due to a partial compensation of spectroscopic information by the non-constant tip-sample distance. If we drop the assumption of an energy-independent LDOS, the $I(V)$ -curves will vary from one position to another, but since $I(0)$ and $I(V_T)$ are fixed, the mean value of dI/dU will be constant within ϵ_F and $\epsilon_F + eV_T$ for all positions. Consequently the comparison of STS-data taken at different positions will *always* be afflicted with topographic artifacts.

An example is shown in Figure 4.11. Here the identical defect (a 5th layer Fe atom in Cu(100)) has been measured twice with the constant current feedback working at $V_T = +150mV$ and $V_T = -150mV$, respectively. The local variations of tip-sample distance in both measurements are depicted in Figure 4.11a,b and differ significantly for both values of V_T . In the **spectrum sections** (Fig. 4.11c,d), which are depicted below the topography cross-sections, the artifacts due to non-uniform tip-sample distances can be clearly seen. The $V_T = +150mV$ measurement contains spectroscopic information only for $U < 0$. The situation for $V_T = -150mV$ is the opposite.

The information contained in a **single dI/dV spectra** at a certain position is less sensitive to these effects. This can be seen in Figure 4.11 g). For both values of V_T single spectra are taken directly above the impurity at position (*), which corresponds to a vertical cross-section of the Spectrum section as indicated by a black line. Both spectra look similar but are shifted vertically by a certain amount. As the $V_T = +150mV$ data was achieved at a $\approx 2pm$ larger distance, it is obvious that the dI/dV values are smaller.

If the reference spectrum $I_0(V)$ was measured in distance h_0 the obtained normalized change of differential conductance is:

$$\frac{\Delta dI(V)/dV}{dI_0(V)/dV} = \frac{\Delta \varrho(\mathbf{x}_{\parallel}, eV)}{\varrho_0(eV)} \cdot \frac{T(eV, V, h)}{T(eV, V, h_0)} + \frac{T(eV, V, h)}{T(eV, V, h_0)} - 1 \quad (4.26)$$

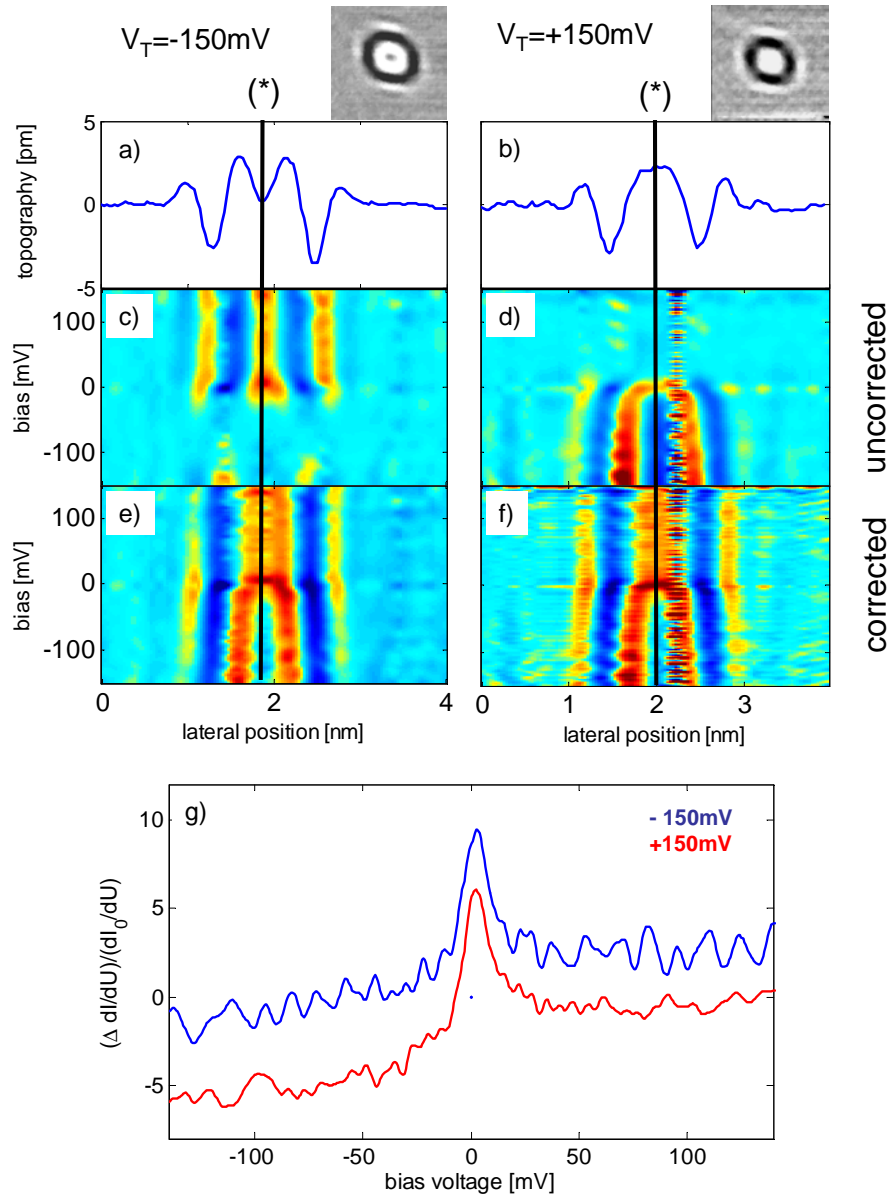


Figure 4.11: *The non-constant tip-sample distance due to the constant-current feedback complicates the lateral comparison of STS-data: a) and b) cross-sections of the STM-signature of 5th-layer Fe atoms at -150mV and $+150\text{mV}$ respectively. c), d) uncorrected spectra section are "blind" within an bias interval between 0V and V_T . e), f) artifacts can be successfully removed by proper normalization of the STS-data. g) uncorrected single spectra taken at position (*) differ only by a vertical offset*

Using a work function of 4.6eV a change in tip-sample distance of $h - h_0 = 2\text{pm}$ results in $T(0, 0, h)/T(0, 0, h_0) = 0.97$. Therefore the spectrum taken at $h = h_0 + 2\text{pm}$ is shifted vertically by -3%. Furthermore the amplitude spectroscopic features (e.g. the peak near 0V) is reduced to 97%, which is a less prominent effect. The general spectroscopic information (energetic position of peaks, line-widths, line-shapes) is identical in both cases and hence less sensitive to this effect. However, when interested in lateral dependence of differential conductance (**Spectrum sections**, **dI/dV-maps**) these artifacts have to be corrected.

For this purpose the STS-data were normalized to a constant tip-sample distance h_0 . This distance was defined as the average value of $h(\mathbf{x}_{\parallel})$ on the free surface, i.e. far away from the defect. I(V)-curves taken at distances closer to the surface have to be attenuated while spectra obtained at $h(\mathbf{x}_{\parallel}) > h_0$ need to be amplified. This was done using:

$$I(\mathbf{x}_{\parallel}, V)_{norm} = I(\mathbf{x}_{\parallel}, V) \cdot \exp(-2\kappa_0(h(\mathbf{x}_{\parallel}) - h_0)) \quad (4.27)$$

The important quantity for this purpose is the average work function of tip and sample. For this a value of $\Phi = 4.6\text{eV}$ turned out to be appropriate. The corrected spectrum sections are depicted in Figure 4.11 e,f).

For most of the data presented here, the measurement was performed twice with bias voltages V_T chosen symmetrically around 0V, i.e. a spectroscopy taken from -300mV to +300mV was measured twice with set-points at $V_T = -300\text{mV}$ and $V_T = +300\text{mV}$, respectively. This allowed cross-checking the efficiency of the topography normalization and to determine the work function needed in order to achieve agreement between both data sets.

4.4 Topographies at different bias voltages

We now want to proceed with the analysis of the experiments and investigate, whether the Kondo Effect can be observed in real space. Subsurface impurities of two different chemical elements have been prepared in this work, namely iron and cobalt. From numerous macroscopic experiments on large ensembles of Co and Fe impurities in copper, the Kondo temperatures of these systems are roughly known. They are summarized in [72] and are 5-50 K for Fe in Cu and 250-1000 K for cobalt impurities in copper. As the Kondo temperatures of both systems are different, the phase-shift observed in the calculations should occur in different energy intervals around 0V. This should be observable in the constant current topographies taken at different bias voltages.

Since states with energies within ϵ_F and $\epsilon_F + eV_T$ contribute to the tunnelling current I_T , the topography $h(\mathbf{x}_{\parallel})$ is a contour of constant *integrated LDOS*. The weighting of states in this integration depends on $\varrho_{Tip}(\epsilon)$ and the transmission factor T . Therefore, especially at higher bias voltages, a quantitative interpretation of these measurements is difficult and not as straightforward as that of the differential conductance. But the analysis provides indications of energy dependent effects: if there is a significant variation of $h(\mathbf{x}_{\parallel})$ in a certain bias voltage range, there also has to be a change of sample LDOS in the particular energy interval. It is the most quick and simple kind of STM-experiment to perform constant current topographies at different bias voltages.

Indeed striking differences between both impurity species can be observed concerning the bias dependence of the measured STM-patterns. Figures 4.12 and 4.13 show a direct comparison of 3rd layer cobalt and iron impurities at different bias voltages. The patterns induced by both species are in general similar concerning their lateral extension and their amplitude in tip-sample distance but they show significant differences in their energetic behaviour. In the depicted cross-sections the red lines correspond to the trace of the STM tip at positive bias voltages and the blue traces correspond to negative voltages. It has to be noted that the presented measurements of the cobalt atoms were taken at $\pm 300mV, \pm 200mV, \pm 100mV$ and $\pm 10mV$, while the depicted Fe data have been measured at bias voltages of $\pm 312mV, \pm 30mV, \pm 10mV$ and $\pm 3mV$.

In the case of cobalt impurities only minor changes in the topographies can be observed within $\pm 10mV$. In the identical energy range a significant effect can be observed for iron impurities. Here the size of the maximum in the center of the pattern is reduced. The interference pattern "shrinks" from negative to positive voltages and the wave-fronts observed at positive voltages are slightly shifted towards the center of the pattern compared with the data taken at negative bias voltages. This can be observed for Fe even within $\pm 3mV$ while for cobalt an effect of bias voltage can be seen only for $\pm 100mV$ and, more significantly, for $\pm 200mV$. The patterns induced by cobalt impurities develop into an minimum centrally above the impurity. In the case of iron atoms a tiny local maximum persists even for $+312mV$. It can be clearly seen that this crossover is more abruptly around zero bias for the Fe atoms.

It was shown that Fe and Co impurities differ strongly in their voltage dependent behaviour. In the case of iron significant effects can be observed within $\pm 10mV$ around zero bias. In such a small energy range, the band structure of copper can be assumed to be constant and the LCAO band structure calculation we used in Chapter 3 reveals changes of $|\mathbf{k}|$ in the order of (min: +0.06%, mean: +0.16% max: +0.23%). Thus the effect has to be related to a property of the impurity. The

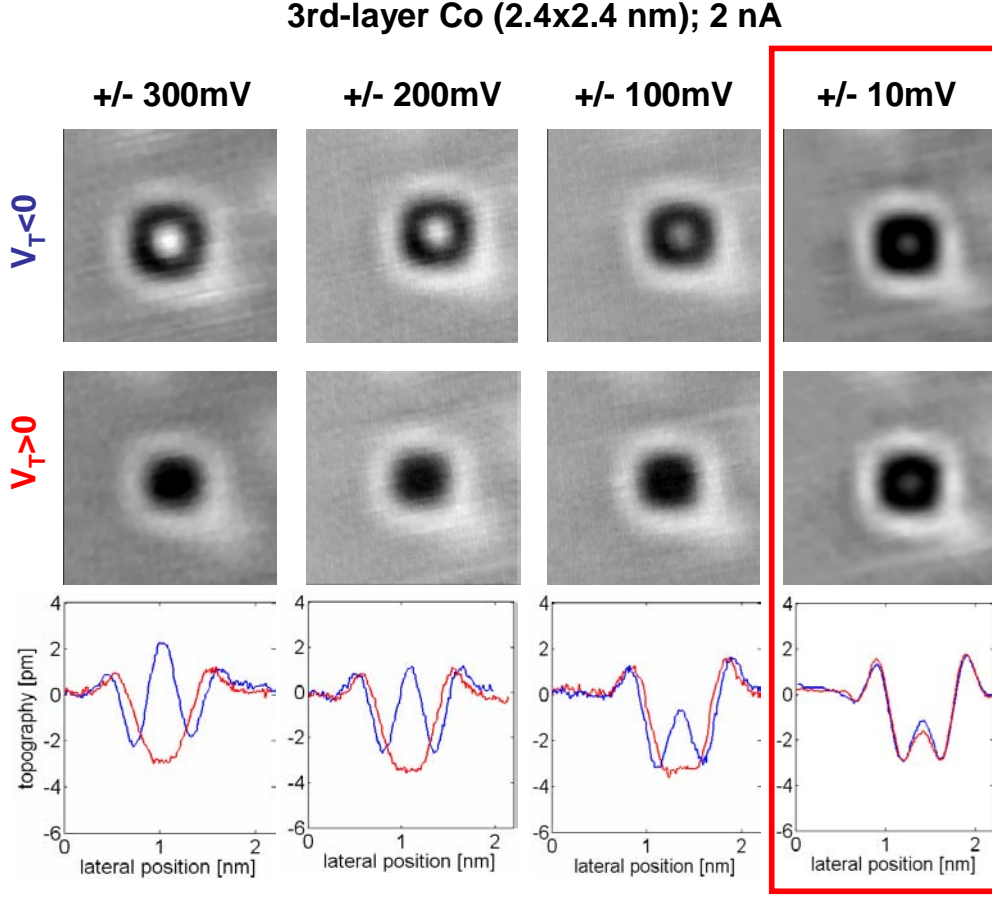


Figure 4.12: *Bias dependence of constant current topographies of Co impurities in the 3rd subsurface layer*

signatures arising from cobalt impurities show only minor variations within $\pm 10mV$ but here an effect can be seen between within $\pm 100mV$ which becomes more prominent within $\pm 200mV$. These energy ranges ($\pm 100mV$ and $\pm 200mV$) correspond to maximal changes in $|\mathbf{k}|$ of (min: +0.58%, mean: +1.7% max: +2.3%) and (min: +1.2%, mean: +3.4% max: +4.8%), respectively. This is an energy range where the band structure of copper does show significant modifications.

In accordance with the above estimation of a 0.2% change in the band structure of copper within $\pm 10mV$ we can assume the host Green-function to be constant $G_0(\mathbf{x}, \mathbf{x}', \epsilon_F - 10mV) = G_0(\mathbf{x}, \mathbf{x}', \epsilon_F + 10mV)$. In this case the maximum possible change in $\Delta\rho(\mathbf{x})$ is an inversion of the LDOS-pattern and corresponds to a change in the scattering phase-shift by π . We can thus use the Green function calculated at the Fermi energy and fit the measured topographies of the Fe impurities in the

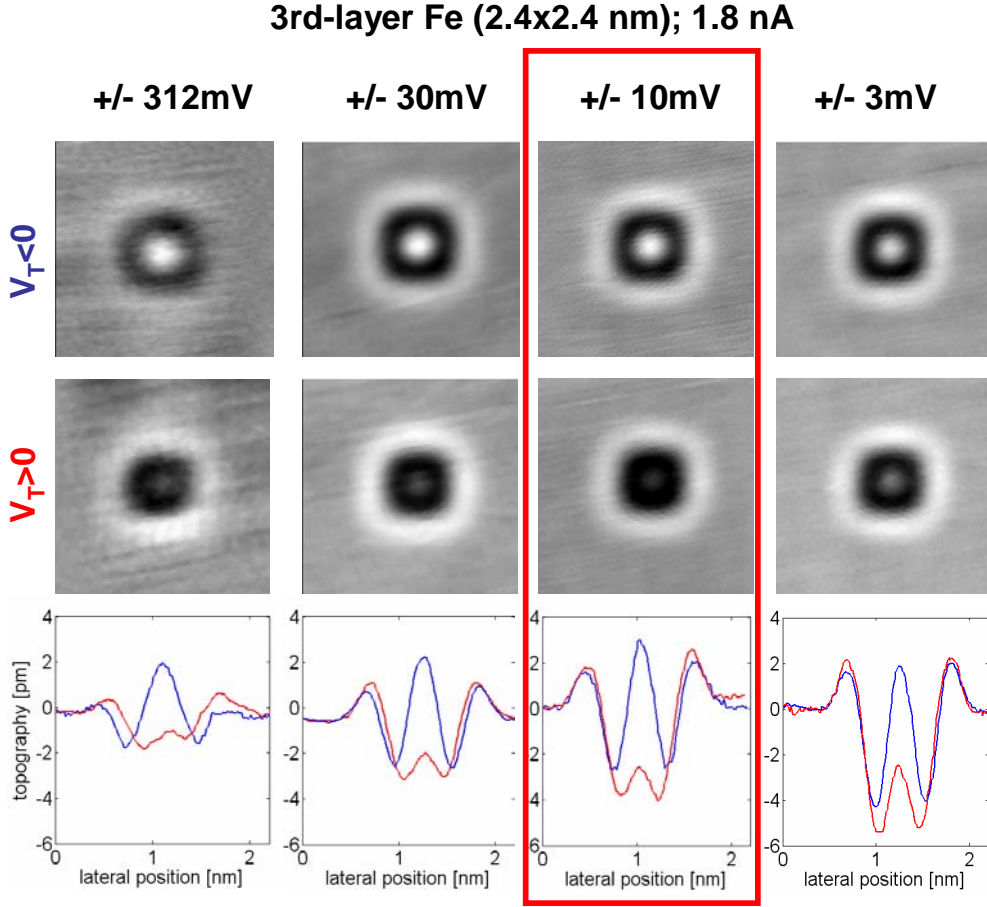


Figure 4.13: *Bias dependence of constant current topographies of Fe impurities in the 3rd subsurface layer. The effect within $\pm 10\text{mV}$ is much stronger than for the Co atoms.*

identical way as performed in Chapter 3. The result is shown in Figure 4.14 and reveals a change of the phase-shift of 0.25π within $\pm 30\text{mV}$ and of 0.15π even within $\pm 3\text{mV}$.

As stated before, the topographies at a certain bias voltage V_T cannot be interpreted as the LDOS of the sample at the particular energy but rather as the (tip-DOS weighted) average LDOS between ϵ_F and $\epsilon_F + eV_T$. Thus the changes in the sample LDOS that are responsible for the observed effects have to be even larger than those observed in the topographies. The fitting of the topographies reveal a (weighted) average value of $t_{imp}(\epsilon)$ within ϵ_F and $\epsilon_F + eV_T$. As a phase-shift of 0.25π can be already observed in the constant current topographies this indicates that the phase-shift of $\varrho(\mathbf{x}, \epsilon)$ around zero bias has to be larger than 0.25π . Consequently, for the

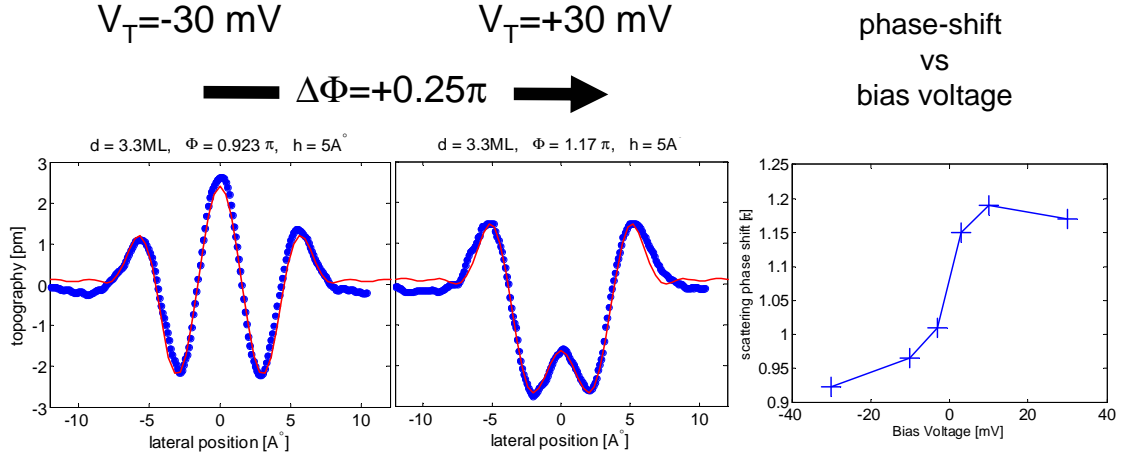


Figure 4.14: Calculations of LDOS at ε_F (red curves) fitted to the constant current topographies of 3rd layer Fe atoms (blue markers) at different bias voltages. The scattering phase-shift changes by 0.25π within $\pm 30\text{mV}$.

case of Fe the observed effects cannot be due to dispersion but have to be due to a change in the "scattering behaviour" $t_{imp}(\varepsilon)$ of the impurity.

This significantly different voltage dependence of both species can be also observed for different depths of the impurity below the surface. In order to show that, we now briefly compare the topographies of impurities in the layers 4-6 only for bias voltages of $\pm 10\text{mV}$ and $\pm 100\text{mV}$.

For the 4th-layer (Fig. 4.15) atoms the height and the lateral extension of the local maximum centrally above the impurity is reduced. As a local maximum stays a local maximum, the effect is less obvious in the grey-scale coded STM-topographies than it was the case for the 3rd-layer impurities. The cross-sections however show that the STM-traces taken at positive voltages (red curves) are shifted inwards compared to those obtained at negative voltages (blue curves). This can be clearly seen for $\pm 10\text{mV}$ for Fe impurities while subsurface Co atoms do not produce any significant effects within this energetic interval.

The 5th layer impurities (Fig. 4.16) show a more prominent effect, since a local minimum being present in the center of the interference pattern for negative bias voltages develops into a plateau-like maximum that (depending on the tip-quality) may still possess a slight central dimple. Thus, similar to the 3rd-layer impurities, the different bias dependency of both impurity species can be already identified during the STM-measurements without the necessity of a detailed comparison of cross-sections.

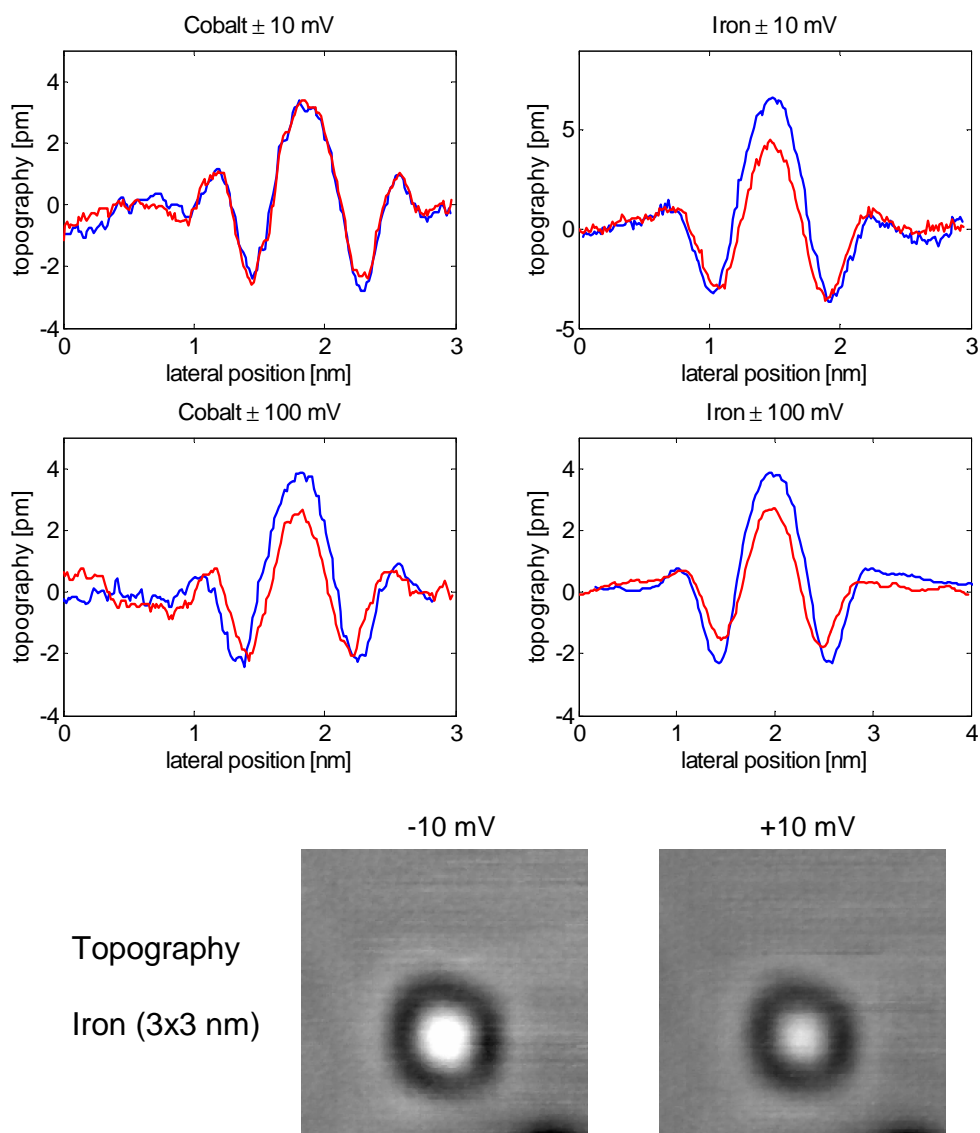


Figure 4.15: Comparison of the bias dependence of Co and Fe impurities in the 4th subsurface layer. The Fe impurities show a phase-shift within ± 10 mV.

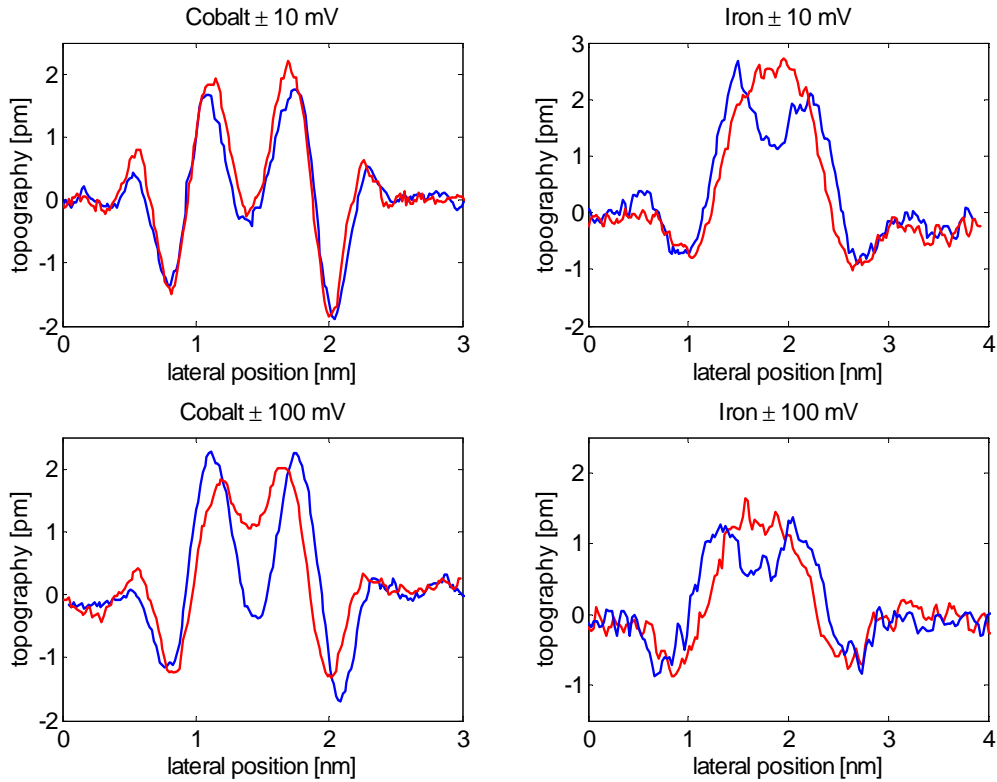


Figure 4.16: Comparison of the bias dependence of Co and Fe impurities in the 5th subsurface layer. For Fe a local minimum turns into a local maximum within $\pm 10\text{mV}$.

If cobalt or iron impurities are buried in the 6th subsurface layer (Fig. 4.17) the resulting STM-patterns are ring-like enhancements of LDOS. The diameter of these rings is reduced if the bias voltage is raised above 0V . The same reduction applies to the depth and lateral extension of the local minimum in the center of the STM pattern. This different behaviour of Co and Fe was consistently observed on multiple prepared samples using different STM-tips. Thus it seems to be a genuine property of the particular impurity species.

For the correct interpretation of the presented data and the conclusion that the observed effects are due to an energy dependence of the sample's LDOS we have to exclude one mechanism that can also cause differences in the STM-topographies of subsurface impurities. This was discussed in Section 3.4.4 when the impact of the tunnelling resistance on the measured patterns was discussed. Different bias voltages as applied here result in different tunnelling resistances and hence in different tip-sample distances h . As the obtained interference patterns depend on the tip-sample

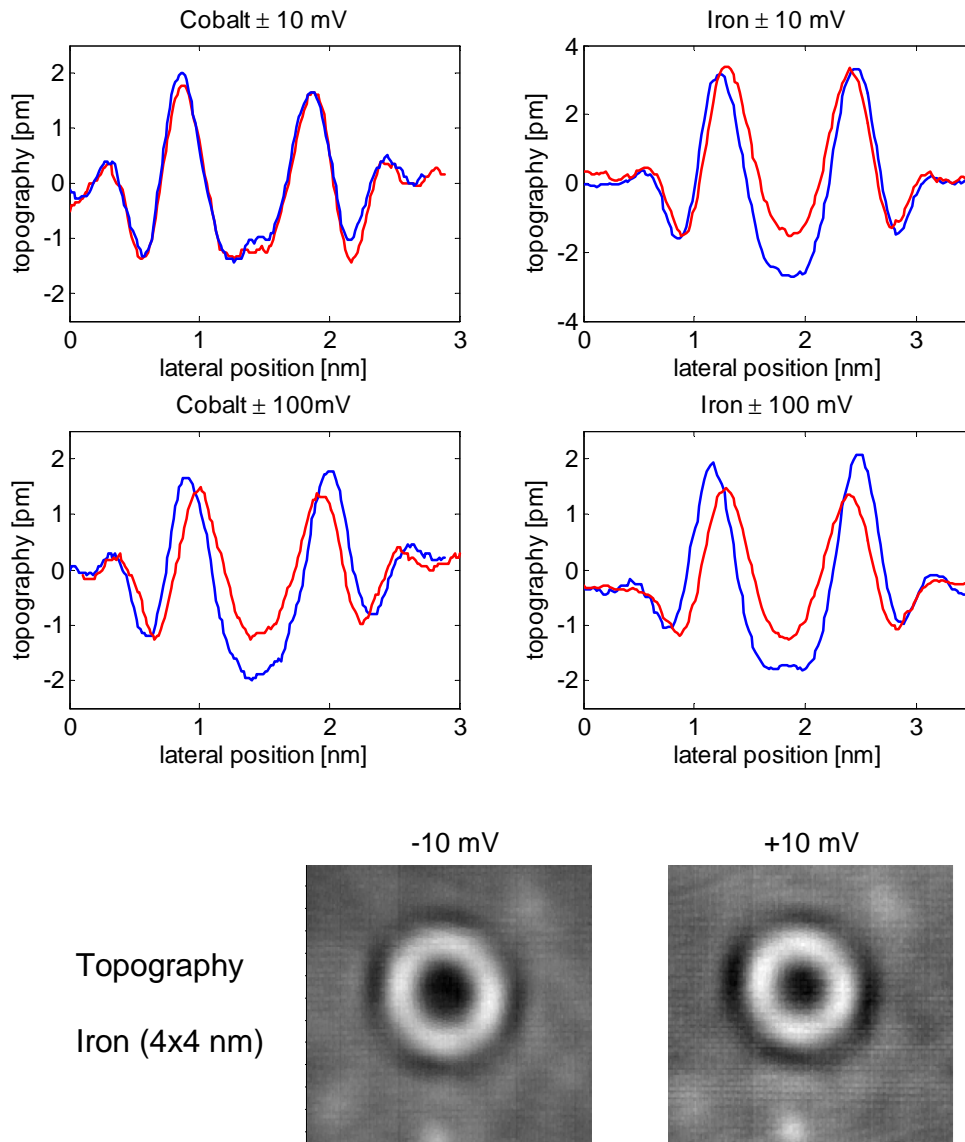


Figure 4.17: Comparison of the bias dependence of Co and Fe impurities in the 6th subsurface layer. Again a significant difference between both impurity species can be observed.

distance, it has to be assured that the topographies discussed above were taken in comparable distance from the sample. The necessary information for that purpose is contained in the experimental data since the topographies for all tunnelling parameters were recorded simultaneously and the relative tip-sample distances can be extracted. This analysis reveals that the measurements at the identical absolute bias voltage but with different polarities (e.g. $+10mV$ and $-10mV$) were always taken in nearly identical tip-sample distance and showed a Δh of less than $4pm$. In contrast to that, the STM-measurements at $V_T = \pm 10mV$ are taken in $\approx 1\text{\AA}$ smaller distance to the sample than those performed at $V_T = \pm 100mV$. Thus the impact of different tip-sample distances on the topographies might be a problem for the comparison of data taken at $+10mV$ and $+100mV$. However, if a difference in the topographies is observed between $+10mV$ and $-10mV$ or between $+100mV$ and $-100mV$ is, this can be clearly attributed to an energy dependence of the sample's LDOS.

It can already be excluded that the bulk-dispersion is solely responsible for the observed energy dependence. If that were the case both impurity species (Co, Fe) would show an identical behaviour. In addition we saw from the calculations that the dispersion in copper is negligible within $\pm 10mV$ and cannot explain the drastic changes observed on the iron impurities. The changes observed on the cobalt impurities however occur within a larger energy range. From the topographies and the LDOS calculations it is not clear whether these changes are due to the dispersion or due to an energy dependent scattering behaviour of the impurity. In order to reveal this question, we now proceed with the STS-analysis of the experimental system. As we saw in the calculations, a scattering resonance is also characterized by Fano line shapes in the dI/dV curves.

4.5 STS of subsurface impurities

The constant current topographies described in the previous section indicated strong energy dependent effects near zero bias for the Fe impurities. Thus we will start the description of the STS-data on this impurity species. After that the sub-surface cobalt atoms will be discussed. First of all this will be performed from a purely experimental point of view. The analysis will focus on the position, widths, asymmetry and amplitude of the Kondo resonance in the dI/dV -curves. This analysis is relatively insensitive to the artifacts that were discussed in Chapter 4.3.3 and are due a local variation of tip-sample distance (topography). It only produces a vertical shift of the single dI/dV -spectra and hence does not affect the energetic positions or line shapes of spectroscopic features. The analysis gives the identical fitting results

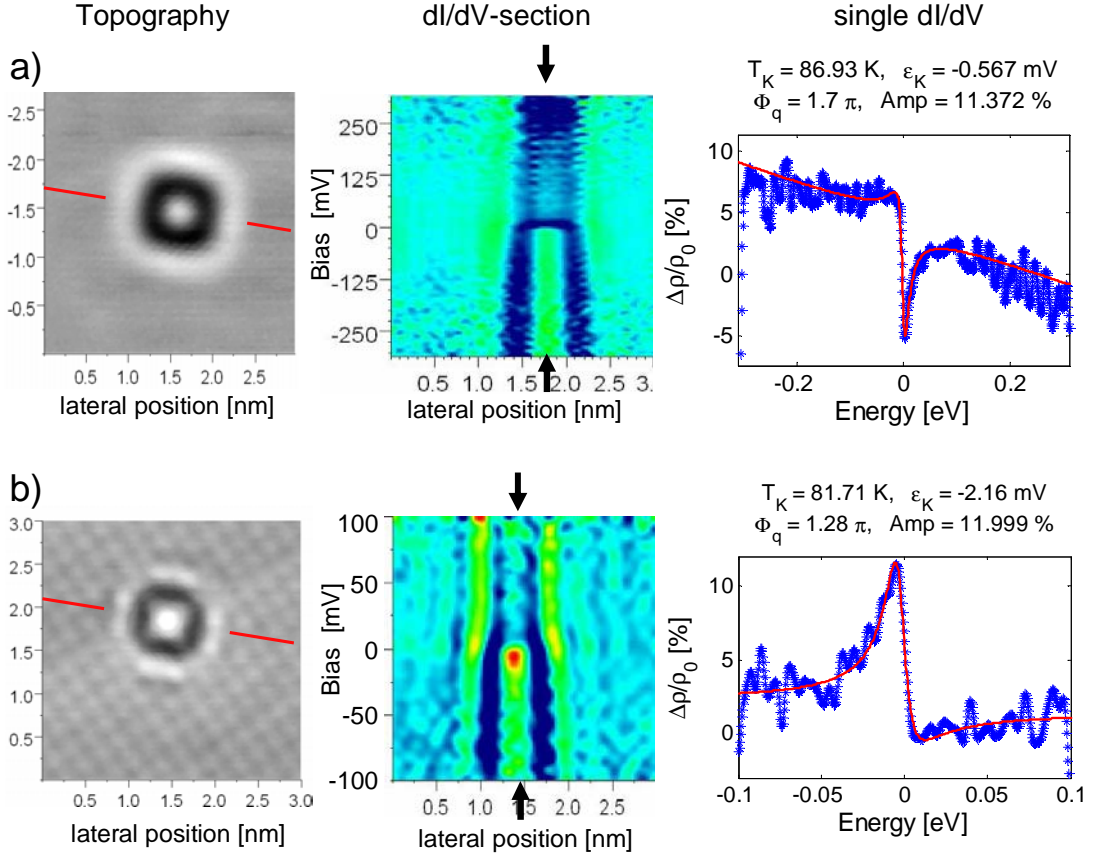


Figure 4.18: STS-data of 3rd layer Fe impurities: a) sharp anti-resonance near $V = 0$ b) atomically resolved 3rd layer Fe impurity: different line-shape but comparable Kondo temperature

without normalizing the STS-data to a constant tip-sample distance. Nevertheless, we will present data that is already properly normalized. Thereafter we will attempt to find a function $t_{imp}(\epsilon)$ that describes the experimental observations. This will be done by fitting the calculated LDOS-sections to measured spectrum sections. This will be a much more sophisticated task since it is sensitive to prevalent artifacts. But since it gives access to the key quantity of the experimental system, we will give it a try.

4.5.1 Fe impurities

In total 19 STS-measurements have been performed on subsurface Fe atoms in Cu(100) which each take about two hours of acquisition time. Only a small se-

lection of this data will be presented here in detail but all experiments have been analyzed concerning the width and position of the Kondo resonance. In all cases Fano functions have been fitted to the single STS-spectra taken in the middle of the defect pattern. This entirety of fitting results will be compared later but first of all a few characteristic spectrum-sections and single spectra will be presented.

The bias dependency of 3rd layer impurities was characterized in the constant current topographies by an abrupt reduction of size of the central maximum near zero bias. Obviously the tunnelling current is strongly reduced at this position from negative to positive voltages and this is compensated by placing the tip in closer distances to the sample. This loss of tunnelling current across $0V$ is equivalent to a negative peak in its derivative dI/dV . Indeed a sharp anti-resonance can be observed in the (normalized) dI/dV spectrum (Figure 4.18a). This spectroscopic feature is located near $V = 0V$ and causes an $\approx 11\%$ reduction of LDOS in the middle of the resonance. A Fano function can be successfully fitted to the dI/dV curve and gives a Kondo temperature of 87 K and a q-phase of $\Phi_q \approx -0.3\pi$. In the (topography normalized) spectrum section it can be observed that the central maximum is strongly reduced in size but persists for positive voltages. This is inconsistent with a full π -phase shift that would cause an inversion of the standing wave pattern across the resonance.

The calculations of chapter 4.2.2 showed a dependence of the obtained line-shapes on the tip-sample distance h . Indeed such effects were also observed in the experiments. Figure 4.18b) shows spectroscopic data of an atomically resolved 3rd layer Fe atom. In contrast to the previous example this data has been taken in a smaller energy-range of $\pm 100mV$ so that the Kondo resonance may appear broader in the single spectrum. However, the width and amplitude of the resonance are comparable to the experiment without atomic resolution. The line-shape however differs strongly and the q-phase is $\approx 0.4\pi$ smaller. This behaviour is expected from the calculations, since we showed that lower tip-sample distances result in lower q-phases. The spectrum section of this defect again shows a significant phase-shift around $0V$. This is again smaller than $\lambda/2$ and hence smaller than the expected value of π .

If the tip is moved laterally away from the center of the defect pattern, the distance to the impurity is enlarged. From the 1D-model an increase of the q-phase is expected for this case. This effect can be in general observed in all measured STS data and will be demonstrated using one data-set, where the effect is particularly pronounced. Figure 4.19 shows the spectroscopic data taken on 5th layer Fe impurity. From the analysis of the multi-bias topography it was evident that a local minimum directly above the impurity atom vanishes from negative to positive voltages. The tip has to retract relative to the free surface if the bias voltage is raised above $0V$. This is equivalent to a tunnelling current which is larger than on the free surface and

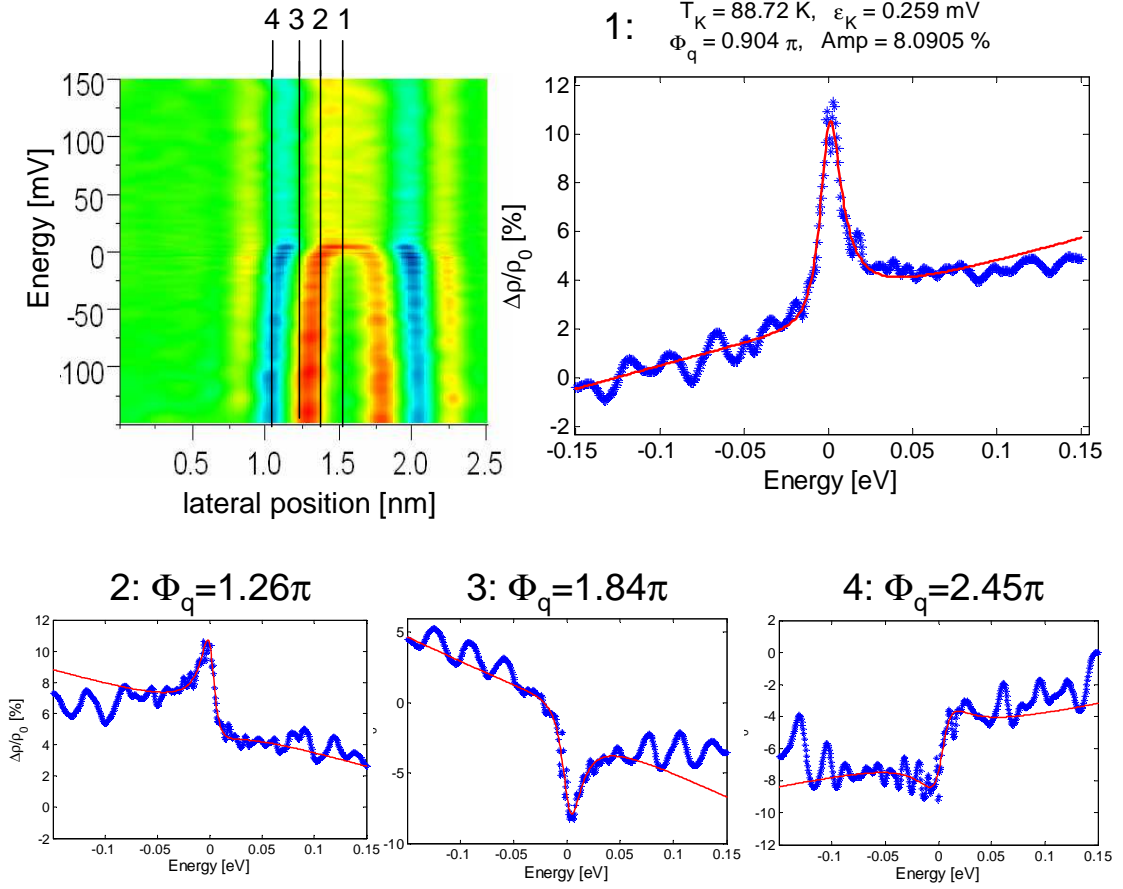


Figure 4.19: *5th layer Fe atoms show a peak-like spectroscopic signature at $V = 0$ directly above the impurity. If the lateral distance to the center of the pattern is increased, the line shapes become asymmetric and the q -phase increases*

consequently a peak can be seen in the tunnelling spectrum in the center of the defect pattern. The width of this resonance is comparable to that of the anti-resonance observed on the 3rd layer impurity. The spectrum section reveals that the phase-fronts are shifted inwards around 0V. A central minimum develops into a plateau-like maximum but overall phase-shift is again smaller than π . Single dI/dV spectra taken at positions 2-4 in Fig. 4.19 correspond to different lateral positions. They show different Fano line-shapes with an increasing q -phase the further the tip is moved away from the center of the pattern. Thus, the behaviour that was demonstrated in the 1D-model and that was also predicted by theoretical investigations [27] can be observed in reality.

4.5.2 Co impurities

We will now perform the identical analysis on the cobalt impurities. Here 17 measurements have been analyzed but we will again only show some representative examples. In general the spectral signatures of Co impurities are similar to those of Fe atoms as for instance a 3rd layer impurity also shows an anti-resonance in the dI/dV -curves and a disappearance of the central maximum from negative to positive voltages. The striking difference is the width of the spectroscopic features. Unlike the Kondo resonance of Fe atoms, which had a line width (HWHM) of $\approx 7meV$, the features of Co atoms show a width of $\approx 100meV$. In general this can be explained by the higher Kondo temperature of Co in Cu, which defines the width of the Kondo resonance.

A few spectroscopies of impurities in layers 3 to 6 are depicted in Figure 4.20

4.5.3 Comparison of the fitting results

Fe in Cu

In total 19 STS-measurements on different impurities using different STM tips have been analyzed. The results are summarized in Figure. 4.21. All these STS-measurements showed sharp spectroscopic features near zero bias with comparable line-width corresponding to a Kondo temperature of Fe in Cu of

$$T_K = (84.8 \pm 2.5)K$$

The Kondo resonance is located at at the Fermi energy and the average position is:

$$\epsilon_K = (-0.14 \pm 0.24)mV$$

Using the Friedel-sum rule [15] the occupancy of the d-orbital can be estimated:

$$n_d/N_d = (51 \pm 1)\%$$

Assuming a 10-fold degenerate d-orbital this would correspond an occupation number of $n_d \approx 5$. This is smaller than expected, as an isolated Fe atom has $n_d \approx 6$, which is slightly increased $n_d \approx 6.44$ according to DFT calculations [73], if the atom is incorporated in a copper environment. Thus we would expect the Kondo resonance further below $0V$. A possible explanation for this discrepancy will be discussed later.

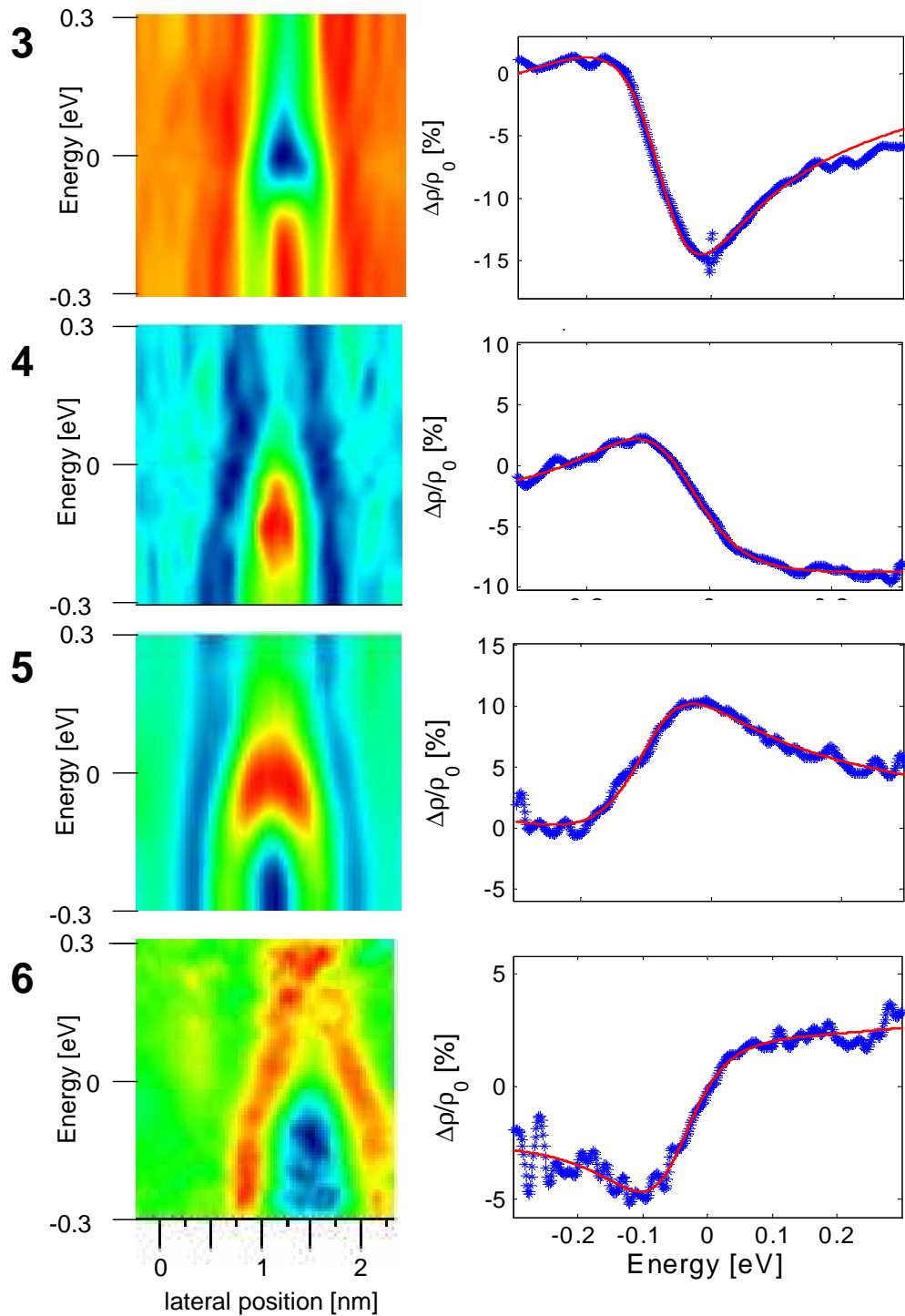


Figure 4.20: STS-data of subsurface Co-impurities in 3 to 6 layers below the Cu(100) surface. A phase shift can be observed in all cases and the single dI/dV spectra can show Fano line shapes.

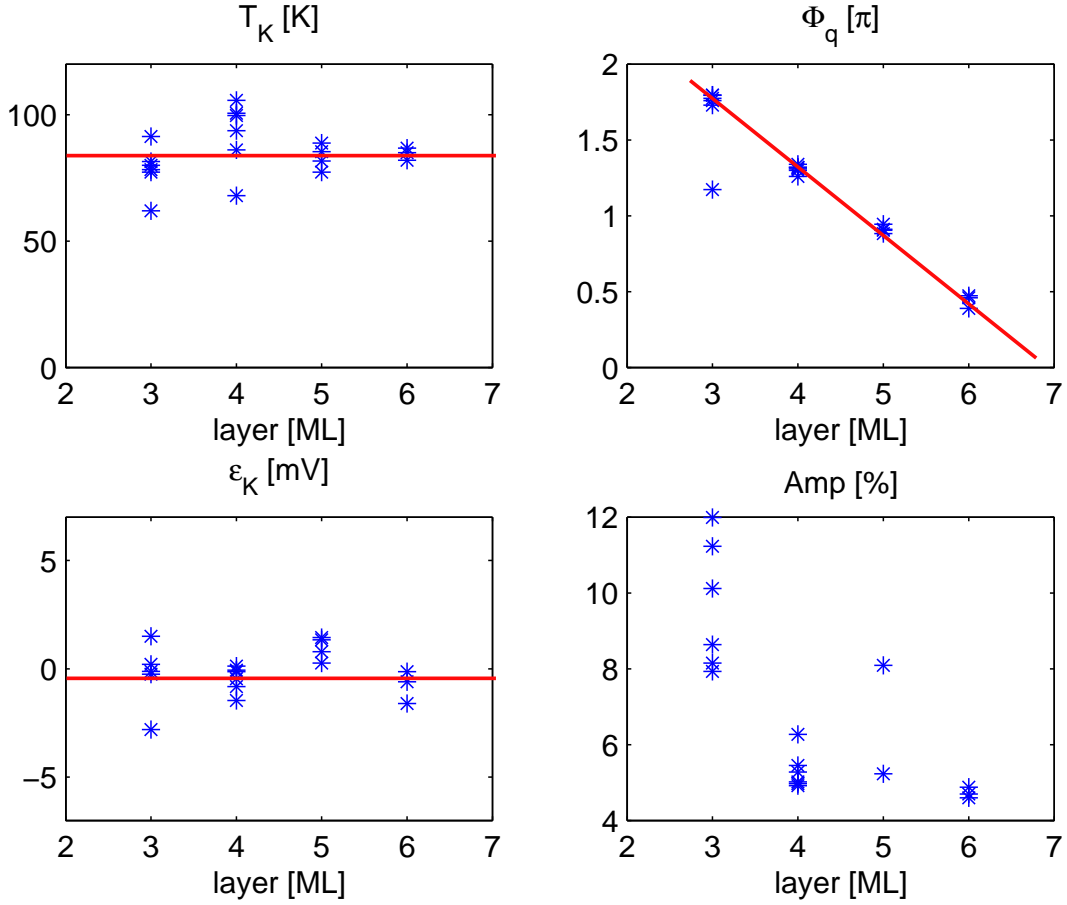


Figure 4.21: Comparison of the fitting results obtained on subsurface Fe atoms: Kondo temperatures around 80 K. The q-phase apparently decreases with increasing depth which turns out to be an aliasing effect.

In the upper right corner of Figure 4.21 a plot of the obtained q-phases versus the impurity depths is depicted. Apart from one single value corresponding to the atomically resolved 3rd layer impurity all other values show a linear decrease of q-phase with increasing distance. As was seen in the calculations, a better tip corresponding to lower values of h results in lower q-phases. This explains why the q-phase of the atomically resolved 3rd layer Fe atom is about 0.4π lower. A linear fit reveals a slope of $-0.44\pi/ML$ if the deviant data point is excluded. This slope corresponds to a periodicity of $4.6ML$ in the observed line shapes. At a first glance this is in striking contrast to the results of the 1D-model. From this one would expect an increasing q-phase with increasing distance and a periodicity of half the Fermi wavelength. Of course the q-phase is 2π -periodic and hence the

observations are also equivalent to a $+1.56\pi/ML$ -slope of q-phase. This is now in accordance to the expected behaviour and corresponds to a periodicity of $1.28ML$. The negative slope is due to an aliasing between the periodicity of the lattice and the wavelength of the LDOS oscillations. This was already observed in Chapter 3 when a 3D reconstruction of the propagator was performed. Since the lattice constant of copper is well known ($1ML \equiv 1.8\text{\AA}$) the slope of q-phase allows a determination of the Fermi wavelength. This periodicity of $1.28ML = 2.31\text{\AA}$ corresponds to a Fermi wave-vector of 1.36\AA^{-1} . The LCAO band structure gives values for $|\mathbf{k}_F|$ of 1.3 in [110] and 1.45 in [100] direction. Therefore the observed slope of q-phase is in very good agreement with the expected behaviour.

Co in Cu

The Kondo resonance observed on the subsurface cobalt atoms was much broader than in the case of Fe atoms. The average Kondo temperature obtained from 17 analyzed spectroscopies is:

$$T_K = (1253 \pm 42)K$$

The position of the Kondo resonance was located below $0V$ for all cases but varied between $-50mV$ and $-100mV$. The average value was determined as:

$$\epsilon_K = (-76 \pm 11)mV$$

This indicates that the d-orbital is more than half filled, as expected. We can again obtain the occupancy of the d-orbital from the ratio of both quantities by using the Friedel sum rule[15]:

$$n_d/N_d = (69 \pm 3)\%$$

This correspond to $n_d = 6.9$ electrons, if we assume a 10-fold degeneracy of the d-orbital. In the same way as in the case of the Fe atoms, where a ratio $n_d/N_d = (51 \pm 1)$ was determined, this value is lower than expected. Although this value is close to $n_d = 7$, which is expected for a free Co atom, one would expect a $n_d = 8.0$ according to DFT calculations [73] if the Co atom is incorporated in copper. One possible explanation for the above discrepancy could be the crystal-field splitting of the d-orbitals, which reduces the degeneracy to $N_d(t_{2g}) = 6$ and $N_d(e_g) = 4$. However, this consideration depends on the actual degeneracy and the internal configuration of the impurity atom in the host-metal's environment. Even for *ab-initio* calculations, the determination of such information is a challenging task, since correlation effects can have a great impact on these properties. Thus, we leave the determined values of n_d/N_d as they are and do not deduce any conclusions about the orbital configuration from them.

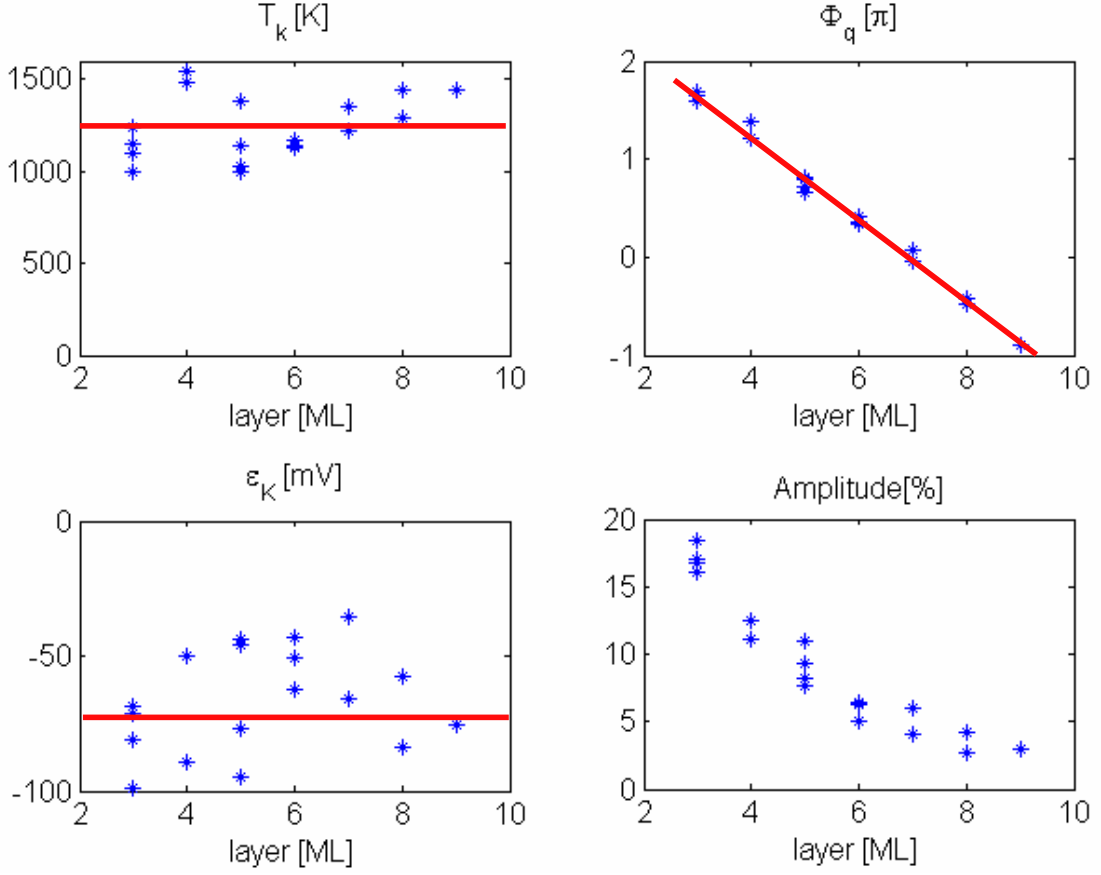


Figure 4.22: Summary of the fitting results of Co impurities in Cu(100): monotonous decrease of Amplitude, Kondo temperature around 1250K and a linear decrease of q -phase with increasing depth (aliasing)

The obtained values of Φ_q again show a linear decrease with increasing depth. This is again an aliasing between the wavelength of the LDOS-oscillations and the periodicity of the atomic lattice. A linear fit reveals a slope of $d\Phi_q/dd = -0.42\pi/ML \equiv +1.58\pi/ML$. The identical analysis that was also performed to the Fe-data gives a Fermi wave vector of 1.37\AA^{-1} .

The plot of amplitude versus depths shows a monotonous decrease with increasing depths. The values for the particular depths are in general larger than those determined on the Fe atoms. A 3rd layer Co atom shows a mean amplitude of $\approx 17\%$ while a 3rd layer Fe atom showed a $\approx 10\%$ reduction of normalized differential conductance in the middle of the Kondo resonance. Although the amplitude shows a smooth decay as with increasing depth, it cannot be described by a pure d^{-1} or

d^{-2} behaviour. This would be expected if the Fermi-surface is solely cylindrical and ellipsoidal, respectively.

4.5.4 Discussion of the experimental findings

All described data of cobalt and iron impurities showed spectroscopic signatures in the dI/dV -curves near zero bias that could be successfully fitted with Fano-functions. The fitting provided comparable line-widths for each system and the measured Kondo temperatures were $(85 \pm 3)\text{K}$ for Fe in Cu and $(1253 \pm 42)\text{K}$ for Co in Cu. In all cases the q-phase increased if tip is moved away laterally from the center of the defect pattern and apparently decreased with increasing depth of the impurity. The latter observation was identified as an aliasing effect so that all measurements consistently describe an increase of q-phase versus distance. This is the behaviour that is expected from a generic scattering resonance and was also reproduced by the 1D-model described in section 4.2.1.

Although this behaviour was predicted by theory [27, 26] it was up to now not observed in STM-experiments. In the measurements of Manoharan *et al* [25] the amplitude of the Kondo resonance decreased as the tip was moved away from the magnetic impurity but the line-shape stayed identical. Knorr *et al* [21] showed a decrease of the q-value versus the lateral distance for Co impurities that were *adsorbed* on the Cu(100) surface. This is the opposite behaviour of what is expected. Most probably these disagreements are due to the fact that their experiments were performed on adsorbates and thus the comparison of different lateral positions is always attended with comparison of different tunnelling geometries. The approach presented here obviously avoids this difficulty as the impurities were buried below the surface. Hence the tunnelling of electrons always occurs between the STM-tip and an atomically flat copper surface.

The Kondo temperatures obtained in this work are in general higher than those reported in literature. As mentioned earlier the Kondo Effect influences multiple physical properties and can be therefore investigated using different methods. The measurement of resistivity versus temperature is the most prominent manifestation of the Kondo Effect. But many other quantities as the magnetic susceptibility, the thermoelectric power among others show anomalies that can be used to determine the Kondo temperature of a given system. A review of such measurements can be found in [72]. Figure 4.23 shows a comparison of the measured Kondo temperatures of various 3d elements in copper. They show values of 200-1000K for cobalt and 5-50 K for iron impurities. In general macroscopic measurements average over large ensemble of impurities so that the prepared samples can potentially also contain

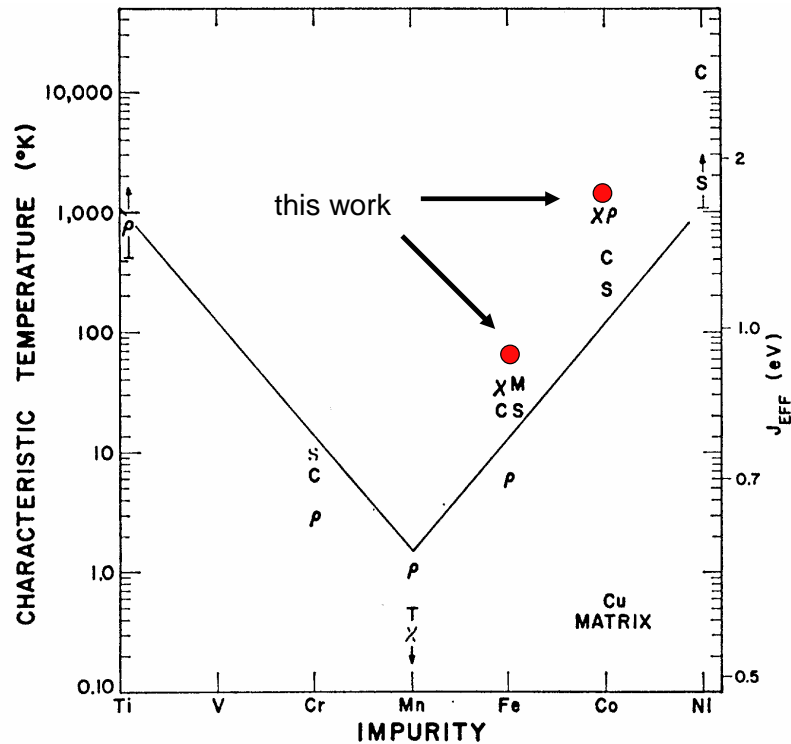


Figure 4.23: Comparison of the Kondo temperatures for 3d-transition metals in copper: red dots indicate the values we obtained by the fitting of Fano-functions to dI/dV -curves. They are in general larger than those values determined by thermodynamic measurements (ρ : resistivity, χ : susceptibility, S : thermoelectric power, C : specific heat and M : Mössbauer). Figure reproduced from [72]

dimers and clusters. However, it appears more probable that the Kondo temperatures determined here are too high than that all values of T_K measured by other groups are too low.

It could also be observed that all measured spectrum-sections showed a much lower phase-shift than the value of π that is expected from the Anderson-model. All presented calculations always showed an inversion of the LDOS pattern across the resonance. These were the 1D-model, solved by diagonalizing the non-interacting Anderson-model, and the LDOS sections that were obtained by combining the host Green function with a hypothetical t-matrix. In contrast to that the experiments showed a phase-shift that was of much smaller size - most probably below 0.5π . Nevertheless, a phase shift can be clearly identified and turned out to be the striking fingerprint of the Kondo Effect in the STM-topographies. Impurities that showed a strong voltage dependence of the constant current topographies near zero bias

always revealed sharp spectroscopic features in the STS-measurements. Regarding the extent of the phase-shift the observations deviate from the expected behaviour. We want to discuss now what the reason for that might be.

4.5.5 Background scattering

The Anderson model is an approximate description of an impurity which is incorporated in a metal. From a conduction band electron's point of view the only perturbation is a hybridization with the impurities d-orbital. Apart from that no additional scattering processes are included. The amplitude of the observed LDOS oscillations is proportional to the amplitude of the t-matrix while the positions of LDOS-maxima and -minima are determined by the phase of $t_{imp}(\varepsilon)$. The proposed t-matrix for the local moment regime (eq.4.14) consists of three scattering resonances, which are each assumed to be describable by a complex Lorentzian. As a consequence the scattering amplitude decreases monotonically with the energetic distance $|\varepsilon - \varepsilon_K|$, unless ε gets into the energetic range of the Hubbard bands. This was also observable in the calculated spectra sections (Chapter 4.2.2) where the LDOS-oscillations at $\pm 300mV$ were of low amplitude compared with the pattern at $0V$. In contrast to that the experiments of Fe in Cu(100) showed that although the Kondo resonance was extremely narrow a significant amplitude of the LDOS oscillations was still observable at energies of $\pm 300mV$ i.e. far away from the resonance.

One possible explanation for this could be an additional, approximately energy-independent "background"-scattering. Of course this could be due to the tails of the Hubbard bands and would then be already included in the Anderson model. But also scattering processes due to a local strain field or a hybridization with the s-orbital of the impurity are possible and such processes would not be considered in equation 4.14 so far.

It will now be analyzed how a background scattering would affect the measured spectrum sections and the corresponding single spectra. For simplicity we "switch off" the Hubbard bands ($Z_d = 0$, $Z_U = 0$) and include only the Kondo resonance in the model t-matrix. This leaves one complex Lorentzian whose general properties are summarized in Figure 4.24. Its real part is an antisymmetric function around $\varepsilon = \varepsilon_K$ while the imaginary part is negative for all energies and shows minimum for $\varepsilon = \varepsilon_K$. A helpful concept to visualize a complex function is the Nyquist plot[74]. It describes the positions of $t_{imp}(\varepsilon)$ in the complex plane for different energies. Another representation is the plot of amplitude and phase versus energy, which is also termed Bode plot[75]. Both are depicted in Figure 4.24. The Nyquist plot of a complex Lorentzian is a circle that is adjacent to the real axis. The red marker indicates

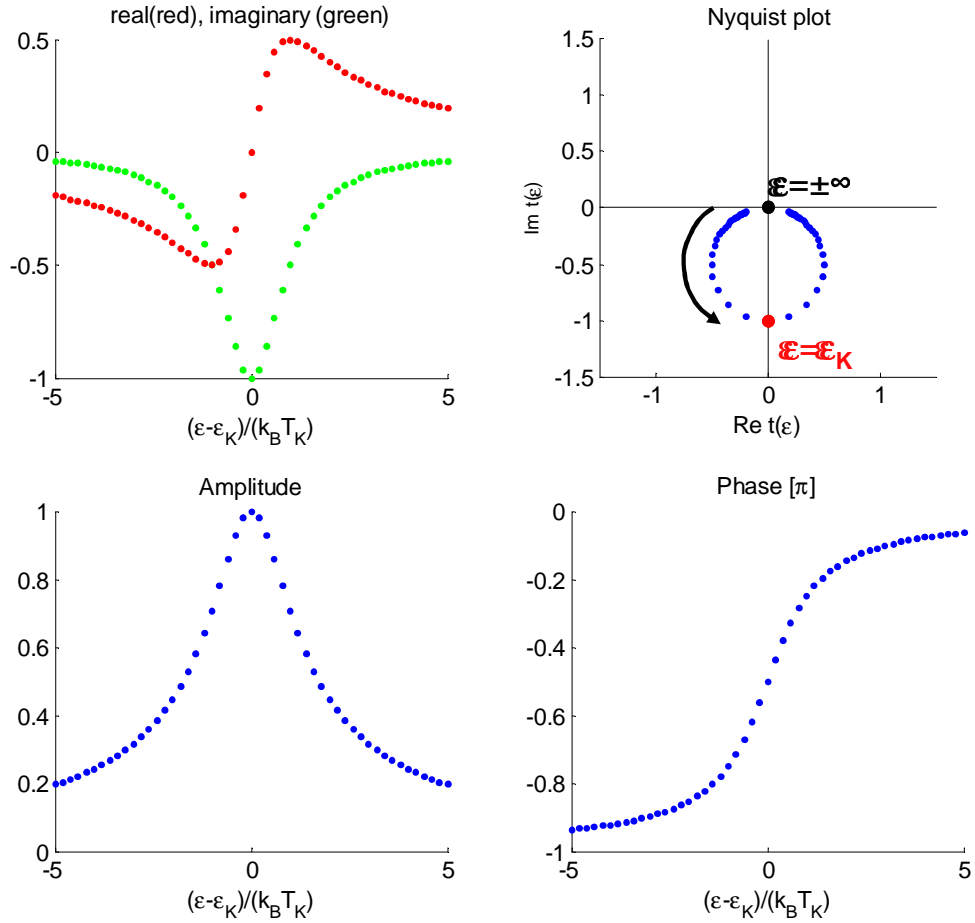


Figure 4.24: *Properties of a complex Lorentian: the Nyquist-plot shows a circle in the complex plane that is adjacent to the real axis*

the value of t_{imp} for $\varepsilon = \varepsilon_K$ i.e. in the middle of the resonance while the black dot is the value of the t-matrix for $|\varepsilon - \varepsilon_K| \rightarrow \infty$ i.e. far away from the resonance. In Figure 4.24 the energetic spacing between two subsequent points was chosen to $0.2 \cdot k_B T_K$. Thus it can be seen that the t-matrix changes rapidly near ε_K . The overall phase-shift of the resonance is π as the values of t_{imp} are near the negative real axis for energies far below the resonance and approach the positive real axis for $\varepsilon \rightarrow +\infty$.

An energy independent scattering process can be described by a constant t-matrix which is just some complex number. The total t-matrix would then be sum of the resonant and the non-resonant (background) channel. The Nyquist plot then shows a circle that is moved away from the origin in some direction. It is obvious that the behaviour of the system depends on the relative strength and the relative phase of

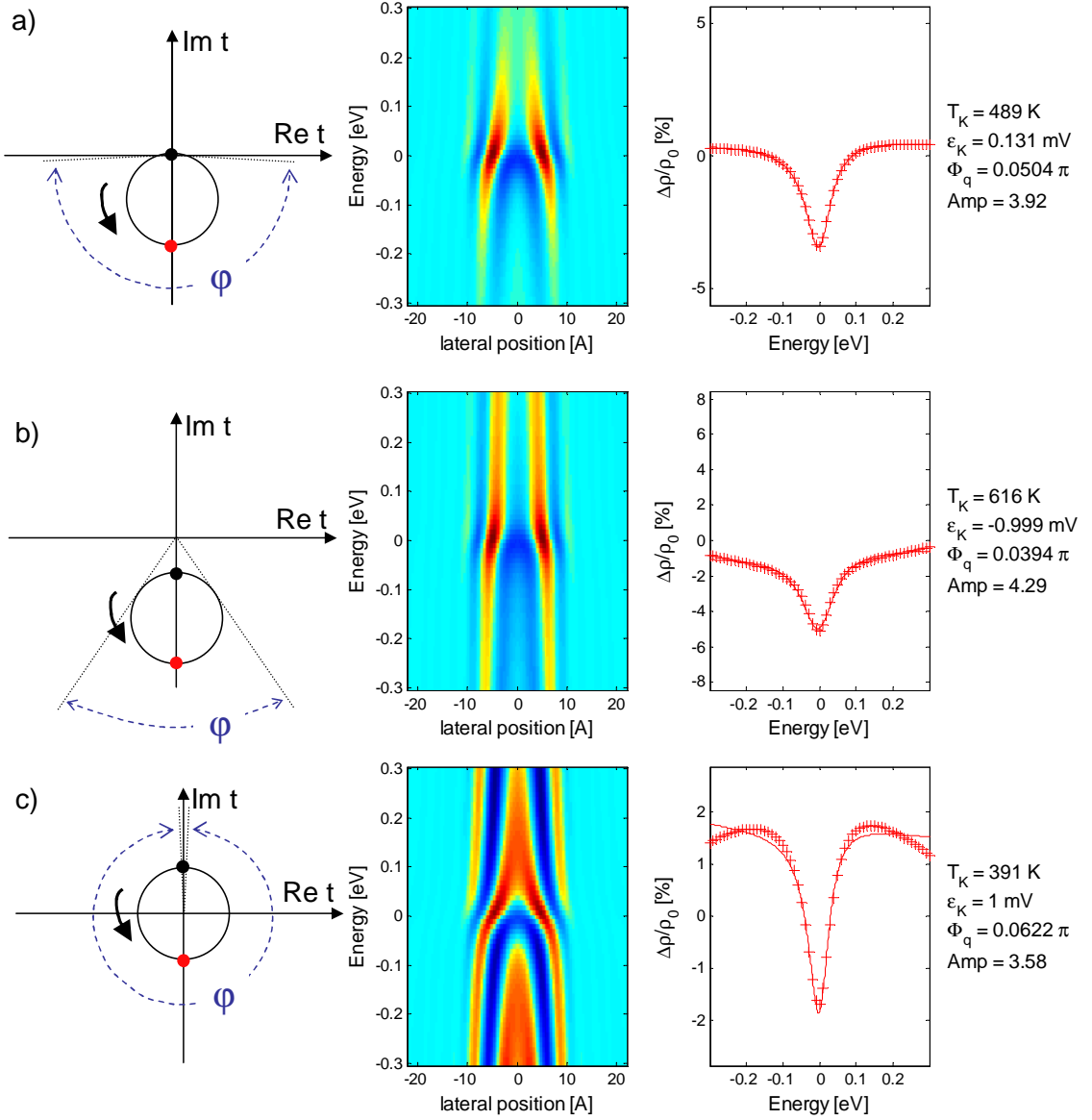


Figure 4.25: Calculated LDOS sections and spectra for different "background" scattering processes. Left side: Nyquist-plot of the t -matrix - black dots indicate $\epsilon \ll \epsilon_K$ and $\epsilon \gg \epsilon_K$ while red dots correspond to $\epsilon = \epsilon_K$. a) no background scattering - t -matrix of eq. 4.14 with $Z_d = Z_U = 0$ (Hubbard bands "switched off") resulting in π -phase shift. b) additional constructively interfering process: reduced phase-shift and overestimation of Kondo temperature c) additional destructively interfering process: phase-shift of 2π and underestimation of Kondo temperature.

the resonant and the background process. This is demonstrated for three cases.

Fig.4.25 a) shows the Nyquist-plot, the spectrum-section and the single spectrum without any background scattering for a 6th layer impurity. The spectrum section shows a π -phase shift and a low amplitude of the LDOS-modulations for $\varepsilon = \pm 300mV$. If the background channel interferes constructively for $\varepsilon = \varepsilon_K$ (Fig. 4.25b) the spectrum section show a much smaller phase-shift than in example a). In the Nyquist-plot the reason for this behaviour can be clearly seen. The locations of the different values of t_{imp} in the complex plane are limited to an angle φ which is much smaller than π . As an interesting detail it can be observed that fitting a Fano-function gives a "measured" Kondo temperature that is about 20% larger than the "real" value of 500K. In the third case (Fig. 4.25c), the background channel interferes destructively with the resonant channel for $\varepsilon = \varepsilon_K$. Here the Nyquist plot of the t-matrix is a circle that surrounds the origin. In the presented case the amplitude of t_{imp} is constant for all energies and the calculated LDOS-section shows oscillations, whose amplitude does not change versus energy. The phase however shows stronger variations than for the case of the pure Lorentzian of Fig. 4.25a. This is obvious since the t-matrix completely circles the origin of the complex plane which corresponds to a phase-shift of $\varphi = 2\pi$. The Fano function shows an inferior agreement to the calculated spectrum and the obtained Kondo temperature is more than 20% lower than the value entered in the resonant part of the t-matrix.

In the experiments we observed a reduced phase-shift and a scattering amplitude even for energies that are far away from the resonance. Consequently the experimental behaviour is similar to the example of (Fig. 4.25b.) where the background process and the resonant channel were constructively interfering for $\varepsilon = \varepsilon_K$. In this example the fitting of a Fano-function provided higher values of T_K than the one inserted in the t-matrix. This could explain why the experimentally obtained Kondo temperatures were larger than those reported in literature. However, in principle a variety of different relative phases and relative strengths of the resonant and the background channel are possible and each one of these t-matrices will produce a different LDOS-section and potentially different fitting results. We will now try an approach to analyze the behaviour of the experimental system in more detail. Its purpose is to extract the t-matrix of the magnetic impurities from the experimental data.

4.5.6 Experimental determination of $t_{imp}(\varepsilon)$

As noted earlier the key quantity of our system is $t_{imp}(\varepsilon)$. It is a complex function describing the scattering amplitude and phase-shift of the impurity versus energy.

Previously different "guesstimates" for this function have been made. A complex Lorentzian, describing a circle in the complex plane produces a phase shift of π , if no additional scattering processes are present i.e. if the scattering amplitude vanishes far away from the resonance. If an additional background scattering is assumed, the phase-shift can be less than π or 2π depending on the relative phase and strength of the resonant and the background process. Every of these approaches for $t_{imp}(\varepsilon)$ approximately produces Fano line shapes in the single spectra and it is obvious that different functions of $t_{imp}(\varepsilon)$ may produce the identical single spectrum if only one lateral position \mathbf{x}_{\parallel} is considered. This ambiguity can be removed if the correct description of spectra at different lateral positions \mathbf{x}_{\parallel} is attempted with the identical t-matrix. In other words the t-matrix has to correctly reproduce the measured spectrum sections. Instead of *guessing* a t-matrix we now want to try the opposite approach and fit the calculations to the measured spectrum sections in order to determine $t_{imp}(\varepsilon)$ experimentally.

The lateral comparison of STS-data is a challenging task, since a thorough elimination of artifacts due to the non-constant tip-sample distance is necessary. This was described in the beginning of this chapter. If not done properly, it may produce nonsensical results. In the uncorrected data of Figure 4.11 no LDOS-oscillations can be observed in that part of the energy range between 0V and the set-point voltage V_T . Therefore the fitting would erroneously provide a vanishing scattering amplitude for these energies. The following analysis was performed using STS-data of defects that were measured twice using different set-point voltages V_T and it was assured that both provided comparable results.

For this the lateral distribution of differential conductance was analyzed and the calculations were fitted to the experimental data for every energy and using fixed values of d and h . This procedure was done similar to the one applied to the constant current topographies in Chapter 3. Since both the calculations and the experiments are properly normalized to $\Delta\rho/\rho_0$ the fitting provides the absolute value and the phase of t_{imp} for every energy. The fitting was done automatically using one spectrum section and the Green functions for different energies. The resulting t-matrix is plotted as a Nyquist-plot, where a red marker now indicates the position of $V = 0V$, and as well as the functions $\text{Re } t_{imp}(\varepsilon)$, $\text{Im } t_{imp}(\varepsilon)$, $|t_{imp}(\varepsilon)|$ and $\Phi(t_{imp}(\varepsilon))$ versus energy. Additionally, a calculated spectrum section using the obtained t-matrix is generated allowing a direct comparison of the fitting results with the experimental data.

We start with the 3rd layer impurities. Figure 4.26 shows the fitting results obtained on a subsurface Co atom. One can see that the fitting works very well and a perfect agreement between the experimental observation and the calculated spectrum can be obtained. The plot of the scattering amplitude versus energy clearly shows a

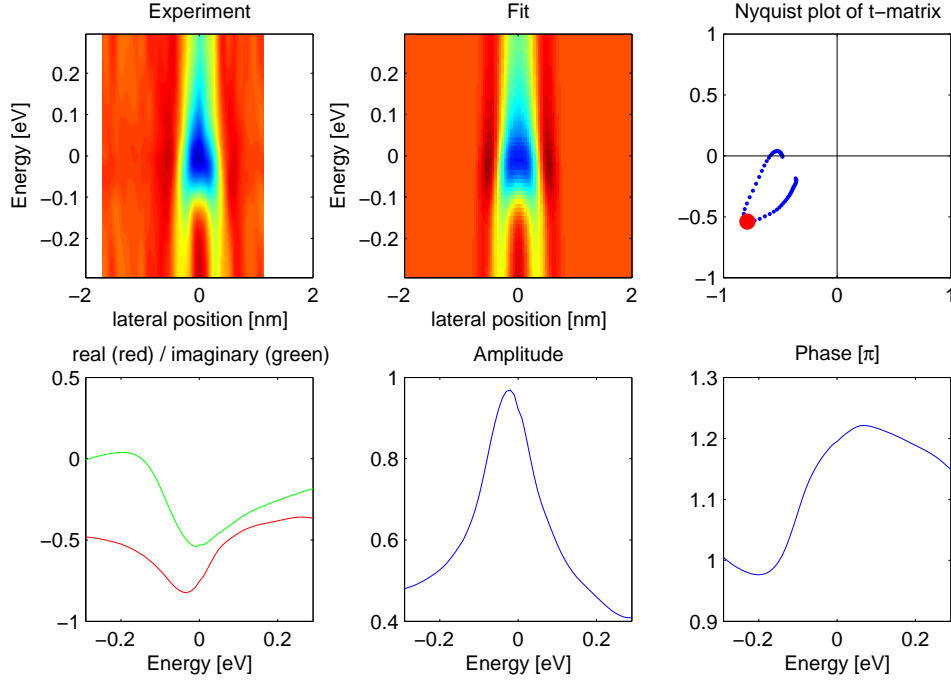


Figure 4.26: *Extracted t -matrix of a 3rd layer Co atom in copper. Fitting was performed using $d = 3.3ML$, $h = 7\text{\AA}$ and using an energetic step size of $10mV$.*

resonance around zero bias. Additionally a positive shift of the scattering phase can be observed between $V = -150mV$ and $V = +50mV$. The extent of this shift is slightly above 0.25π . This can be also observed in the Nyquits-plot of t_{imp} in the complex plane which shows a clear loop which is entirely within the third quadrant of the complex plane. This loop is not a circle (as a complex Lorentzian would be) but shows a more elongated shape. It is clearly not adjacent to the origin. This indicates that a background process is present.

The results of this investigation depend on the chosen parameter d . Of course a bad agreement is achieved if d is chosen far away from the "correct" value but a small variation in the order of $\pm 0.1ML$ leaves the shape of the loop unchanged but rotates the whole pattern in the complex plane by $\mp 0.15\pi$. This was already observed when fitting the topographies in Chapter 3: if the impurity is moved away from the surface, the phase-fronts have to be pushed outward in order to obtain a comparable pattern at the surface. This leads to a negative shift of scattering phase if d is enlarged. The obtained scattering amplitudes are enlarged if d is increased. This can also be easily understood as G_0 becomes more attenuated for larger distances. The t -matrix has to compensate this decay if the modulation of LDOS is of identical strength. If a fit

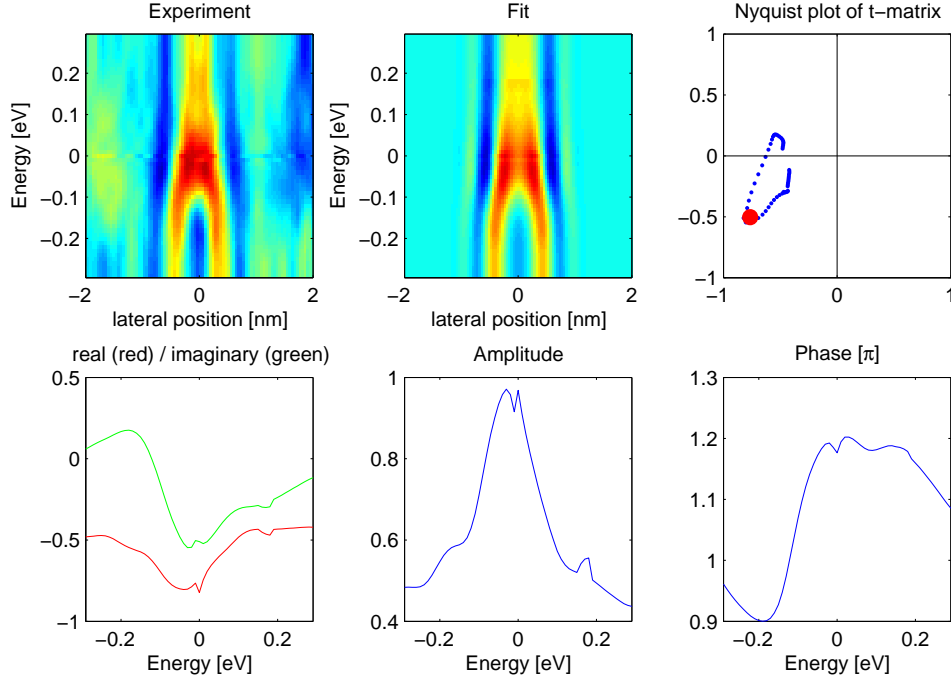


Figure 4.27: *Extracted t -matrix of a 5rd layer Fe atom in copper. Fitting was performed using $d = 5.3ML$, $h = 7\text{\AA}$ and using an energetic step size of $10mV$.*

is performed for instance using $d = 3.5$, the the overall scattering amplitude even exceeds the unitary limit. This demonstrates, that the procedure cannot determine the absolute value of the scattering amplitude and the absolute orientation of the resonance loop in the complex plane certainly.

If a 5th- layer Co atom is fitted using $d = 5.3$ (Fig.4.27) both the Nyquist-plot and the functions of phase and amplitude versus energy look comparable to the result of the 3rd layer impurity. Again a peak-like resonance can be seen in the plot of amplitude versus energy and a $\approx 0.3\pi$ shift of scattering phase is present. The extracted t -matrix of a 3rd layer Fe impurity (Fig.4.28) looks similar concerning the orientation in the complex plane but is lower in amplitude. This agrees with the lower amplitudes of the fitted Fano-curves for Fe impurities. The resonance loop is more circular than for Co impurities and the phase-shift is again $\approx 0.3\pi$.

Although the described procedure shows a good agreement between the fitting results and the measured data, the results should not be over-interpreted. At the beginning of this chapter it has been explained that the assumed identity $\Delta\varrho/\varrho_0 = (\Delta I/dU)/dI_0/dU$ is not precisely correct. The normalized differential

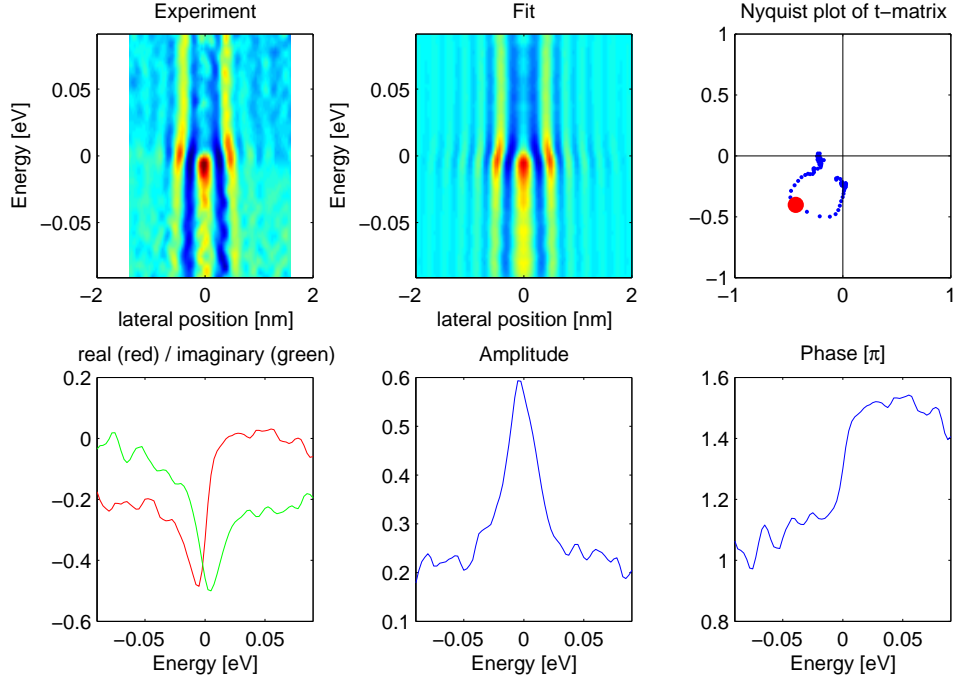


Figure 4.28: *Extracted t -matrix of a 3rd layer Fe atom in copper. Fitting was performed using $d = 3.3ML$, $h = 3\text{\AA}$ and using an energetic step size of $2.5mV$.*

conductance overestimates the strengths of spectral features in $\Delta\rho/\rho_0$ above $V = 0$ and vice versa. This might explain why the measured loop is somehow distorted and not of a circular shape. Especially in the case of Co, where the Kondo resonance is extended over a larger energy interval, the differences between $\Delta\rho/\rho_0$ and $(\Delta dI/dU)/dI_0/dU$ could effect the shape of the resonance loop. The Kondo-resonance of Fe however occurs in a very small energy range so that the normalization should be valid. Here a more circular shape is observed.

In conclusion it was shown that in principle the key-quantity of a Kondo system can be accessed by combining STS-experiments and calculations of the host-metal Green function. However, a quantitative determination of the "real" t -matrix is only approximately possible. This is because the results depend on the chosen value of d , the agreement between the calculated Fermi surface and the "real" Fermi surface and the correctness of the STS-normalization we used for this analysis.

Chapter 5

Outlook

In this chapter we will briefly discuss possible applications of the electron focusing effect. As was demonstrated previously in this thesis, the main physical reason for the particular shape of sub-surface impurities in the STM-topographies can be found in the shape of the propagator of the unperturbed host material. Although surface reflections and a k_{\parallel} -dependent decay within the vacuum were necessary to achieve a *quantitative* agreement with the experimental observations, a *qualitative* understanding was already achieved in section 3.2 with the knowledge of G_0 only. The "shape" of G_0 in turn can be quickly obtained from the Fermi-surface.

Indeed the Fermi-surfaces of all solids deviate from a spherical shape. Hence the corresponding propagators are anisotropic and this fact will reveal new effects in well known materials.

Nano-sonar

For copper and many other materials showing electron focusing (e.g. Pb), the existence of beam-like propagation paths could be used to construct a "nano-sonar" (Fig. 5.1a). Such a device could determine not only the depths of the impurities themselves (as done here) but also the depth and reflectivity of buried interfaces. Here, in addition to the previously described LDOS-oscillations caused by processes of direct propagation between impurity and surface, larger, concentric rings should appear that are produced by electrons being scattered by the impurity and reflected at the interface. The effect can be nicely observed in the *ab-initio* calculations of Lounis *et al.* Due to the slab technique, a highly reflecting "interface" (the lower boundary of the slab) is present 18 ML below the surface. This produces a second

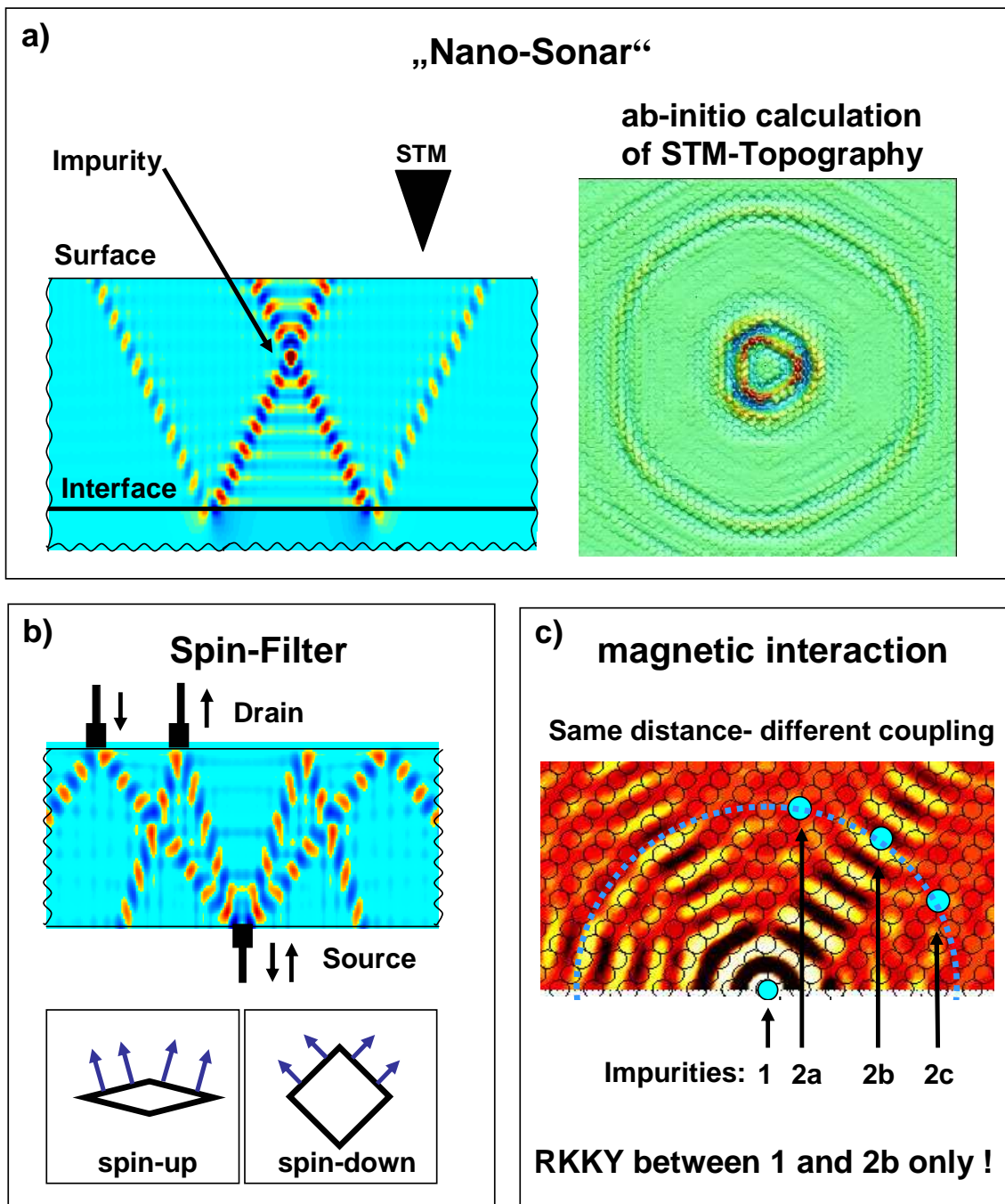


Figure 5.1: Applications based on focusing properties of the single electron propagator: a) Nano-Sonar: a buried interface below the impurity produces a second, concentric LDOS-modulation. An STM-investigation of the surface LDOS would gain access to the depths and the reflectivity of both impurity and interface. b) Spin-Filter: in a ferromagnetic material a spin-unpolarized current emitted from a point-contact ($S_{\uparrow\downarrow}$) splits up due to the different Fermi-surfaces and thus different propagators of majority and minority spins. c) (conduction electron related) indirect exchange interaction between two magnetic atoms in Copper: strong and long-range interaction only between impurities 1 and 2b, i.e. in the directions of the focused beams.

ring-like LDOS oscillation having a larger diameter. From the knowledge of G_0 it is easy to obtain the depths of interface and impurity below the surface using trigonometric relations.

The possibility to study buried structures with the STM was shown on subsurface Argon bubbles in Aluminum [76]. They presented calculations based on a Jellium model i.e. with a free-electron like dispersion to explain their observations. Recently these Argon-induced nano-cavities were also observed in Cu(100)[77].

Although not being a "nano-sonar" in the above sense (which requires a single impurity *and* a interface) the next example demonstrates that the width of the oscillations's envelope in the radial direction does not diverge with increasing distance. Fig 5.2 shows a single Fe atom in the 5th layer and a deeply buried linear defect of unknown origin. The latter one produces a large elongated pattern of $\approx 6 \times 8nm$ size. Here we can again nicely observe that the focusing cone is still ≈ 1.5 oscillations in width. From the knowledge of the propagator's geometry we can assume that the defect is in a depths of 22-24 ML, approximately 8 atomic distances in length and oriented in [110] direction. The reason for this elongated pattern could be a dislocation or a buried chain of impurities, but it is sure that this defect is not a *singe* Fe atom. Within $\pm 10mV$ the singe 5th layer Fe atom again shows the Kondo-specific phase-shift that was described in Chapter 4. The pattern arising from the deep linear defect however does not change within $\pm 10mV$. From this it is obvious that the dispersion of electrons in Copper is completely negligible in this energy interval and cannot be responsible for the variations observed on the Fe impurities.

Spin-filter

Ferromagnetic materials possess different Fermi-surfaces and therefore different propagators for electrons having majority and the minority spin. This should allow the design of effective spin-filters (Fig. 5.1b) if both propagators show a focused propagation in different directions. A mixture of both spin-species enters the ferromagnet at a point-like source contact ($S_{\uparrow\downarrow}$) from which \uparrow and \downarrow propagate in different directions and are collected at different drain-contacts D_{\uparrow} and D_{\downarrow} . According to recent theoretical calculations [78] bcc-Europium may be a good candidate for this purpose.

RKKY and IEC

We have demonstrated highly anisotropic charge density oscillations due to subsurface point defects. If a magnetic impurity scatters spin-up and spin-down differ-

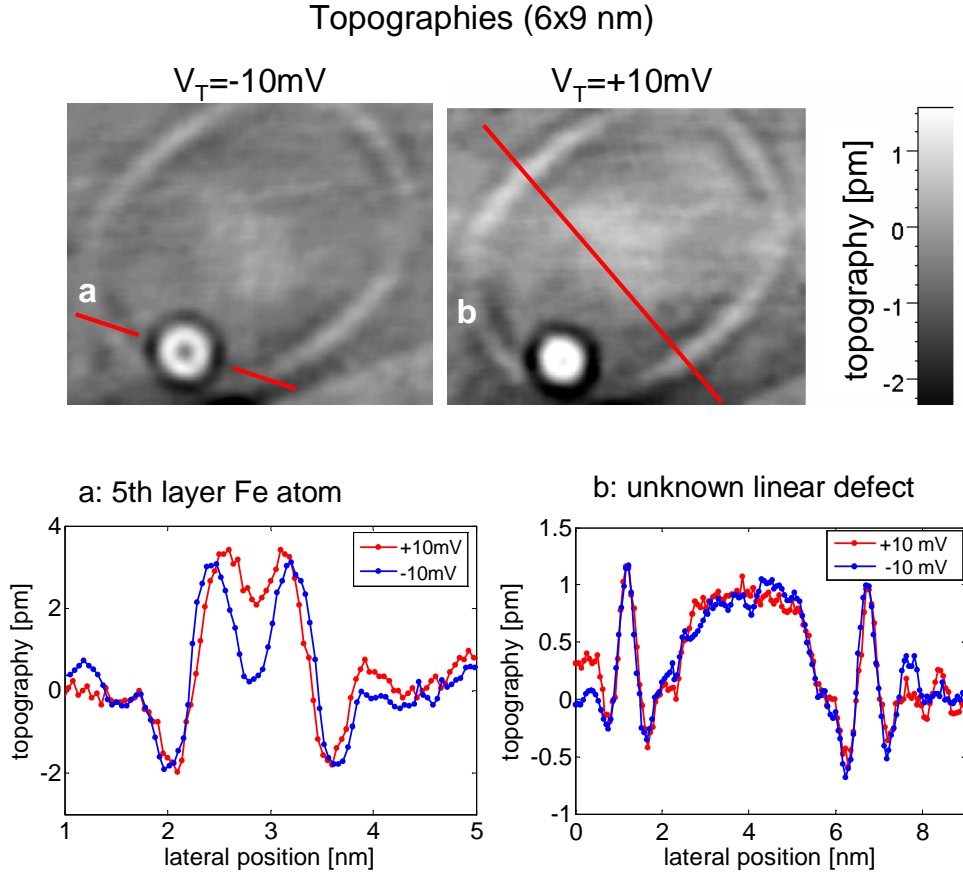


Figure 5.2: *STM topographies of a 5th layer Fe impurity and a deeply buried linear defect of unknown origin.*

ently, this leads to an oscillatory behavior of spin density which are called RKKY (*Ruderman-Kittel-Kasuya-Yosida*)-oscillations [6]. A second magnetic atom may sense the spin-polarization induced by the first atom giving rise to a (conduction electron related) indirect exchange interaction. This long range interaction oscillates between a ferromagnetic and anti-ferromagnetic coupling with a periodicity of half the Fermi-wavelength. In Figure 5.1c we plotted the calculated LDOS-oscillations onto the atomic lattice. Although the impurities 2a, 2b and 2c are placed in approximately identical distance to impurity 1, a strong magnetic coupling will only take place to impurity 2b. This is because it is positioned on the focusing beam of the first impurity. Since the interaction is mediated by the conduction-band electrons, their propagator is the physical quantity that defines the directionality and the spatial decay of the interaction.

The step from coupling two separated magnetic atoms to coupling magnetic layers is straightforward. If magnetic layers (e.g. Co) are separated by non-magnetic spacers (e.g. Cu) the magnetic coupling depends on the spacer material and its crystallographic orientation. The *interlayer exchange interaction* (IEC) is strong and long-range, if the layers are oriented perpendicular to directions of preferred propagation. In deed the theory of the interlayer exchange coupling [3] depends on the geometry of the Fermi-surface and uses the same concepts (effective mass tensor, principal curvatures, group velocities), that were also discussed in Section 3.2 For copper as spacer material, the predicted coupling strengths of (110)-oriented layers are 9 times higher than those having (111)-orientation. As can be seen from the calculated propagator (Fig.3.5) the [110] direction is in line with the focusing beam.

Chapter 6

Summary

In this work we presented a comparative STM and STS study of single subsurface iron and cobalt atoms in copper. The experimental systems were prepared under UHV conditions by co-deposition of the host metal and the impurity atoms onto single crystals of Cu(100) and Cu(111).

The STM topographies taken at 6K showed strongly anisotropic short wavelength oscillations of the local density of states (LDOS) in the vicinity of the defects. Impurities located up to 15 ML below the surface could be clearly identified in the STM topographies. It was shown that the observed anisotropies arise from the non-spherical Fermi-surface of copper which causes a preferred propagation of bulk electrons in narrowly confined directions. This produces an electron focusing effect leading to four-fold symmetric patterns on the (100) surface and to three-fold symmetric patterns on the (111) surface. These characteristic signatures of subsurface impurities were reproduced by calculations based on the host metal's band structure that also included the effect of the surface and of the k_{\parallel} -dependent decay of the wave functions into the vacuum. We obtained a good agreement of the calculations to the experiments and to the result of *ab-initio*-calculations.

In the second part the Kondo Effect of subsurface impurities was analyzed. In the case of Fe impurities the bulk state interference patterns changed significantly close to zero bias. This effect could even be observed within $\pm 3mV$ bias voltage range. It was excluded that this effect can be caused by the energy dependence of the host metal's band structure, i.e. its dispersion $E(k)$. We have shown that the observations are related to a change of the scattering phase shift around zero bias. This was identified as the fingerprint of the Kondo effect in real space.

Using Scanning Tunnelling Spectroscopy it was shown, that both species of impurities show characteristic Kondo features on distinctly different energy scales. The dI/dV spectra reveal Fano line shapes whose asymmetries depend on the depth of the impurity below the surface and the lateral position with respect to the center of the defect pattern. It was shown that the q -phase increased if the tip was moved away laterally and apparently decreased with increasing depths of the impurity below the surface. The latter effect was identified as an aliasing between the wavelength of the LDOS-oscillations and the periodicity of the atomic lattice. The obtained Kondo-Temperatures of the investigated systems were 84K for Fe impurities and 1250K for subsurface Co atoms. These values are both slightly higher than those reported previously.

Additionally it was shown, that the Kondo specific phase-shift, as observed in the STS-data, is smaller than the expected value of π . A non-resonant background scattering process was proposed as a possible explanation. Using the Green function of the host metal, we extracted the energy dependence of the impurity t -matrix from the STS measurements. Both the scattering amplitude as well as the scattering phase-shift as a function of energy showed signatures of the Kondo-resonance.

Appendix A

Computational details: LCAO

Most of the calculations presented in this thesis were based on the band structure of copper, which was obtained using an *linear combination of atomic orbitals* (LCAO) technique [79, 80]. The idea of LCAO (or *tight-binding*) is to expand the lattice-periodic part $u_{\mathbf{k}}(\mathbf{x})$ of the Bloch functions $\Psi_{\mathbf{k}}(\mathbf{x})$ by wave functions $\phi_{\alpha}(\mathbf{x})$ of atomic orbitals with quantum numbers $\alpha = \{s, p_x, \dots, d_{xy}, \dots\}$

$$\Psi_{\mathbf{k}}(\mathbf{x}) = e^{i\mathbf{k}\mathbf{x}} \cdot u_{\mathbf{k}}(\mathbf{x}) = \sum_{\alpha} v_{\alpha}(\mathbf{k}) \phi_{\alpha}(\mathbf{k}, \mathbf{x}) \quad (\text{A.1})$$

with

$$\varphi_{\alpha}(\mathbf{k}, \mathbf{x}) = e^{i\mathbf{k}\mathbf{x}} \sum_{\mathbf{R}_i} \phi_{\alpha}(\mathbf{x} - \mathbf{R}_i) \quad (\text{A.2})$$

Here \mathbf{R}_i denote the atomic positions and $v_{\alpha}(\mathbf{k})$ are the expansion coefficients, describing whether $\Psi_{\mathbf{k}}(\mathbf{x})$ is for example more "s-like" or "d-like". With the exception of high symmetry points in the Brillouin Zone (e.g. $\Gamma = [000]$) the eigenfunctions in general possess contributions from all these basis states.

Although the atomic orbitals $\phi_{\alpha}(\mathbf{x})$ are orthogonal, this is not valid for the delocalized basis states $\varphi_{\alpha}(\mathbf{k}, \mathbf{x})$. Therefore, the first step is to create an orthogonal set of basis functions for each value of \mathbf{k} . For this, we used Löwdin's method of symmetric orthogonalization [81]. Its purpose is to find a projection Matrix $W(\mathbf{k})$, that maps the initial basis states $\varphi_{\alpha}(\mathbf{k}, \mathbf{x})$ onto an orthogonal and normalized set of basis functions $\varphi'_{\alpha}(\mathbf{k}, \mathbf{x})$ with $\langle \varphi'_{\alpha}(\mathbf{k}) | \varphi'_{\beta}(\mathbf{k}) \rangle = \delta_{\alpha\beta}$.

For this an overlap matrix $S_{\alpha,\beta}(\mathbf{k}) = \langle \varphi_{\alpha}(\mathbf{k}) | \varphi_{\beta}(\mathbf{k}) \rangle$ is calculated and subsequently diagonalized, giving $S = TDT^{-1}$. The diagonal matrix D is used to construct a

matrix $\tilde{D}^{-1/2}$ by replacing each diagonal element of D by its inverse square root. Obviously, this gives:

$$\mathbb{1} = \tilde{D}^{-1/2} D \tilde{D}^{-1/2} = T \tilde{D}^{-1/2} T^{-1} S T \tilde{D}^{-1/2} T^{-1} = W S W \quad (\text{A.3})$$

which yields the required projector $W = T \tilde{D}^{-1/2} T^{-1}$.

The Hamilton matrix $H_{\alpha\beta}(k) = \langle \varphi_\alpha | H | \varphi_\beta \rangle$ calculated using the non-orthogonal basis is then transformed into a new matrix $H_2 = W H W$ and diagonalized $E = V^{-1} H_2 V$. This gives the eigenenergies E and the eigenvectors V (the expansion coefficients) with respect to the new basis. Since the projector W and consequently the new basis is different for each wave-vector \mathbf{k} the eigenvectors V are projected back onto the initial basis, which is the same for all values of \mathbf{k} .

The computation was performed using MATLAB. As this software provides a number of functions for matrix operations, the source code of the procedure described above is very short:

```
[T,D] = eig(S);           % diagonalize Overlap – Matrix S
W = T * (1./sqrt(DS)) * inv(T); % calculate orthonormal Projector W
H2 = W * H * W;         % calculate new Hamiltonian
[V,E] = eig(H2);        % diagonalize new Hamiltonian H2
EV = W * V;             % transfer eigenvector to initial basis
```

The result is a Matrix EV containing the n expansion coefficients of the n eigenfunctions and a matrix E containing the n eigenenergies on its diagonal elements. n is the number of basis functions used for the expansion A.1. In our case we used 1 s-, 3 p- and 5 d-states giving $n=9$.

These calculations requires the knowledge of \mathbf{k} -dependant Hamilton and overlap-matrices $H_{\alpha,\beta}(\mathbf{k})$ and $S_{\alpha,\beta}(\mathbf{k})$. If the crystal potential $V(\mathbf{x})$ and the atomic wave-functions $\phi_\alpha(\mathbf{x})$ are known, these can directly be calculated by:

$$H_{\alpha,\beta}(\mathbf{k}) = \sum_{\mathbf{R}_j} \exp i\mathbf{k}(\mathbf{R}_i - \mathbf{R}_j) \int d^3\mathbf{x} \phi_\alpha^*(\mathbf{x} - \mathbf{R}_i) H \phi_\beta(\mathbf{x} - \mathbf{R}_j) \quad (\text{A.4})$$

$$S_{\alpha,\beta}(\mathbf{k}) = \sum_{\mathbf{R}_j} \exp i\mathbf{k}(\mathbf{R}_i - \mathbf{R}_j) \int d^3\mathbf{x} \phi_\alpha^*(\mathbf{x} - \mathbf{R}_i) \phi_\beta(\mathbf{x} - \mathbf{R}_j) \quad (\text{A.5})$$

Since the integrals in the above equations do not depend on the \mathbf{k} -vector, they can be expressed as a set of material specific *tight-binding parameters* $E_{[xyz]}^{\alpha-\beta}$ and $O_{[xyz]}^{\alpha-\beta}$ for each lattice vector $[xyz] = \mathbf{R}_i - \mathbf{R}_j$ and each combination (α, β) of angular momenta. In this case no detailed knowledge of the atomic wave-functions and the

effective crystal potential is needed. Moreover the value of these parameters can be obtained by fitting the LCAO band-structure to the result of more realistic *ab-initio* calculations.

By numbering the basis states in the following way

$$[s, p_x, p_y, p_z, d_{xy}, d_{yz}, d_{xz}, d_{x^2-y^2}, d_{z^2-r^2}] \quad (\text{A.6})$$

and by including up to second nearest neighbour interactions (i.e. with the lattice vectors $\mathbf{R}_i - \mathbf{R}_j = [000], \frac{1}{2}[110]$ and $[100]$), the required matrix elements for fcc symmetry are:

$$\begin{aligned}
H_{11}(\mathbf{k}) &= E_{[000]}^{s-s} + 4E_{[110]}^{s-s} [\cos k_x \cos k_y + \cos k_y \cos k_z + \cos k_z \cos k_x] \\
&\quad + 2E_{[200]}^{s-s} [\cos 2k_x + \cos 2k_y + \cos 2k_z] \\
H_{12}(\mathbf{k}) &= -4E_{[110]}^{s-x} \sin k_x [\cos k_y + \cos k_z] + 2E_{[200]}^{s-x} \sin 2k_x \\
H_{13}(\mathbf{k}) &= -4E_{[110]}^{s-x} \sin k_y [\cos k_x + \cos k_z] + 2E_{[200]}^{s-x} \sin 2k_y \\
H_{14}(\mathbf{k}) &= -4E_{[110]}^{s-x} \sin k_z [\cos k_y + \cos k_x] + 2E_{[200]}^{s-x} \sin 2k_z \\
H_{15}(\mathbf{k}) &= -4E_{[110]}^{s-xy} \sin k_x \sin k_y \\
H_{16}(\mathbf{k}) &= -4E_{[110]}^{s-xy} \sin k_y \sin k_z \\
H_{17}(\mathbf{k}) &= -4E_{[110]}^{s-xy} \sin k_z \sin k_x \\
H_{18}(\mathbf{k}) &= 2\sqrt{3}E_{[110]}^{s-d_2} \cos k_z [\cos k_y - \cos k_x] + \sqrt{3}E_{[002]}^{s-d_2} [\cos 2k_x - \cos 2k_y] \\
H_{19}(\mathbf{k}) &= -2E_{[110]}^{s-d_2} [-2 \cos k_x \cos k_y + \cos k_y \cos k_z + \cos k_z \cos k_x] \\
&\quad + E_{[002]}^{s-d_2} [-\cos 2k_x - \cos 2k_y + 2 \cos 2k_z] \\
H_{22}(\mathbf{k}) &= E_{[000]}^{x-x} + 4E_{[110]}^{x-x} \cos k_x [\cos k_y + \cos k_z] + 4E_{[011]}^{x-x} \cos k_y \cos k_z \\
&\quad + 2E_{[200]}^{x-x} \cos 2k_x + 2E_{[200]}^{xy} [\cos 2k_y + \cos 2k_z] \\
H_{23}(\mathbf{k}) &= -4E_{[110]}^{x-y} \sin k_x \sin k_y \\
H_{24}(\mathbf{k}) &= -4E_{[110]}^{x-y} \sin k_x \sin k_z \\
H_{25}(\mathbf{k}) &= 4 \sin k_y [E_{[110]}^{x-xy} \cos k_x + E_{[011]}^{x-xy} \cos k_z] + 2E_{[020]}^{x-xy} \sin 2k_y \\
H_{26}(\mathbf{k}) &= 0 \\
H_{27}(\mathbf{k}) &= 4 \sin k_z [E_{[110]}^{x-xy} \cos k_x + E_{[011]}^{x-xy} \cos k_y] + 2E_{[020]}^{x-xy} \sin 2k_z \\
H_{28}(\mathbf{k}) &= 2\sqrt{3}E_{[011]}^{z-d_2} \sin k_x [\cos k_y + \cos k_z] + \sqrt{3}E_{[002]}^{z-d_2} \sin 2k_x \\
&\quad + 2E_{[011]}^{z-d_1} \sin k_x [\cos k_y - \cos k_z] \\
H_{29}(\mathbf{k}) &= -2E_{[011]}^{z-d_2} \sin k_x [\cos k_y + \cos k_z] - E_{[002]}^{z-d_2} \sin 2k_x \\
&\quad + 2\sqrt{3}E_{[011]}^{z-d_1} \sin k_x [\cos k_y - \cos k_z] \\
H_{34}(\mathbf{k}) &= -4E_{[110]}^{x-y} \sin k_y \sin k_z \\
H_{35}(\mathbf{k}) &= 4 \sin k_x [E_{[110]}^{x-xy} \cos k_y + E_{[011]}^{x-xy} \cos k_z] + 2E_{[020]}^{x-xy} \sin 2k_x \\
H_{36}(\mathbf{k}) &= 4 \sin k_z [E_{[110]}^{x-xy} \cos k_y + E_{[011]}^{x-xy} \cos k_x] + 2E_{[020]}^{x-xy} \sin 2k_z \\
H_{37}(\mathbf{k}) &= 0 \\
H_{38}(\mathbf{k}) &= -2\sqrt{3}E_{[011]}^{z-d_2} \sin k_y [\cos k_z + \cos k_x] - \sqrt{3}E_{[002]}^{z-d_2} \sin 2k_y \\
&\quad - 2E_{[011]}^{z-d_1} \sin k_y [\cos k_x - \cos k_z]
\end{aligned}$$

$$\begin{aligned}
H_{39}(\mathbf{k}) &= -2E_{[011]}^{z-d_2} \sin k_y [\cos k_z + \cos k_x] - E_{[002]}^{z-d_2} \sin 2k_y \\
&\quad - 2\sqrt{3}E_{[011]}^{z-d_1} \sin k_y [\cos k_z - \cos k_x] \\
H_{44}(\mathbf{k}) &= E_{[000]}^{x-x} + 4E_{[110]}^{x-x} \cos k_z [\cos k_x + \cos k_y] + 4E_{[011]}^{x-x} \cos k_x \cos k_y \\
&\quad + 2E_{[200]}^{x-x} \cos 2k_z + 2E_{yy[200]} [\cos 2k_x + \cos 2k_y] \\
H_{45}(\mathbf{k}) &= 0 \\
H_{46}(\mathbf{k}) &= 4 \sin k_y [E_{[110]}^{x-xy} \cos k_z + E_{[011]}^{x-xy} \cos k_x] + 2E_{[020]}^{x-xy} \sin 2k_y \\
H_{47}(\mathbf{k}) &= 4 \sin k_x [E_{[110]}^{x-xy} \cos k_z + E_{[020]}^{x-xy} \cos k_y] + 2E_{[020]}^{x-xy} \sin 2k_x \\
H_{48}(\mathbf{k}) &= 4E_{[011]}^{z-d_1} \sin k_z [\cos k_y - \cos k_x] \\
H_{49}(\mathbf{k}) &= 4E_{[011]}^{z-d_2} \sin k_z [\cos k_y + \cos k_x] + 2E_{[002]}^{z-d_2} \sin 2k_z \\
H_{55}(\mathbf{k}) &= E_{[000]}^{xy-xy} + 4E_{[110]}^{xy-xy} \cos k_x \cos k_y + 4E_{[011]}^{xy-xy} \cos k_z [\cos k_x + \cos k_y] \\
&\quad + 2E_{[200]}^{xy-xy} [\cos 2k_x + \cos 2k_y] + 2E_{[002]}^{xy-xy} \cos 2k_z \\
H_{56}(\mathbf{k}) &= -4E_{[011]}^{xy-xz} \sin k_x \sin k_z \\
H_{57}(\mathbf{k}) &= -4E_{[011]}^{xy-xz} \sin k_y \sin k_z \\
H_{58}(\mathbf{k}) &= 0 \\
H_{59}(\mathbf{k}) &= -4E_{[110]}^{xy-d_2} \sin k_x \sin k_y \\
H_{66}(\mathbf{k}) &= E_{[000]}^{xy-xy} + 4E_{[110]}^{xy-xy} \cos k_y \cos k_z + 4E_{[011]}^{xy-xy} \cos k_x [\cos k_y + \cos k_z] \\
&\quad + 2E_{[200]}^{xy-xy} [\cos 2k_z + \cos 2k_y] + 2E_{[002]}^{xy-xy} \cos 2k_x \\
H_{67}(\mathbf{k}) &= -4E_{[011]}^{xy-xz} \sin k_x \sin k_y \\
H_{68}(\mathbf{k}) &= -2\sqrt{3}E_{[110]}^{xy-d_2} \sin k_y \sin k_z \\
H_{69}(\mathbf{k}) &= 2E_{[110]}^{xy-d_2} \sin k_y \sin k_z \\
H_{77}(\mathbf{k}) &= E_{[000]}^{xy-xy} + 4E_{[110]}^{xy-xy} \cos k_x \cos k_z + 4E_{[011]}^{xy-xy} \cos k_y [\cos k_x + \cos k_z] \\
&\quad + 2E_{[200]}^{xy-xy} [\cos 2k_x + \cos 2k_z] + 2E_{[002]}^{xy-xy} \cos 2k_y \\
H_{78}(\mathbf{k}) &= 2\sqrt{3}E_{[110]}^{xy-d_2} \sin k_x \sin k_z \\
H_{79}(\mathbf{k}) &= 2E_{[110]}^{xy-d_2} \sin k_x \sin k_z \\
H_{88}(\mathbf{k}) &= E_{[000]}^{d_2-d_2} + 3E_{[110]}^{d_2-d_2} \cos k_z [\cos k_x + \cos k_y] + 4E_{[110]}^{d_1-d_1} [\cos k_x \cos k_y \\
&\quad + \cos k_x \cos k_z/4 + \cos k_y \cos k_z/4] + (3/2)E_{[002]}^{d_2-d_2} [\cos 2k_x + \cos 2k_y] \\
&\quad + 2E_{[002]}^{d_1-d_1} [\cos 2k_x/4 + \cos 2k_y/4 + \cos 2k_z] \\
H_{89}(\mathbf{k}) &= \sqrt{3} \cos k_z [\cos k_x - \cos k_y] (E_{[110]}^{d_2-d_2} - E_{[110]}^{d_1-d_1}) \\
&\quad + \sqrt{3}/2 [\cos 2k_y - \cos 2k_x] (E_{[002]}^{d_2-d_2} - E_{[002]}^{d_1-d_1}) \\
H_{99}(\mathbf{k}) &= E_{[000]}^{d_2-d_2} + 4E_{[110]}^{d_2-d_2} [\cos k_x \cos k_y + \cos k_x \cos k_z/4 + \cos k_y \cos k_z/4] \\
&\quad + 3E_{[110]}^{d_1-d_1} \cos k_z [\cos k_x + \cos k_y] + (3/2)E_{[002]}^{d_1-d_1} [\cos 2k_x + \cos 2k_y] \\
&\quad + 2E_{[002]}^{d_2-d_2} [\cos 2k_x/4 + \cos 2k_y/4 + \cos 2k_z]
\end{aligned}$$

The lower triangular matrix can be padded using $H_{\alpha,\beta}(\mathbf{k}) = H_{\beta,\alpha}(\mathbf{k})^*$. The overlap matrix $S_{\alpha,\beta}$ is obtained similar to the above by replacing the parameters $E_{[xyz]}^{\alpha-\beta}$ in the equations by $O_{[xyz]}^{\alpha-\beta}$. The required integrals $X_{[xyz]}^{\alpha-\beta}$ ($X = E, O$) in the above matrix elements were taken from [46]. For the case of copper they are:

	Energy [Ry] $X = E$	Overlap $X = O$
On Site		
$X_{[000]}^{s-s}$	0,60246	1
$X_{[000]}^{x-x}$	1,22779	1
$X_{[000]}^{xy-xy}$	0,37675	1
$X_{[000]}^{d2-d2}$	0,37520	1
First Neighbour		
$X_{[110]}^{s-s}$	-0.05801	0.08495
$X_{[110]}^{s-x}$	0.04580	-0.08397
$X_{[110]}^{s-xy}$	-0.03557	0.00492
$X_{[110]}^{s-d2}$	0.02037	0.00966
$X_{[110]}^{x-x}$	0.07153	-0.05392
$X_{[011]}^{x-x}$	0.06447	0.06951
$X_{[110]}^{x-y}$	-0.01376	-0.12072
$X_{[110]}^{x-xy}$	-0.03287	-0.00862
$X_{[011]}^{x-xy}$	-0.01085	-0.06060
$X_{[011]}^{z-d2}$	-0.01180	-0.06334
$X_{[110]}^{z-d1}$	0.01291	-0.01291
$X_{[110]}^{xy-xy}$	-0.01429	0.01400
$X_{[011]}^{xy-xy}$	0.00421	-0.00696
$X_{[011]}^{xy-xz}$	0.00315	-0.01384
$X_{[110]}^{xy-d2}$	0.01009	0.00006
$X_{[110]}^{d2-d2}$	0.00069	0.02228
$X_{[110]}^{d1-d1}$	0.01766	0.00209
Second Neighbour		
$X_{[200]}^{s-s}$	-0.02041	-0.00003
$X_{[200]}^{s-x}$	0.05037	0.00468
$X_{[002]}^{s-d2}$	-0.01651	-0.02370
$X_{[200]}^{x-x}$	0.13434	0.03163
$X_{[200]}^{y-y}$	0.03834	0.02838
$X_{[020]}^{x-xy}$	-0.01329	-0.03333
$X_{[002]}^{z-d2}$	-0.04240	-0.07768
$X_{[200]}^{xy-xy}$	-0.00150	-0.00499
$X_{[002]}^{xy-xy}$	-0.00126	-0.00235
$X_{[002]}^{d2-d2}$	-0.00484	-0.00218
$X_{[002]}^{d1-d1}$	0.00116	0.00519

The laborious part of the LCAO method is typing in all these Matrix elements and material specific parameters. But as this technique only deals with 9×9 -matrices the calculation of the eigenenergies and eigenvectors is very fast giving approximately 6000 k-points/sec. Moreover, since the above energy- and overlap integrals were determined by fitting the LCAO band-structures to the results of more accurate *ab-initio* calculations, they provide realistic information. For the 6th-band, which we are particularly interested in because it is the one that crosses the Fermi-level, the RMS deviation from *ab-initio* results is 7 meV and the maximum error is 15 meV.

The band-structure of copper obtained by this method is depicted in Figure A.1. With colors we represented the corresponding "character" of the wave functions ($s = |v_1(\mathbf{k})|^2$, $p = \sum_{\alpha=2}^4 |v_\alpha(\mathbf{k})|^2$, $t2_g = \sum_{\alpha=5}^7 |v_\alpha(\mathbf{k})|^2$, $e_g = \sum_{\alpha=8}^9 |v_\alpha(\mathbf{k})|^2$). Here it can be seen that the parabolic band around $-9eV$ has mainly s-character while the so called "d-bands" emerge between $-2eV$ and $-4eV$ and show a strong crystal-field splitting.

The fcc-Brillouin zone is invariant under various symmetry transformations. It is sufficient to restrict the calculation to the irreducible part of the first Brillouin zone (IFBZ) and transform every \mathbf{k} into the other regions using the 48 matrices:

$$M_x = \begin{pmatrix} -1 & 0 & 0 \\ 0 & 1 & 0 \\ 0 & 0 & 1 \end{pmatrix}^a \cdot \begin{pmatrix} 1 & 0 & 0 \\ 0 & -1 & 0 \\ 0 & 0 & 1 \end{pmatrix}^b \cdot \begin{pmatrix} 1 & 0 & 0 \\ 0 & 1 & 0 \\ 0 & 0 & -1 \end{pmatrix}^c \cdot \begin{pmatrix} 0 & 0 & 1 \\ 0 & 1 & 0 \\ 1 & 0 & 0 \end{pmatrix}^d \cdot \begin{pmatrix} 0 & 0 & 1 \\ 1 & 0 & 0 \\ 0 & 1 & 0 \end{pmatrix}^e \quad (\text{A.7})$$

with $a, b, c, d \in \{0, 1\}$ and $e \in \{0, 1, 2\}$. The first three matrices in the above equation are reflections at the x-, y-, and z-plane, respectively. The fourth matrix is a $(10\bar{1})$ -reflection and the last term a 120° -rotation around $[111]$. With the help of this procedure the computational time of a Fermi-surface calculation can be reduced to $1/48$.

Within the IFBZ a specialized grid of directions was used. It is derived from spherical coordinates with the zenith oriented in $[111]$ -direction and distorted properly to cover the IFBZ. This is depicted in Figure A.2. First, the opening angle $\theta_{neck}(\varepsilon)$ of the $[111]$ -"neck" was determined for the particular energy by performing the band structure calculation along a line $L \rightarrow U$. For $n \times m$ points in the IFBZ with $u = 1 \dots n$, $v = 1 \dots m$ we used the zenith angles:

$$\theta(u, v) = \frac{\pi}{2} - \theta_{neck} - \frac{u-1}{n-1} \left(\arccos \left(\sqrt{\frac{2}{3 - 2 \tan^2 \left(\frac{v-1}{m-1} \cdot \frac{\pi}{3} \right)}} \right) - \theta_{neck} \right) \quad (\text{A.8})$$

and the azimuth angle:

$$\varphi(u, v) = \frac{3\pi}{2} + \frac{v-1}{m-1} \cdot \frac{\pi}{3} \quad (\text{A.9})$$

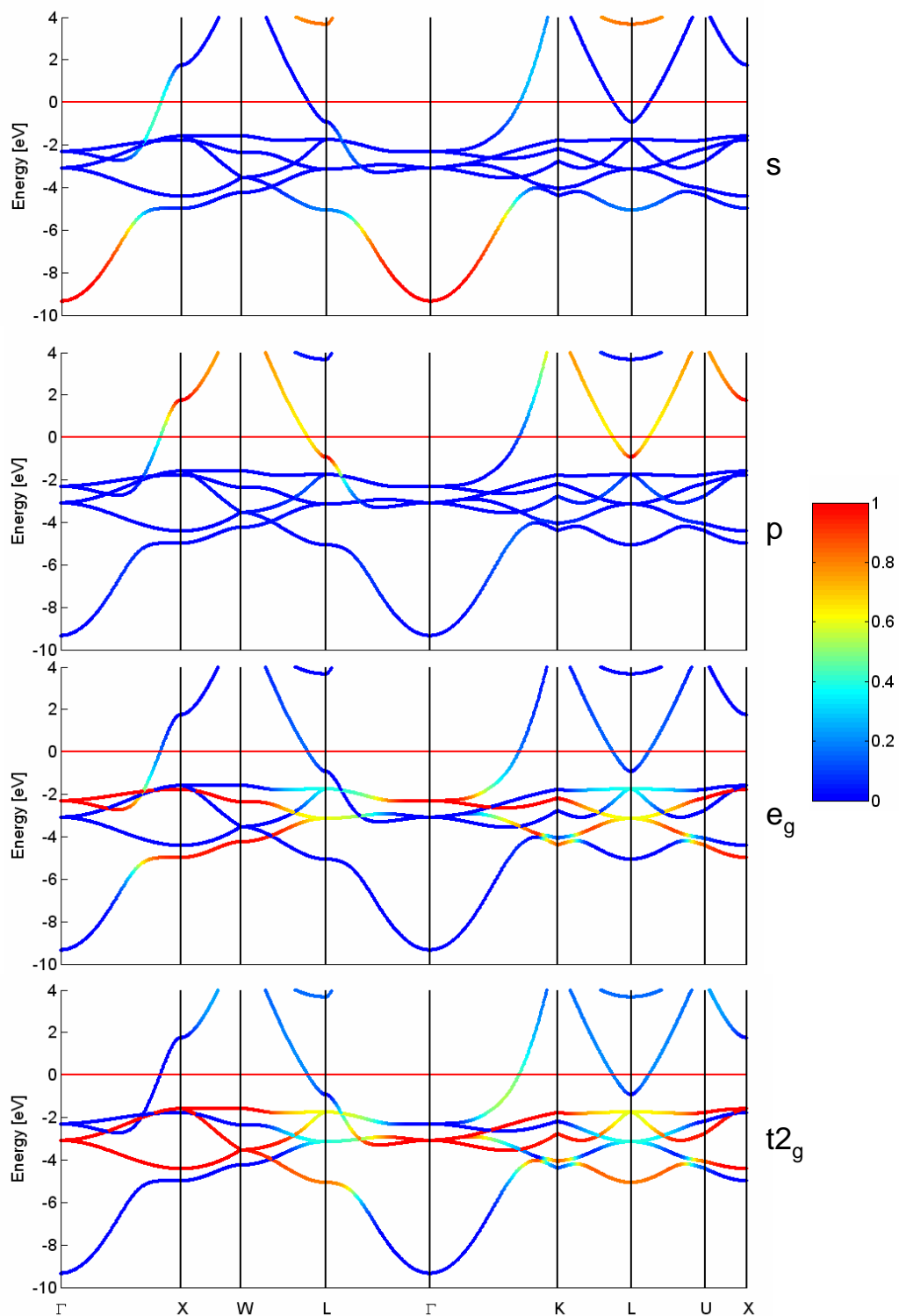


Figure A.1: Band structure of copper calculated using the LCAO technique. The "character" of wave-functions is represented with colors.

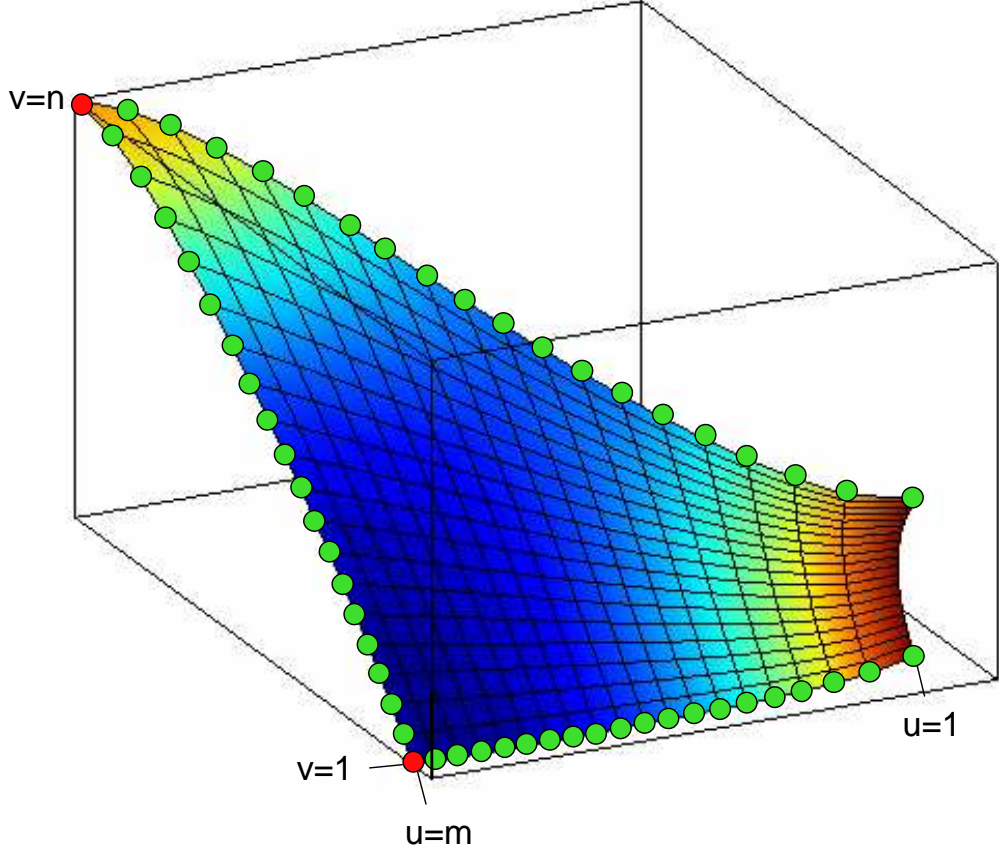


Figure A.2: Grid of directions in the IBZ used for the computation of the fcc-Fermi surfaces. Red and green dots mark grid points whose area has to be reduced to $1/4$ and $1/2$, respectively.

For every direction within the IBZ a zero-finding routine based on Newton's method was used to determine the length of the \mathbf{k} -vector that satisfies $E(\mathbf{k}) - \varepsilon = 0$. This gives a contour $\mathbf{k}(u, v) = [k_x(u, v), k_y(u, v), k_z(u, v)]$ for which the normal vector was determined at each point. In direction of the normal vector the slope of dispersion $|\mathbf{v}_{Gr}|(u, v)$ was calculated. Furthermore, the Jacobi-determinant $J(u, v)$ describing the area of each grid "tile" was extracted. When assembling the Fermi surface from the 48 parts it has to be considered that \mathbf{k} -points located at the edges (green dots in Fig. A.2) and vertices (red dots in Fig. A.2) of the fragments overlap with those of neighbouring cells. Thus, their area $J(u, v)$ has to be divided by 2 and 4, respectively.

The total density of states can then easily be obtained from the area of the Fermi

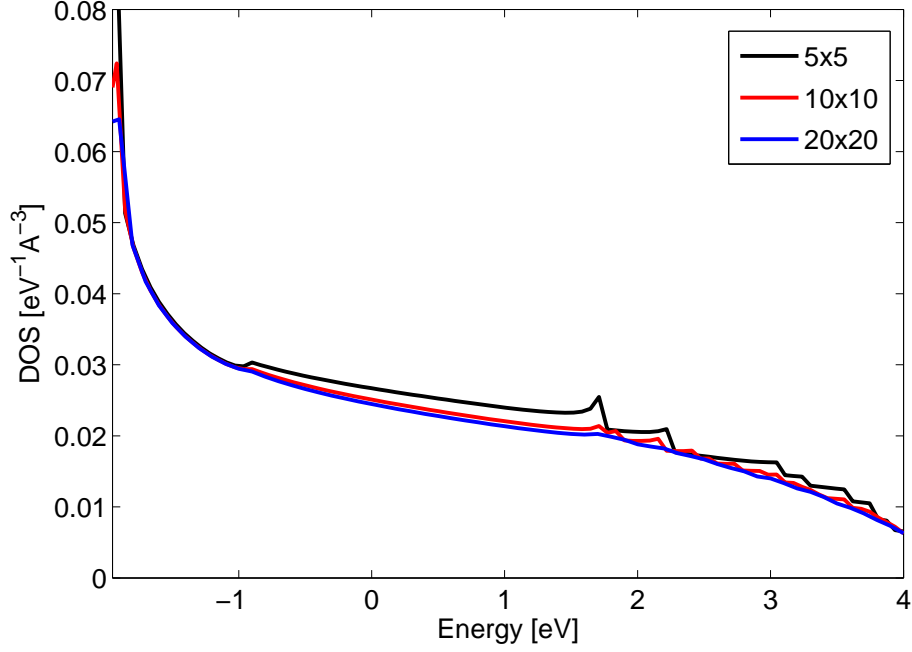


Figure A.3: Total density of states calculated using different grid sizes within IFBZ. The ripples above $+1.6\text{eV}$ are due to the emergence of a $[100]$ pseudo band-gap and the consequent "flaking" of single grid "tiles".

surface and the group velocities:

$$DOS(\varepsilon) = 48 \cdot \frac{2}{(2\pi)^3} \cdot \sum_{u,v} \frac{J(u,v)}{|\mathbf{v}_{Gr}(u,v)|} \quad (\text{A.10})$$

The result for different grid-sizes can be seen in Figure A.3. The result is a smooth function within $\pm 1\text{V}$ while irregularities can be observed above $+1.6\text{V}$. These are due to an emerging pseudo band-gap in $[100]$ -direction. These artifacts become less obvious if the grid-size is increased.

The required computation time for a 10×10 -grid is $\approx 15\text{ s}$. The calculations presented in this work were performed using 20×20 points in the IFBZ although the result of the LDOS calculations do not differ markedly from those calculated using a 10×10 grid.

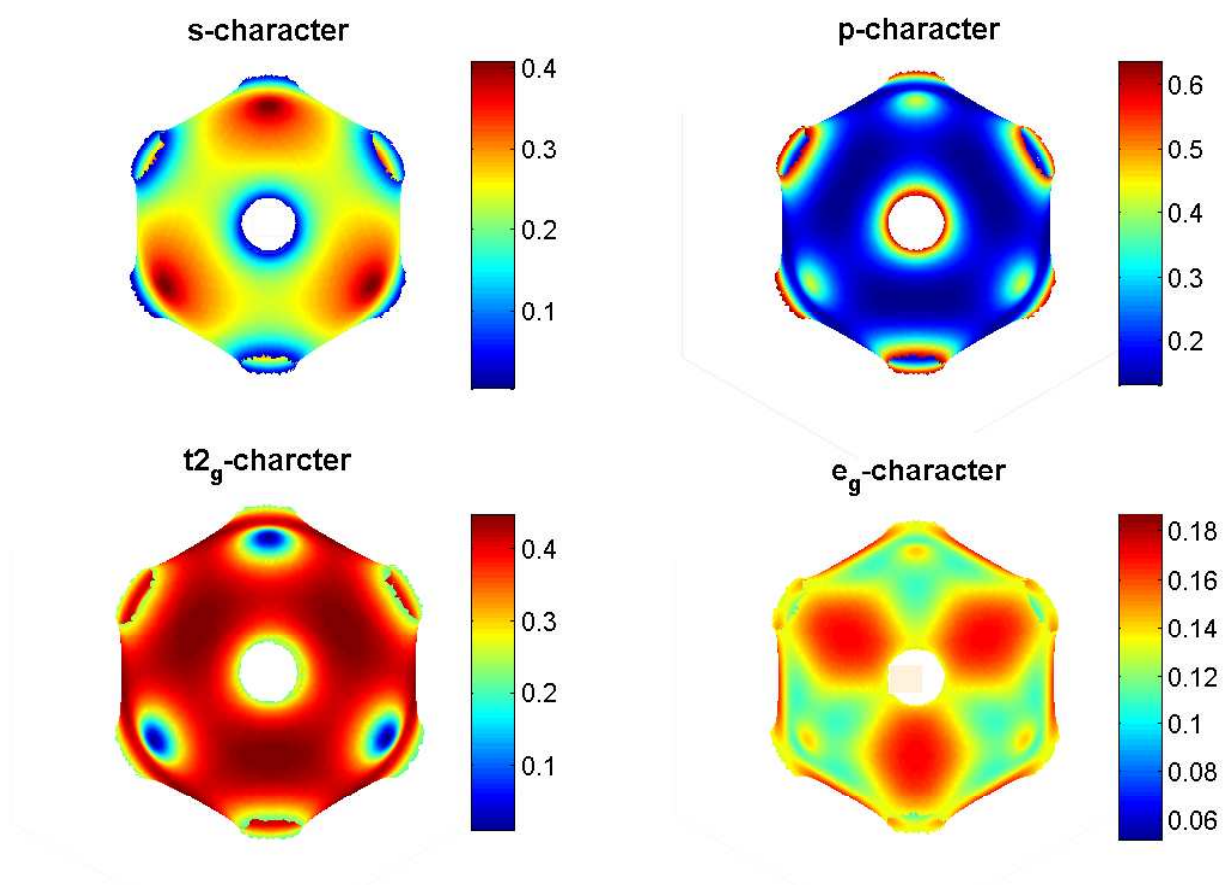


Figure A.4: Fermi-surfaces calculated using the LCAO technique. The "character" of wave-functions is represented on the Fermi-surfaces with colors.

Appendix B

The real part of G_0

When the relationship between the propagation of electrons within the host material and the geometry of the Fermi-surface was explained in Chapter 3, we restricted the discussion to that of the imaginary part of $G_0(\mathbf{x}, \mathbf{x}', \varepsilon)$ and assumed that (within a band) the real part shows the identical characteristics concerning e.g. wavelength and directional dependency. Later, when the local density of states in certain distances from the impurity was computed, we used the full Green function without describing the calculation details of how the real part was obtained. This lengthy discussion was avoided for sake of readability and we want to make up for further explanations here.

In spectral representation, the Green function can be obtained by integration of \mathbf{k} -states within the first Brillouin-zone [17, 12]:

$$G_0(\mathbf{x}, \mathbf{x}', \varepsilon) = \lim_{\eta \rightarrow 0} \sum_{\nu} \int_{FBZ} d^3k \frac{\Psi_{\mathbf{k},\nu}(\mathbf{x}) \Psi_{\mathbf{k},\nu}^*(\mathbf{x}')}{\varepsilon - E(\mathbf{k}, \nu) + i\eta} \quad (\text{B.1})$$

Here the band-index ν was included to show that in general the integration has to be performed using a complete set of states. This includes multiple bands and states $\Psi_{\mathbf{k},\nu}(\mathbf{x})$ whose energies $E(\mathbf{k}, \nu)$ may differ strongly from the energy of interest ε . While it can be shown using the residue theorem that for the imaginary part only states with $E(\mathbf{k}) = \varepsilon$ are of importance, one obtains an expression for the real part that contains the principal value of the above intergral:

$$\text{Re}G_0(\mathbf{x}, \mathbf{x}', \varepsilon) = \mathcal{P} \int_{FBZ} d^3k \frac{\Psi_{\mathbf{k},\nu}(\mathbf{x}) \Psi_{\mathbf{k},\nu}^*(\mathbf{x}')}{\varepsilon - E(\mathbf{k}, \nu)} \quad (\text{B.2})$$

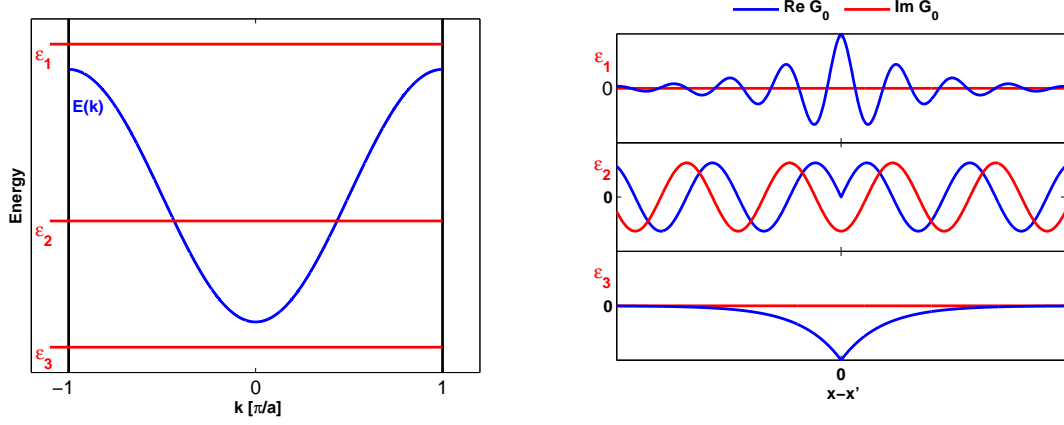


Figure B.1: : Propagators for certain energies: for ϵ outside the band (ϵ_1, ϵ_3) $\text{Im } G_0$ vanishes while $\text{Re } G_0$ shows evanescent behavior. For energies inside the continuum (ϵ_2) both parts differ only in a $\pi/2$ phase shift.

This again requires all k -states and the full band structure $E(k, \nu)$. A last possibility to access $\text{Re } G_0$ is to use the *Kramers-Kronig relation*[47, 48]:

$$\text{Re } G_0(\mathbf{x}, \mathbf{x}', \epsilon) = \frac{1}{\pi} \mathcal{P} \int_{-\infty}^{\infty} d\epsilon' \frac{\text{Im } G_0(\mathbf{x}, \mathbf{x}', \epsilon')}{\epsilon - \epsilon'} \quad (\text{B.3})$$

which allows to obtain the real part by integrating the imaginary part over an infinite energy range. In all these cases, states within a large energy interval are necessary for the calculation of $\text{Re } G_0$.

From the above information it seems to be not justified to derive any properties of the real part only from that states having $E(\mathbf{k}) = \epsilon$ (i.e. form the iso-energy surface $\Omega(\epsilon)$) or to assume any "similarity" between $\text{Re } G_0$ and $\text{Im } G_0$ as it was done in Chapter 3. We will now show that such a similarity does not exist in general but can be assumed if the energy ϵ lies within a continuum of states. For this we will use a simple, 1-dimensional example to demonstrate the connection between the real and imaginary part of the propagator in various energy regimes. This is depicted in Figure B.1 using a cosine-shaped band structure $E(k) = -\frac{W}{2} \cos ka$.

If ϵ is chosen outside a band continuum ($|\epsilon| > \frac{W}{2}$, which corresponds to energies ϵ_1 and ϵ_3 in Figure. B.1), the imaginary part of the propagator is zero. This is obvious for two reasons: i) the density of states $\varrho_0(\epsilon)$ that can be derived from $\text{Im } G_0$, vanishes at these energies and ii) $\text{Im } G_0$ can solely be obtained from an integration over the iso-energy surface $\Omega(\epsilon)$, which does not exist within a band-gap. However, the real part of G_0 is non-zero for these energies and shows an *evanescent* character.

It is exponentially damped and shows similarities to those band-states which are closest in energy: it is non-oscillatory damped for ε_3 being closest to states having $k = 0$ and shows damped oscillations for ε_3 being near to states with $k = \pi/a$. The real part for these energies contains all information about possible localized states that *may* emerge in the vicinity of defects (impurities, interfaces, surfaces) if their corresponding T-matrix has a non-zero imaginary part. In other words with $G_0 \in \mathbb{R}$ and $\text{Im } t \neq 0$ the perturbed system would show a localized density of states $\text{Im } G = \text{Im}[G_0 t G_0] \neq 0$ within the band gap.¹

This example illustrates, that it is in general **not** possible to obtain $\text{Re } G_0(\varepsilon)$ from $\text{Im } G_0(\varepsilon)$ at the identical energy ε or from the iso-energy surface $\Omega(\varepsilon)$. Furthermore it demonstrates that the real part is influenced by states that are in energetic proximity. As was shown on the above equations one needs the full band-structure to compute $\text{Re } G_0$ for an arbitrary energy. But in the case of $|\varepsilon| < \frac{W}{2}$ (ε_2 in Fig. B.1) where ε is chosen inside a continuum of band states, the quantities $\text{Re } G_0$ and $\text{Im } G_0$ have substantial similarity. They both show identical wavelength $\lambda = 2\pi/k(\varepsilon_2)$ and spatial envelope but differ in a $\pi/2$ shift of the real part towards the position of the source \mathbf{x}' . In this case the question arises whether it is really necessary to perform a time-consuming integration over a large energy range if the Green function is required only for energies inside a continuum of band states. Without giving mathematical proof we now present a method that was found empirically. It performs an approximation of $\text{Re } G_0(\varepsilon)$ from the iso-energy surface $\Omega(\varepsilon)$. The method is exact for the case of a free electron in three dimensions and this physical system will also be used to introduce the procedure.

The iso-energy surfaces of a 3-dimensional free electron gas are spheres with radius $k(\varepsilon) = \hbar^{-1}\sqrt{2m\varepsilon}$. As discussed in chapter 3, the corresponding propagator is a spherical wave decaying with $|\mathbf{x} - \mathbf{x}'|^{-1}$ in amplitude:

$$G_0(\mathbf{x}, \mathbf{x}', \varepsilon) = \pi \varrho_0(\varepsilon) \left(\frac{\cos(k(\varepsilon)|\mathbf{x} - \mathbf{x}'|)}{k(\varepsilon)|\mathbf{x} - \mathbf{x}'|} - i \frac{\sin(k(\varepsilon)|\mathbf{x} - \mathbf{x}'|)}{k(\varepsilon)|\mathbf{x} - \mathbf{x}'|} \right) \quad (\text{B.4})$$

Its imaginary and real parts are also proportional to the regular and irregular solution of the radial Schroedinger equation for zero angular momentum. The superposition

$$-i\pi \sum_{\mathbf{k} \in \Omega(\varepsilon)} \frac{J(\mathbf{k})}{|v_{Gr}(\mathbf{k})|} e^{i\mathbf{k}(\mathbf{x}-\mathbf{x}')} \quad (\text{B.5})$$

¹These localized wave functions are sometimes associated with non-normalizable continuum states having a complex k-vector ("*complex band structure*"). The above example however shows, that the continuum wave-functions of real k-value and their (real) band structure $E(\mathbf{k})$ are sufficient for the physical description of these evanescent states.

of all states $|\mathbf{k}\rangle = \exp(i\mathbf{k}\mathbf{x})$ lying on the iso-energy surface, as done throughout the thesis, yields only the regular solution i.e. an expression $\propto \sin(k|\mathbf{x} - \mathbf{x}'|)/(k|\mathbf{x} - \mathbf{x}'|)$. The reason for that is the inversion symmetry of the iso-energy surfaces. Every state $|\mathbf{k}\rangle$ on the iso-energy surface has its counterpart $|\mathbf{-k}\rangle$ so that the antisymmetric part of the wave-functions cancels out during the integration. This can be avoided by replacing the exponent of the wave functions by its absolute value giving $|\tilde{\mathbf{k}}\rangle = \exp(i|\mathbf{k}\mathbf{x}|)$. This leaves the imaginary part unchanged but provides a "preliminary" real part whose physical meaning is first of all unclear. In the case of the 3-dimensional free electron gas the superposition of all these modified wave functions $|\tilde{\mathbf{k}}\rangle$ yields an expression which is "nearly" the exact Green function:

$$\tilde{G}_0(\mathbf{x}, \mathbf{x}', \varepsilon) = \pi \varrho_0(\varepsilon) \left(\frac{\cos(k(\varepsilon)|\mathbf{x} - \mathbf{x}'|) + 1}{k(\varepsilon)|\mathbf{x} - \mathbf{x}'|} - i \frac{\sin(k(\varepsilon)|\mathbf{x} - \mathbf{x}'|)}{k(\varepsilon)|\mathbf{x} - \mathbf{x}'|} \right) \quad (\text{B.6})$$

Its real part shows the correct oscillatory behavior and decay but is shifted upwards compared to the exact expression by a smooth, non-oscillatory function $\propto 1/(k|\mathbf{x} - \mathbf{x}'|)$. A comparison of the correct real part and the one obtained by the above expression is depicted in figure B.2. This figure also shows, that if ReG_0 is not calculated correctly, the absolute value of the Green function shows unphysical oscillations.

If this procedure is performed using the Fermi surface of copper the identical effect can be observed. The preliminary real part looks appropriate but it is shifted upwards and is "not aligned" with the imaginary part. Hence, if one finds a correction function (the difference between the preliminary and the exact real part) that properly "pulls down" the calculated real part, this would allow to calculate the full Green function from the iso-energy surface. In the case of copper the correction function of the isotropic case ($\propto |\mathbf{x} - \mathbf{x}'|^{-1}$) seems to apply well so that the following approximation showed to be appropriate:

$$G_0(\mathbf{x} - \mathbf{x}', \varepsilon) \approx -i\pi \sum_{\mathbf{k} \in \Omega(\varepsilon)} \frac{J(\mathbf{k})}{|v_{Gr}(\mathbf{k})|} |a(\mathbf{k})| \left[e^{i|\mathbf{k}(\mathbf{x} - \mathbf{x}') + \phi(a(\mathbf{k}))|} - \frac{i}{|\mathbf{k}||\mathbf{x} - \mathbf{x}'|} \right] \quad (\text{B.7})$$

here a complex pre-factor $a(\mathbf{k})$ having phase $\phi(a(\mathbf{k})) = \arctan(\text{Im}a(\mathbf{k})/\text{Re}a(\mathbf{k}))$ was included. This pre-factor can be the reflection/transmission coefficients of section 3.4.2 that were used to calculate G_0^{CV} and G_0^{VV} .

Several attempts have been made to find the exact correction-function for an arbitrary Fermi-surface. One idea is depicted in figure B.2: the positions directly between the zero crossings of the imaginary part are determined. At these positions, the values of the preliminary real part (indicated by black arrows in fig. B.2) define, how much $Re\tilde{G}_0$ has to be "pulled down" in order to match with ReG_0 . The

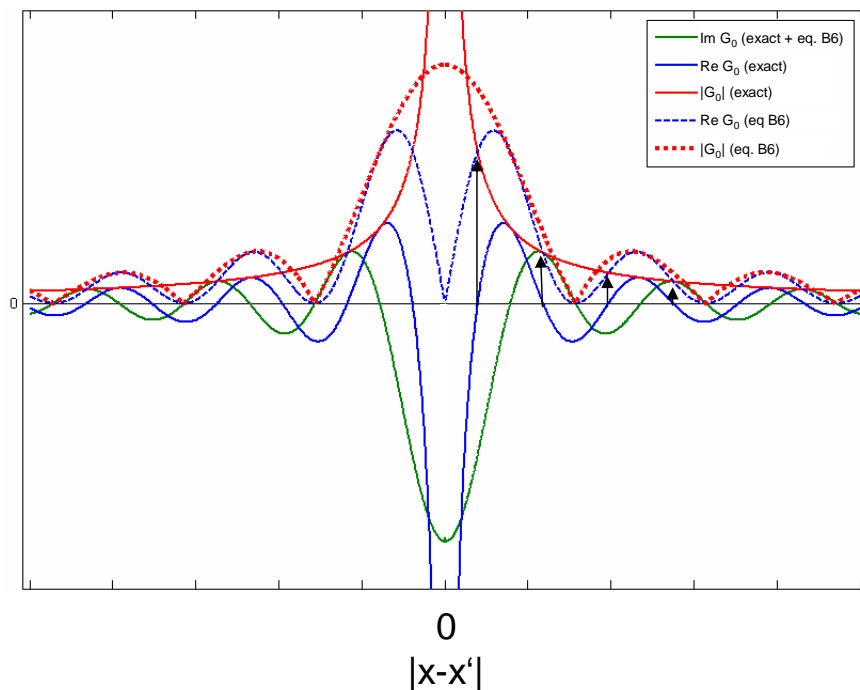


Figure B.2: *Exact and "preliminary" Green functions of a 3-dimensional free electron gas*

values of the correction function for other positions can be obtained by interpolation. However, the realization of such a procedure in three dimensions turned out to be much more complicated. Since equation B.7 gives satisfactory results at least for the case of copper, these efforts were not continued. Finally we used two different methods for the calculation of $\text{Re}G_0$ depending on how important the accuracy of the result has been:

For the fitting of the constant current topographies, the simulation of spectra sections and for the experimental determination of the t-matrix, it is of great importance that the real part is calculated correctly and that it is free of artifacts. In these cases G_0 was required only along one lateral dimension so that the calculations are less time-consuming. Here the real part was calculated using the Kramers-Kronig relation by integration over a large energy range. For this, we used $\text{Im}G_0(h, d, x, \varepsilon)$ for energies between -2.3V and +4V with an energetic step-size of 25mV. This produces good results but takes some time. For the calculation of two-dimensional LDOS-maps or whenever a rough estimations of G_0 was sufficient, the real part was approximated using equation B.7. By this, the simulation of a STM-topography takes less than one minute including the LCAO-calculation of the Fermi surface (10x10 points in the IFBZ) and the subsequent integration in order to obtain G_0 .

Appendix C

List of Abbreviations

$f * g$	convolution of two functions f and g
c_λ	fermionic destructor of state λ
c_λ^\dagger	fermionic constructor of state λ
d	depth of the impurity below the surface
ε	energy
ϵ_d	energy of d-orbital
ϵ_F	Fermi-energy
$E(\mathbf{k})$	band structure
FWHM	full width half maximum
FS	Fermi surface = $\Omega(\epsilon_F)$
G	Propagator
G_0	Propagator of the unperturbed system
G_{dd}	d-orbital Green function
h	height of the tip above the surface
HWHM	half width half maximum
I	(tunnelling) current
I_{Em}	emission current
I_{Fil}	filament current
I_T	set-point (tunnelling) current
J	Jacobi determinant
K	principal curvature
κ	decay constant
k_B	Boltzmann-constant $8.62 * 10^{-5} eV/K$
LCAO	linear combination of atomic orbitals
LDOS	local density of states
LHe	liquid helium
LN_2	liquid nitrogen

n_d	d-level occupation number
N_d	degeneracy of the d-orbital
ω	angular frequency
$\Omega(\epsilon)$	iso-energy surface for energy ϵ
\mathcal{P}	principal value
φ	azimuth angle
$\phi(a)$	phase of a complex number a ($\equiv \arctan(\text{Im}a/\text{Re}a)$)
ϕ	scattering phase-shift ($= \phi(t_{imp})$)
ϕ_q	q-phase of Fano-lineshapes $\phi_q = 2 \cdot \arctan(q)$
$\Psi_{\mathbf{k}}(\mathbf{x})$	Bloch wavefunction
q	Fano asymmetry parameter
$\varrho(\mathbf{x}, \epsilon)$	local density of states / single-particle spectral density at \mathbf{x}
$\varrho_0(\epsilon)$	(local) density of states of the unperturbed system
$\varrho_d(\epsilon)$	d-orbitals single-particle spectral density
$\varrho_t(\epsilon)$	tip density of states
STM	Scanning Tunnelling Microscope
STS	Scanning Tunnelling Spectroscopy
t_{imp}	t-Matrix of the impurity
\mathcal{T}	time ordering operator
T	temperature
T_K	Kondo Temperature
θ	zenith angle
$u_{\mathbf{k}}(\mathbf{x})$	lattice periodic part of the Bloch functions
U	Coulomb repulsion
UHV	ultra high vacuum $p < 10^{-9} \text{mbar}$
V	(bias) voltage
V_{kd}	hybridization between localized orbital $ d\rangle$ and band state $ k\rangle$
V_T	bias voltage used for the <i>constant current topography</i>
\mathbf{v}_{Gr}	group velocity
W	bandwidth
\mathbf{x}	position
\mathbf{x}_i	position of the impurity
\mathbf{x}_{\parallel}	vector parallel to the surface $\mathbf{x}_{\parallel} = (x, y)$

Bibliography

- [1] J. Heil, M. Primke, K. U. Würz, and P. Wyder, ‘Real Space Imaging of Ballistic Carrier Propagation in Bi Single Crystals’, *Phys. Rev. Lett.* **74**, 146 (1995).
- [2] J. M. Capinelli, H. H. Weitering, E. W. Plummer, and R. Stumpf, *Nature* **381**, 398 (1996).
- [3] C. Chappert P. Bruno, *Phys. Rev. Lett.* **67**, 2592 (1991).
- [4] J Friedel, *Nuovo Cimento Suppl.* **7**, 287 (1958).
- [5] M. F. Crommie, C. P. Lutz, and D. M. Eigler, *Nature* **363**, 524 (1993).
- [6] C. Kittel M. A. Ruderman, ‘Indirect Exchange Coupling of Nuclear Magnetic Moments by Conduction Electrons’, *Phys. Rev.* **96**, 99 (1954).
- [7] K. Yosida, ‘Ground state energy of conduction electrons interacting with a localized spin’, *Prog. Theor. Phys.* **36**, 875 (1966).
- [8] R. P. Feynman and A. R. Hibbs, *Quantum Mechanics and Path Integrals* (McGraw-Hill Companies, 1965).
- [9] S.G. Davison and M. Steslicka, *Basic theory of surface states* (Oxford University Press, 1992).
- [10] G. F. Koster, ‘Theory of Scattering in Solids’, *Phys. Rev.* **95**, 1436 (1954).
- [11] Laura M. Roth, H. J. Zeiger, and T. A. Kaplan, ‘Generalization of the Ruderman-Kittel-Kasuya-Yosida Interaction for Nonspherical Fermi Surfaces’, *Phys. Rev.* **149**, 519 (1966).
- [12] R. M. Thaler L. S. Rodberg, *Introduction to the quantum theory of scattering* (Academic press, 1967).

- [13] J. Kondo, 'Resistance Minimum in Dilute Magnetic Alloys', *Prog. Theor. Phys.* **32**, 37 (1964).
- [14] E. Hildebrand, 'Zum Dia- und Paramagnetismus in metallischen Mischkristallreihen. Das Verhalten von gelöstem Kobalt und Rhodium', *Ann. d. Physik* **30**, 593 (1937).
- [15] A.C. Hewson, *The Kondo Problem to Heavy Fermions* (Cambridge University Press, 1993).
- [16] H. Suhl, 'Dispersion theory of the Kondo effect', *Phys. Rev.* **138**, A515 (1965).
- [17] Gerald D. Mahan, *Many-Particle Physics* (Kluwer Academics/Plenum Publishers, 2000), third edn.
- [18] G. Binnig and H. Rohrer, 'Scanning tunneling microscopy', *Helv. Phys. Acta* **55**, 726 (1982).
- [19] J.T. Li, W.D. Schneider, R. Berndt, and B. Delley, 'Kondo scattering observed at a single magnetic impurity', *Phys. Rev. Lett.* **80**, 2893 (1998).
- [20] V. Madhavan, W. Chen, T. Jamneala, M.F. Crommie, and N.S. Wingreen, 'Tunneling into a single magnetic atom: Spectroscopic evidence of the Kondo resonance', *Science* **280**, 567 (1998).
- [21] N. Knorr, M.A. Schneider, L. Diekhöner, P. Wahl, and K. Kern, 'Kondo effect of single Co adatoms on Cu surfaces', *Phys. Rev. Lett.* **88**, 096804 (2002).
- [22] V. Madhavan, W. Chen, T. Jamneala, M.F. Crommie, and N.S. Wingreen, 'Local Spectroscopy of a Kondo impurity: Co on Au(111)', *Phys. Rev. B* **64**, 165412 (2001).
- [23] P. Wahl, L. Diekhöner, M. A. Schneider, L. Vitali, G. Wittich, and K. Kern, 'Kondo Temperature of Magnetic Impurities at Surfaces', *Phys. Rev. Lett.* **93**, 176603 (2004).
- [24] P. Wahl, L. Diekhöner, G. Wittich, L. Vitali, M. A. Schneider, and K. Kern, 'Kondo Effect of Molecular Complexes at Surfaces: Ligand Control of the Local Spin Coupling', *Physical Review Letters* **95**, 166601 (2005).
- [25] H.C. Manoharan, C.P. Lutz, and D.M. Eigler, 'Quantum mirages formed by coherent projection of electronic structure', *Nature* **403**, 512 (2000).
- [26] M. Plihal and J.W. Gadzuk, 'Nonequilibrium theory of scanning tunneling spectroscopy via adsorbate resonances: Nonmagnetic and Kondo impurities', *Phys. Rev. B* **63**, 085404 (2001).

- [27] O. Ujsaghy, J. Kroha, L. Szunyogh, and A. Zawadowski, ‘Theory of the Fano resonance in the STM tunneling density-of-states due to a single Kondo impurity’, *Phys. Rev. Lett.* **85**, 2557 (2000).
- [28] N. Quaas, *Scanning Tunnelling Microscopy on Co-impurified Noble Metal Surfaces: Kondo-Effect, Electronic Surface States and Diffusive Atom Transport*, Ph.D. thesis, Georg-August Universitt Göttingen (2004).
- [29] A. Weismann, *Rastertunnelspektroskopie auf magnetisch verunreinigten Cu- und Ag- Einkristalloberflächen*, Diplom thesis, unpublished, Georg-August-Universität Göttingen, IV. Physikalisches Institut (2003).
- [30] R.G. Musket, W. McLean, C.A.Colmenares, D.M. Makowiecki, and W.J. Siekhaus, ‘Preparation of atomically clean surfaces of selected elements: A review’, *Applications of Surface Science* **10** (1982).
- [31] H. Prüser, *Titel*, Diplom thesis, unpublished, Georg-August-Universität Göttingen, IV. Physikalisches Institut (2008).
- [32] David D. Chambliss and Kevin E. Johnson, ‘Nucleation with a critical cluster size of zero: Submonolayer Fe inclusions in Cu(100)’, *Phys. Rev. B* **50**, 5012 (1994).
- [33] C. J. Chen, ‘Theory of scanning tunneling spectroscopy’, *J. Vac. Sci. Technol. A* **6**, 319 (1988).
- [34] R. Wiesendanger, *Scanning Tunnelling Microscopy and Spectroscopy* (Cambridge University Press, 1994).
- [35] J. Tersoff and D. Hamann, ‘Theory and application for the Scanning Tunnelling Microscope’, *Phys. Rev. Lett.* **50**, 1998 (1983).
- [36] J. Bardeen, ‘Tunnelling from a many-particle point of view’, *Phys. Rev. Lett.* **6**, 57 (1961).
- [37] J. Tersoff and D.R. Hamann, ‘Theory of the scanning tunneling microscope’, *Phys. Rev. B* **31**, 805 (1985).
- [38] K. Besocke, ‘An easily operable scanning tunneling microscope’, *Surf. Sci.* **181**, 145 (1987).
- [39] M. A. Rosentreter, *Rastertunnelmikroskopie auf der GaAs(110)-Oberfläche bei Temperaturen von 8 K bis 300 K*, Doktor thesis, cuvillier verlag göttingen, Georg-August-Universität Göttingen, IV. Physikalisches Institut (1997).

- [40] K. Sauthoff, *Rastertunnelspektroskopie an einzelnen Donatoren und Donatorkomplexen nahe der GaAs(110)-Oberfläche*, Doktor thesis, cuvillier verlag göttingen, Georg-August-Universität Göttingen, IV. Physikalisches Institut (2003).
- [41] H. F. Schleiermacher, *Characterization of tips for scanning tunnelling microscopy*, Master's thesis, Georg-August-Universität Göttingen, IV. Physikalisches Institut (2006).
- [42] N.W. Ashcroft and N.D. Mermin, *Solid State Physics* (Harcourt college publishers, 1976).
- [43] J.A. Verges and E. Louis, 'Electron states on the (111) surface of copper', *Sol. State Comm.* **22**, 663 (1977).
- [44] W. Kohn and N. Rostoker, 'Solution of the Schrödinger Equation in Periodic Lattices with an Application to Metallic Lithium', *Phys. Rev.* **94**, 1111 (1954).
- [45] University of Florida Departement of Physics, '3D (VRML) Fermi Surface Database', <http://www.phys.ufl.edu/fermisurface/>.
- [46] D. A. Papaconstantopoulos, *Handbook of the band structure of elemental solids* (Plenum Press, 1986).
- [47] H.A. Kramers, 'La diffusion de la lumiere par les atomes', *Atti Cong. Intern. Fisica* **2**, 545 (1927).
- [48] R. de L. Kronig, 'On the theory of the dispersion of X-rays', *J. Opt. Soc. Am* **12**, 547 (1926).
- [49] W. H. Butler A. Gonis, *Multiple scattering in solids* (Springer, 2000).
- [50] E. Schrödinger, 'An Undulatory Theory of the Mechanics of Atoms and Molecules', *Phys. Rev.* **28**, 1049 (1926).
- [51] G. Binnig, N. Garcia, H. Rohrer, J. M. Soler, and F. Flores, 'Electron-metal-surface interaction potential with vacuum tunneling: Observation of the image force', *Phys. Rev. B* **30**, 4816 (1984).
- [52] N. Quaas, M. Wenderoth, A. Weismann, R.G. Ulbrich, and K. Schönhammer, 'Kondo resonance of single Co atoms embedded in Cu(111)', *Phys. Rev. B* **69**, 201103 (2004).
- [53] Samir Lounis, *Physics of magnetic clusters on surfaces*, Ph.D. thesis, Forschungszentrum Jülich (2007).

- [54] P.W. Anderson, ‘Localized Magnetic States in Metals’, *Phys. Rev.* **124**, 41 (1961).
- [55] H. K. Onnes, ‘The disappearance of the resistivity of mercury’, *Comm. Leiden* **122(b)** (1911).
- [56] W. Felsch and K. Winzer, ‘Magnetoresistivity of (La, Ce)Al₂ alloys’, *Sol. Stat. Comm.* **13**, 569 (1973).
- [57] K. Samwer and K. Winzer, ‘Magnetoresistivity of the Kondo-system (La, Ce)B₆’, *Z. Phys. B* **25**, 269 (1976).
- [58] Kenneth G. Wilson, ‘The renormalization group: Critical phenomena and the Kondo problem’, *Rev. Mod. Phys.* **47**, 773 (1975).
- [59] O. Gunnarsson and K. Schönhammer, ‘Electron Spectroscopies for Ce Compounds in the Impurity Model’, *Phys. Rev. B* **28**, 4315 (1983).
- [60] C. Zener, ‘Interaction between the *d*-shells in the Transition Metals’, *Phys. Rev.* **81**, 440 (1951).
- [61] U. Fano, ‘Effects of configuration interaction on intensities and phase shifts’, *Phys. Rev.* **124**, 1866 (1961).
- [62] B. Horvatić, D. Sokcević, and V. Zlatić, ‘Finite-temperature spectral density for the Anderson model’, *Phys. Rev. B* **36**, 675 (1987).
- [63] P. Nozieres, ‘A fermi-liquid description of the Kondoproblem at low temperatures’, *J. Low Temp. Phys.* **17**, 31 (1974).
- [64] A.C. Hewson, ‘Theory of Localized Magnetic Moments in Metals’, *Phys. Rev.* **144**, 420 (1966).
- [65] Ch. Kolf, J. Kroha, M. Ternes, and W.-D. Schneider, ‘Comment on “Fano Resonance for Anderson Impurity Systems”’, *Physical Review Letters* **96**, 019701 (2006).
- [66] S. Biermann, F. Aryasetiawan, and A. Georges, ‘First-Principles Approach to the Electronic Structure of Strongly Correlated Systems: Combining the *GW* Approximation and Dynamical Mean-Field Theory’, *Phys. Rev. Lett.* **90**, 086402 (2003).
- [67] Gregory A. Fiete and Eric J. Heller, ‘Colloquium: Theory of quantum corrals and quantum mirages’, *Rev. Mod. Phys.* **75**, 933 (2003).

- [68] László Borda, ‘Kondo screening cloud in a one-dimensional wire: Numerical renormalization group study’, *Physical Review B (Condensed Matter and Materials Physics)* **75**, 041307 (2007).
- [69] Ian Affleck, László Borda, and Hubert Saleur, ‘Friedel oscillations and the Kondo screening cloud’, *Physical Review B (Condensed Matter and Materials Physics)* **77**, 180404 (2008).
- [70] Gerd Bergmann, ‘Quantitative calculation of the spatial extension of the Kondo cloud’, *Physical Review B (Condensed Matter and Materials Physics)* **77**, 104401 (2008).
- [71] J. Homoth, M. Wenderoth, K. J. Engel, T. Druga, S. Loth, and R. G. Ulbrich, ‘Reconstruction of the local density of states in Ag(111) surfaces using scanning tunneling potentiometry’, *Physical Review B (Condensed Matter and Materials Physics)* **76**, 193407 (2007).
- [72] M.D. Daybell and W.A. Steyert, ‘Localized magnetic impurity states in metals: Some experimental relationships’, *Rev. of Mod. Phys.* **40**, 380 (1968).
- [73] S. Lounis, ‘DFT calculation of the d-orbital DOS of Fe and Co impurities in Copper’, (2008). Private communications.
- [74] Wikipedia, ‘Nyquist plot’, ‘http://en.wikipedia.org/wiki/Nyquist_plot’ (2008).
- [75] Wikipedia, ‘Bode-plot’, ‘http://en.wikipedia.org/wiki/Bode_plot’ (2008).
- [76] M. Schmid, W. Hebenstreit, P. Varga, and S. Crampin, ‘Quantum Wells and Electron Interference Phenomena in Al due to Subsurface Noble Gas Bubbles’, *Phys. Rev. Lett.* **76**, 2298 (1996).
- [77] O. Kurnosikov, O. A. O. Adam, H. J. M. Swagten, W. J. M. de Jonge, and B. Koopmans, ‘Probing quantum wells induced above a subsurface nanocavity in copper’, *Physical Review B (Condensed Matter and Materials Physics)* **77**, 125429 (2008).
- [78] R. Laskowski J. Kunes, ‘Magnetic ground state and Fermi surface of bcc Eu’, *Phys. Rev. B* **70**, 174415 (2004).
- [79] J. Slater, ‘Interaction of Waves in Crystals’, *Rev. Mod. Phys.* **30**, 197 (1958).
- [80] J. C. Slater and G. F. Koster, ‘Simplified LCAO Method for the Periodic Potential Problem’, *Phys. Rev.* **94**, 1498 (1954).
- [81] Per-Olov Löwdin, ‘A Note on the Quantum-Mechanical Perturbation Theory’, *The Journal of Chemical Physics* **19**, 1396 (1951).

Danksagung

An dieser Stelle möchte ich mich bei allen bedanken, die zum Gelingen dieser Arbeit beigetragen haben:

Herrn Prof. Dr. Rainer G. Ulbrich danke ich für die Möglichkeit, dieses spannende Thema an seinem Institut bearbeiten zu dürfen, für die zahlreichen und fruchtbaren Gespräche sowie für das große Interesse an dieser Arbeit.

Herrn Prof. Dr. Schönhammer danke ich für die Übernahme des Zweitgutachtens.

Dr. Martin Wenderoth danke ich für die einzigartig gute Betreuung der Doktorarbeit und die zahlreichen, aufschlussreichen Diskussionen.

Bernhard Spicher gilt mein Dank für die entgegenbrachte Unterstützung in allen UHV-Angelegenheiten.

Besonderer Dank geht auch an Henning Prüser, der zum Gelingen eines wesentlichen Teils der präsentierten Messungen beigetragen hat.

Dr. Samir Lounis, Prof. Peter H. Dederichs und Prof. Stefan Blügel danke ich für die gute Zusammenarbeit.

Peter Löptien und Swante Siewers danke ich für viel Spaß im Büro. Der restlichen Arbeitsgruppe, namentlich Thomas Druga, Jan Homoth, Karolin Löser, Sebastian Loth, Karen Teichmann und Lars Winking danke ich für eine schöne Zeit.

Vor allem danke ich aber Anna für das entgegengebrachte Verständnis während der letzten Monate.

Lebenslauf

Name: Alexander Weismann
Nationalität: deutsch
Geboren am: 30. Dezember 1978
Geburtsort: Gräfelfing

05-1998 : Abitur am Katharineum zu Lübeck
10-1998 : Beginn des Physikstudiums, Universität Göttingen.
04-1999 : Beginn des Medizinstudiums, Universität Göttingen.
07-2000 : Vordiplom Physik
09-2001 : Ärztliche Vorprüfung
01-2002 : Beginn der Diplomarbeit am IV. Physikalischen Institut der
Universität Göttingen.
07-2003 : Diplom in Physik
10-2003 : Beginn der Promotion am IV. Physikalischen Institut der Uni-
versität Göttingen im Rahmen des SFB 602.